Electronic Properties and Raman Spectra of High-T_c Materials

A Theoretical Study within Density Functional Theory

Dissertation

Submitted to the faculty of natural sciences by

Heinrich Auer

under supervision of

Ao. Univ.-Prof. Dr. Dr. h.c. C. Ambrosch-Draxl

at

THE INSTITUTE OF THEORETICAL PHYSICS

Karl-Franzens-University of Graz

Graz, November 2001

Acknowledgments

I am most grateful to my supervisor Claudia Ambrosch-Draxl who has encouraged my Ph.D. studies all these years. She has always been an fruitful source of enthusiasm which, of course, has led me to work even harder on our projects. Moreover I want to thank her for many useful hints concerning calculations with the WIEN97 code and also in the interpretation and presentation of the results, not forgetting her great support by formulating this work in English.

Eugene Sherman is acknowledged for encouraging discussions on site- selective isotope substitutions and Y-point phonons and for proof reading and correcting this thesis.

I would like to thank Peter Puschnig for providing me his Mathematica programs accompanied by very detailed illustrations, which have been very useful in the analysis of my first-principle results.

This work would have been much harder without Timo Thonhauser who has helped me a lot with my computer problems, especially I want to thank him for many useful advises in LaTeX.

I want to thank Robert Kouba, who gave me very important advises at the beginning of my work, which allowed me to start very quickly with first calculations.

I also like to thank the other members of our group Florian Ladstädter, Jürgen Spitaler, Kerstin Weinmeier and Pavol Dudešek for providing a good and fine working atmosphere.

I also would like to say thank you to Jutta Telsnig for her encouragement, help, support and for taking care of our son Erik, in order to provide me with enough time to finish my thesis.

Last, but not least, I also want to thank my mother for supporting us (me) in many different ways.

Summary

After the discovery of high temperature superconductivity in the La-(Ba,Sr)-Cu-O compound by Bednorz and Müller in 1986 a variety of other superconducting materials have been found with even higher T_c' s. Most of them contain copper-oxygen planes which are responsible for the superconducting properties. During the years the critical temperature steadily climbed up, where the highest T_c reached so far is more than $160K$. It scales with the number of CuO_2 planes n with its maximum for n=3 and can be tuned by doping and applying pressure.

Despite the fact that the critical temperature could be tremendously increased since the beginning of the high T_c research, the pairing mechanism is still not understood. The puzzling physical problems in these kind of materials are not fully solved, a fact also hindering industrial applications, which are still far away from the expectations of the late eighties.

In conventional superconductors, the pairing of electrons to Cooper pairs is mediated by the exchange of phonons, which can be quantitatively described within the BCS theory introduced by Bardeen, Cooper, and Schrieffer. In high T_c materials, however, superconductivity cannot be traced back to electron-phonon coupling, even when the BCS theory is extended to anisotropic systems. Nevertheless, the role of the phonons turned out to be important, therefore lattice effects have to be investigated in detail in order to get more insight into the nature of superconductivity.

This work focuses on the investigation of the interplay between the electronic properties and lattice effects in high T_c compounds. A major part of the thesis is dedicated to Raman scattering which contains important information, about the electronic subsystems, the lattice properties, and their interplay. In terms of materials, $YBa_2Cu_3O_7$ and the Hg-based superconductors (termed the *Hg-family*) are studied. The former one has been the first superconductor which could be cooled by liquid nitrogen (T_c =$93K$) and is one of the most investigated materials. For this compound the effect of site-selective isotope substitution is investigated in detail. It turned out that not only the phonon frequencies are modulated by the replacement of an atom with its isotope, but also the Raman intensities are strongly influenced. Moreover, phonon frequencies and eigenvectors of zone-boundary phonons have been determined providing a basis for the assignment of experimental data and a starting point for the calculation of electron-phonon

coupling.

The Hg-family is one of the most fascinating systems, one reason being the fact that the three-layer representative holds the *world record* in T_c. At the same time $HgBaCuO_4$ exhibits the highest critical temperature among the single-layer cuprates. But maybe most important, all three different effects influencing the superconducting properties, namely doping, pressure, and the number of copper-oxygen layers can be studies within one family of compounds. For these reasons a systematic study of the electronic properties and Raman spectra has been performed for four members of $HgBa_2Ca_{n-1}Cu_nO_{2n+2}$, namely Hg-1201, Hg-1212, Hg-1223, and Hg-1234, which stand for the one- two, three, and four-layer compounds, respectively. Hereby band structure, total and site-projected densities of states, and Raman spectra as a function of pressure are discussed and the changes in theses properties are explained when adding additional structural elements (copper-oxygen and Ca layers). For the simplest representative, Hg-1201, the role of oxygen doping has been studied in detail revealing a clear picture of how doping and the charge carriers (holes) in the CuO_2 planes are related to each others. This is an important fact since so far most of the models dealing with the superconducting mechanism take the hole concentration rather than the doping level as a starting point.

Contents

Chapter 1

Introduction

After the discovery of high temperature superconductivity by Bednorz and Müller in 1986 in the La-(Ba,Sr)-Cu-O compound a variety of other superconducting materials have been found with even higher T_c' s. Most of them contain copper-oxygen planes which are responsible for the superconducting current. During the years the critical temperature steadily climbed up, where the highest T_c reached so far is more than $160K$. It scales with the number of CuO_2 planes n with its maximum for n=3 and can be tuned by doping and applying pressure.

Despite the fact that the critical temperature could be tremendously increased since the beginning of the high T_c research, the pairing mechanism is still not understood. The puzzling physical problems in these kind of materials are not fully solved, a fact also hindering industrial applications, which are still far behind the expectations of the late eighties.

In conventional superconductors, the pairing of electrons to Cooper pairs is mediated the by exchange of phonons, which can be quantitatively described within the BCS theory introduced by Bardeen, Schriefer, and Cooper. In high T_c materials, however, superconductivity cannot be traced back to electron-phonon coupling, even if the BCS theory is extended to anisotropic systems. Nevertheless, the role of the phonons turned out to be important, therefore lattice effects have to be investigated in detail in order to get more insight into the nature of superconductivity.

For more than a decade after the discovery of high-temperature superconductivity by Bednorz and Müller [1], its mechanism is still not understood despite of the success in finding materials with very high transition temperatures up to 160 K. The first high-T_c compound La-(Ba,Sr)-Cu-O contained CuO_2-layers, which should remain a characteristic for most high-T_c' s. It was also found out that the transition temperature can be varied via doping and applying pressure. Over the years many theories have been developed. Some theories favor spin fluctuations for the pairing mechanism. Another approach, as already mentioned, is that the theory of conventional superconductivity could be extended in order to explain the high-temperature superconductivity. In the following a short history

of supercondivity is given, followed by the motivation for this work.

1.1 The History of Superconductivity

The year of birth of superconductivity was in 1911, when H.K. Onnes [2] investigated the temperature dependence of the electrical resistivity (R) of mercury. Despite his expectation of a continuous decrease of R he found that at a certain so called critical temperature ($T_c^{Hg} = 4.2K$) the electrical resistivity of mercury vanished completely. He concluded that he had found a new state, which he called *superconducting state* [3]. The disappearance of the electrical resistivity should not be the only characteristic of this new state.

In 1933 Meissner and Ochsenfeld [4] showed, that up to a critical external magnetic field H_c a superconductor behaves like a perfect diamagnetic material, which means that it repels a magnetic field from its interior. This discovery also served as a starting point for a thermodynamical macroscopic description of the superconducting state.

After this it took nearly twenty years until a commonly accepted microscopic theory for the superconducting phenomenon was established. In 1957, **B**ardeen, **C**ooper and **S**chrieffer (BCS) were able to describe all experimental facts by introducing an interaction between metal electrons via the exchange of virtual particles (phonons). This attractive interaction makes two electrons with opposite momenta and spins form a new bosonic particle named a Cooper pair, and this change in the particle's character is the explanation for superconductivity. Within this approach it was now possible to explain the superconducting state as a macroscopic quantum phenomenon, where the Cooper pairs are the charge carriers, all in the same coherent state. Furthermore it is presumed that the electrons can only interact with the crystal lattice if the Cooper pair is broken, and that is what happens at or above T_c.

A fundamental experiment which directly shows that the interaction leading to superconductivity has its origin in lattice vibrations, as claimed in the BCS theory, is the very well known isotope effect. With this experiment it was shown, that the superconducting effect not only depends on the electronic properties but also on the nuclear masses of the atoms building up the crystal. According to the BCS theory T_c should be proportional to $M^{-1/2}$ (M being the atomic mass), an expectation which was proven very impressively by Maxwell [5] and Lock, Pippard and Shoenberg [6] for tin.

Although superconductivity was then understood in principle, it stayed a low temperature phenomenon until 1986 [1]. Before that time only materials with T_c up to 30 K had been known. Shortly after, however, several complex compounds, most of them containing CuO_2 planes (cuprates), have been found with transition temperatures ranging from 30 K ($La_{1.85}Ba_{0.15}CuO_4$) [1] up to 160 K ($HgBa_2Ca_2Cu_3O_{8+\delta}$) [7, 8]. By entering the temperature region of liquid nitrogen

($T_S = 77\ K$), first realized by $YBa_2Cu_3O_7$, the cooling was much cheaper and easier to handle compared to liquid helium. All the cuprates are pronounced type II superconductors, what means that in contrast to superconductors of type I, the upper critical magnetic field, which completely destroyes the superconductivity is very high. This is a feature which makes them qualified to serve as materials for generating high magnetic fields. Thus the door for new technical applications of the superconducting phenomenon was opened. Now we can e.g. look at superconducting magnetic coils producing very strong magnetic fields or SQUIDS based on the new type of superconductors.

But everything in life has its prize: Within the BCS-theory such high transition temperatures cannot be explained with a phononic interaction as the pairing mechanism for the Cooper pairs. So in the case of these so called high-temperature superconductors the microscopic theory has to be extended, modified or changed for gaining insight into the superconducting mechanism in these materials. Only a deep understanding will help to design new materials with even higher T_c's.

1.2 Motivation and Purpose of this Work

The principle problem someone faces when starting to investigate the physical properties of high-temperature superconductors is that most of them have a very complicated crystal structure with many (up to 20) crystallographically different atoms in their unit cells. As a consequence, the theories, which have excellently worked in the description of the physical and superconducting properties of simple metals and compounds seem not to record sufficiently what is going on in high-T_c materials. Nevertheless, the existence of Cooper pairs as the carriers of the supercurrent in high-T_c materials like in $YBa_2Cu_3O_7$ [9] is well established. The first attempts in explaining the high-temperature superconducting phenomena was to modify the pictures which have been applied to describe the superconducting effect in low-temperature superconductors by taking into account the anisotropy and the complex crystal structure of those materials. It has been a challenge to clarify, whether extensions of the BCS-theory, which take into account the complicated band structures and the great anisotropy of those materials, were able to lead back the effective electron-electron interaction to an interaction via phonons. This is, however, a complicated task since analytic expressions for the superconducting critical temperature, the superconducting gap, etc. can only be derived in case of a simple Fermi surface with nearly constant density of states around the Fermi level. These are requirements which are by far not fulfilled in high-T_c compounds. Such theoretical studies have shown that in case of complicated band structures also high transition temperatures ($T_c \approx 100$ K) mediated by electron-phonon interaction could be expected [10–12].

Nevertheless the major part of the scientific community favors a different pairing mechanism, where magnetic fluctuations seem to be the most likely scenario, but the phonons still could play an important role. Recent publications propose a model where the interplay between electron-electron interaction and lattice effects plays a leading role in the explanation of high-temperature superconductivity [13], and it is claimed that the part of the phonons is even undeniable [14]. Thus electron-phonon coupling and the role of the lattice have been always subject of investigations since the discovery of high-T_c superconductivity. Results of these studies indicated the importance of the coupling of electrons to the lattice in the normal state as well as a significant relation between phonons and the superconducting transition.

In the following some experiments (see Reference [15]), which emphasize the existence of strong electron-phonon coupling in high-T_c materials are given. However, it should be noticed here again that these experiments are not a proof for electron-phonon interaction being the pairing mechanism.

1. Inelastic neutron scattering experiments have shown a great change in the phonon density of states between the insulating $YBa_2Cu_3O_6$ and the superconducting $YBa_2Cu_3O_7$ [16].

2. Investigations of the Raman effect in $YBa_2Cu_3O_7$ have revealed, that strong electron-phonon interaction leads to changes in the phonon frequencies at the transition to the superconducting phase [17, 18].

3. The measurement of the thermal conductivity of $YBa_2Cu_3O_7$ has yield a remarkable electron-phonon interaction [19].

A deep understanding of physical phenomena always requires an interplay between theory and experiments. For this reason detailed theoretical studies have to be carried out in order to analyze existing experimental data and to gain information to guide further measurements. It turned out that first-principle calculations describe the properties of high-T_c cuprates very accurately close to optimal doping, were those materials demonstrate good metallic behavior. Further experience showed that the best agreement with experimental data is achieved when the crystal structure is optimized theoretically, i.e. when unit cell volume, axes ratios and atomic positions are obtained by searching for the lowest total energy [20]. Thus most of the calculations in this work were performed within the optimized crystal structures (see Chapter 8).

1.3 $YBa_2Cu_3O_7$ and the Mercury Family

This work focuses on the investigation of phonons and lattice effects in high-temperature superconductors, in particular $YBa_2Cu_3O_7$ (YBCO7) and the $HgBa_2Ca_{n-1}Cu_nO_{2n+2+\delta}$ compounds, which in the following will be called the *Hg-family*. The first part will deal with phonons and Raman spectra in $YBa_2Cu_3O_7$. Special attention will be paid to the effects of site-selective isotope substitution on the vibrational frequencies and Raman intensities. In the second part the electronic structure and lattice vibrations of the Hg-family will be discussed in detail. These properties are investigated as a function of composition (number of CuO_2-layers), pressure, and oxygen doping.

All the high-T_c materials have a close relationship with the Perovskite structure. The most important structural elements of the cuprate superconductors are CuO_2 layers, the number of which varies between one and five in different unit cells and governs the critical temperature. In $YBa_2Cu_3O_7$ there are two CuO_2 layers in the unit cell with a T_c of 93 K. In the mercury family, crystals up to five CuO_2 layers can be synthesized [21] where the maximum T_c of 136 K is reached for $n = 3$. The heavy elements, like Ba, La, Y, Hg, etc., which are present in all these materials are assumed to serve as charge reservoirs and to stabilize the crystal.

A further characteristic of high-temperature superconductors is the fact, that in most of these materials the normal-state carriers are holes. The holes are mainly located at the CuO_2 layers, which are made responsible for the superconducting state. In the normal state the conductivity parallel to the CuO_2-planes

is substantially greater than the conductivity normal to the planes [22], what is also a sign of the already mentioned anisotropy of these materials. In both compounds under investigation, the concentration of holes in the CuO_2 planes can be enhanced via oxygen doping and in this way T_c can be controlled.

1.4 Phonons and the Raman Scattering Process

As already indicated, the electronic and the superconducting properties of YBCO and other high-T_c materials are governed in principle by their crystal structure, which implies the lattice constants as well as the particular atomic positions in the unit cell. If the ions are displaced from their equilibrium positions the increase of the total energy is associated to lattice forces acting on the nuclei and forcing them to move back. The displacements result then in lattice vibrations, which lead to changes in the electronic structure due to the strong electron-phonon coupling in these compounds. When an electromagnetic wave propagates through the crystal, its frequency is changed due to the modulation of the dielectric tensor caused by the time-dependent ionic displacements. This frequency modulation by lattice vibrations results then in inelastic light scattering, usually called Raman scattering.

Since Raman scattering is determined by the influence of the ionic motions on the electronic states in a wide energy range, Raman spectroscopy provides valuable informations on both, the lattice properties as well as the electronic subsystem. The total energy and the dielectric tensor as a function of the atomic coordinates required for the theoretical description of the Raman spectra can be obtained by first-principle band structure methods within the frozen-phonon approach based on the Born-Oppenheimer approximation.

Chapter 2

The Dynamics of the Crystal Lattice

The present chapter is dedicated to quantized lattice vibrations, which are important in describing the Raman scattering process. After a short discussion of the Born-Oppenheimer approximation, an introduction to phonons, symmetry considerations and normal modes will be given. At the end of this chapter some fundamental group theoretical formulas are presented in order to provide a tool for carrying out a factor group analysis.

2.1 The Born-Oppenheimer Approximation

The exact Hamilton operator of a crystal can be written in the form

$$\hat{H} = \hat{H}_{el}(\vec{r}) + \hat{H}_{lat}(\vec{R}) + \hat{H}_{el,lat}(\vec{r}, \vec{R}), \tag{2.1}$$

where $\vec{r}$ and $\vec{R}$ denote all the coordinates of the electrons and nuclei, respectively. The operators $\hat{H}_{el}$ and $\hat{H}_{lat}$ contain the corresponding kinetic and potential energies, whereas $\hat{H}_{el,lat}$ describes the interaction between the electrons and the nuclei. The solution of this many-body problem is only possible with the help of some approximations. As a first step one may consider the different masses of electrons and nuclei. Since electrons have a much higher velocity than the heavy nuclei they are able to follow adiabatically the changes in the atoms positions. As a consequence, it is possible to calculate the electron distribution and the total energy of the crystal, for a fixed configuration of the atomic coordinates $\vec{R}$

$$\left[\hat{H}_{el}(\vec{r}) + \hat{H}_{el,lat}(\vec{r}, \vec{R})\right]\psi_{el}(\vec{r}, \vec{R}) = E_{el}(\vec{R})\psi_{el}(\vec{r}, \vec{R}). \tag{2.2}$$

This so-called adiabatic approximation was first suggested by Born and Oppenheimer [23, 24]. Equation (2.2) can be solved for different sets of atomic coordinates and thus the total energy as a function of the atomic positions is

known. This energy surface $E_{el}(\vec{R})$ serves as a contribution to the potential for the Schrödinger equation of the lattice vibrations

$$[\widehat{H}_{lat}(\vec{R}) + E_{el}(\vec{R})]\psi_{lat}(\vec{R}) = E_{lat}\psi_{lat}(\vec{R}). \tag{2.3}$$

The advantage of this approach for the investigation of lattice dynamics lies in the fact, that the movement of the electrons can be ignored and only the motions of the ions have to be taken into account. In the following we assume that the requirements of the Born-Oppenheimer approximation are fulfilled.

2.2 The Harmonic Approximation

In a part of a crystal consisting of N elementary cells, each containing r atoms, the nuclei in their equilibrium positions are specified by vectors written as

$$\begin{aligned} \vec{R}_{nm} &= \vec{R}_n + \vec{R}_m \quad m = 1, \ldots, r \\ \vec{R}_n &= n_1\vec{a}_1 + n_2\vec{a}_2 + n_3\vec{a}_3, \quad n, n_i = 1, \ldots, N \\ \vec{R}_m &= m_1\vec{a}_1 + m_2\vec{a}_2 + m_3\vec{a}_3, \quad 0 < m_i \leq 1. \end{aligned} \tag{2.4}$$

Here $\vec{R}_n$ points from an arbitrary origin to the center of the n-th elementary cell and $\vec{R}_m$ points from that center to the m-th ion within this cell. The kinetic energy of this system is given by

$$T = \sum_{nmi} \frac{M_m}{2}\left(\frac{\partial s_{nmi}}{\partial t}\right)^2, \tag{2.5}$$

where s_{nmi} describes the displacement of the m-th ion in the n-th unit cell along the component i, and M_m specifies the mass of the m-th ion. If the potential energy of this system is now expanded with respect to powers of s_{nmi} one obtains the expression

$$\begin{aligned} W(t) &= W(\vec{R}_{nm}) + \sum_{nmi}\left(\frac{\partial W(\vec{x})}{\partial s_{nmi}}\right)_{\vec{x}=\{\vec{R}_{nm}\}} s_{nmi} + \\ &\quad \frac{1}{2}\sum_{\substack{nmi \\ n'm'i'}}\left(\frac{\partial^2 W(\vec{x})}{\partial s_{nmi}\partial s_{n'm'i'}}\right)_{\vec{x}=\{\vec{R}_{nm}\}} s_{nmi}s_{n'm'i'} + \cdots \end{aligned} \tag{2.6}$$

In this expression $\vec{x}$ describes the actual positions of all the ions at time t. The first part of equation (2.6) is the potential energy of the crystal in its equilibrium (with respect to the displacements of the ions). The expansion coefficients appearing in the second term describe the force in direction i acting on atom m. For the equilibrium position it follows that

$$\left(\frac{\partial W(\vec{x})}{\partial s_{nmi}}\right)_{\vec{x}=\{\vec{R}_{nm}\}} = 0.$$

The third term may be written in the form

$$\frac{1}{2}\sum_{\substack{nmi\\ n'm'i'}}\left(\frac{\partial^2 W(\vec{x})}{\partial s_{nmi}\partial s_{n'm'i'}}\right)_{\vec{x}=\{\vec{R}_{nm}\}} s_{nmi}s_{n'm'i'} = \frac{1}{2}\sum_{\substack{nmi\\ n'm'i'}}\Phi_{nmi}^{n'm'i'}s_{nmi}s_{n'm'i'}. \quad (2.7)$$

(2.8)

Since the *harmonic approximation* is used in the further considerations terms of higher orders are neglected. If it is assumed now that a crystal is a conservative system the symmetry relation [25]

$$\Phi_{nmi}^{n'm'i'} = \Phi_{n'm'i'}^{nmi} \quad (2.9)$$

can be derived and Newton's equation of motion for the nm-th ion in direction i can be obtained

$$M_m\ddot{s}_{nmi} = -\sum_{n'm'i'}\Phi_{nmi}^{n'm'i'}s_{n'm'i'}. \quad (2.10)$$

The matrix element $\Phi_{nmi}^{n'm'i'}$ (force constant) describes the fact that a force in direction i on the ion (nm) is caused by the ion $(n'm')$ displaced along the i' axis.

Taking into account the effect of an infinitesimal translation and rotation of the crystal, more symmetry relations of $\Phi_{nmi}^{n'm'i'}$ can be derived. Regarding, additionally, the symmetry of a special lattice the differential equations (2.10) may partly decouple.

A time periodic solution of equation (2.10) can be found via the ansatz

$$s_{nmi}(t) = \frac{1}{\sqrt{M_m}}u_{nmi}e^{-i\omega t} \quad (2.11)$$

leading to the eigenvalue equation

$$\omega^2 u_{nmi} = \sum_{n'm'i'}D_{nmi}^{n'm'i'}u_{n'm'i'} \quad (2.12)$$

with

$$D_{nmi}^{n'm'i'} = \frac{\Phi_{nmi}^{n'm'i'}}{\sqrt{M_m M_{m'}}}. \quad (2.13)$$

The quantity ω can only be purely imaginary (what can be excluded for physical reasons) or purely real. For each eigenvalue ω_j $(j = 1, ..., 3N)$ there exists a corresponding eigenvector $\vec{u}^{(j)}$ with $3rN$ components, which describes the j-th normal vibration of the system.

Until now no thought has been given to the translational symmetry of the lattice, which can be introduced by the ansatz

$$u_{nmi} = c_{mi}e^{i\vec{q}\vec{R}_n}. \quad (2.14)$$

Inserting equation (2.14) into equation (2.12) yields

$$\omega^2 c_{mi} = \Big[\sum_{m'i'}\sum_{n'} \frac{\Phi_{min}^{m'i'n'}}{\sqrt{M_m M_{m'}}} e^{i\vec{q}(\vec{R}_{n'}-\vec{R}_n)}\Big] c_{m'i'}. \tag{2.15}$$

If it is now taken into account that the summation over n' is done at a fixed n the right hand side of equation (2.15) can be rewritten as a summation over $n'-n$ and with the help of the definition

$$D_{mi}^{m'i'}(\vec{q}) \equiv \sum_{n'} \frac{\Phi_{min}^{m'i'n'}}{\sqrt{M_m M_{m'}}} e^{i\vec{q}(\vec{R}_{n'}-\vec{R}_n)} \tag{2.16}$$

one ends up with the eigenvalue equation

$$\omega^2 c_{mi} = \sum_{m'i'} D_{mi}^{m'i'}(\vec{q}) c_{m'i'}. \tag{2.17}$$

Thereby the system of $3rN$ equations (2.12) could be reduced to a system of $3r$ equations. This system is now characterized by $3r$ eigenvalues ω_j with their corresponding eigenvectors $\vec{c}^{(j)}$, all being functions of $\vec{q}$[1]

$$\omega_j \equiv \omega_j(\vec{q}), \qquad \vec{c}^{\,(j)} \equiv \vec{c}^{\,(j)}(\vec{q}). \tag{2.18}$$

The eigenvectors form an orthonormal system.

Summarizing the previous mathematical definitions and transformations it is now possible to write the displacement of the nm-th ion in direction i within the $j\vec{q}$-th vibrational eigenstate as

$$s_{nmi}^{(j)}(\vec{q},t) = \frac{1}{\sqrt{M_m}} c_{mi}^{(j)}(\vec{q}) e^{-i\omega_j(\vec{q})t}. \tag{2.19}$$

The vector $\vec{q}$ already introduced above is a reciprocal lattice vector[2], which can be reduced to the first Brillouin zone, and $\omega_j(\vec{q})$ is a lattice periodical function of $\vec{q}$. j is limited to $3r$ branches.

2.3 The Second Quantization: Phonons

According to the previous section the Hamiltonian in equation (2.3) can be written as

$$\hat{H}_{lat} = \sum_{nmi} \frac{M_m}{2}\Big(\frac{\partial s_{nmi}}{\partial t}\Big)^2 + \frac{1}{2}\sum_{\substack{nmi\\ n'm'i'}} \Phi_{n'm'i'}^{nmi} s_{nmi} s_{n'm'i'}, \tag{2.20}$$

[1]It is common to name the function $\omega_j(\vec{q})$ the dispersion-relation of the j-th normal lattice vibration.

[2]The definition of the reciprocal lattice vectors will be introduced later on in Section 2.3.

and one can write a general displacement $s_{nmi}(t)$ of an ion as a linear combination of special solutions (see (2.19)) in the form

$$s_{nmi}(t) = \frac{1}{\sqrt{M_m}} \sum_{j,\vec{q}} \beta_{j,\vec{q}} c_{mi}^{(j)}(\vec{q}) e^{i\vec{q}\vec{R}_n} e^{-i\omega_j(\vec{q})t}. \tag{2.21}$$

Introducing time-dependent coefficients $Q_j(\vec{q},t)$ by combining the expansion coefficients $\beta_{j,\vec{q}}$ and the harmonic time-dependent exponential functions

$$e^{-i\omega_j(\vec{q})t}\beta_{j,\vec{q}} \equiv \frac{1}{\sqrt{N}} Q_j(\vec{q},t), \tag{2.22}$$

one obtains an expression for the ionic displacements

$$s_{nmi}(t) = \frac{1}{\sqrt{NM_m}} \sum_{j,\vec{q}} Q_j(\vec{q},t) c_{mi}^{(j)}(\vec{q}) e^{i\vec{q}\vec{R}_n}. \tag{2.23}$$

Inserting equation (2.23) into equation (2.20) using equations (2.11)-(2.13) then yields the Hamiltonian

$$\hat{H}_{lat} = \frac{1}{2} \sum_{j,\vec{q}} \Big[\frac{\partial Q_j^*(\vec{q},t)}{\partial t} \frac{\partial Q_j(\vec{q},t)}{\partial t} + \omega_j^2(\vec{q}) Q_j^*(\vec{q},t) Q_j(\vec{q},t) \Big]. \tag{2.24}$$

As a result of these transformations the Hamiltonian has split into $3rN$ independent terms. In other words: *The coupled single vibrations have been fragmented into uncoupled collective vibrations.*

Furthermore, if we introduce now the creation and annihilation operators given by

$$\begin{aligned} \hat{b}_{j\vec{q}}^{\dagger} &= \frac{1}{\sqrt{2\hbar\omega_{j\vec{q}}}} \Big[\omega_{j\vec{q}} \widehat{Q}_j^{\dagger}(\vec{q}) - i\widehat{\dot{Q}}_j(\vec{q}) \Big] \\ \hat{b}_{j\vec{q}} &= \frac{1}{\sqrt{2\hbar\omega_{j\vec{q}}}} \Big[\omega_{j\vec{q}} \widehat{Q}_j(\vec{q}) + i\widehat{\dot{Q}}_j^{\dagger}(\vec{q}) \Big], \end{aligned} \tag{2.25}$$

where $\widehat{\dot{Q}}_j$ is the canonically conjugate momentum to the coordinate $\widehat{Q}_j$, we can write the total energy of all lattice vibrations in form of the second quantization as[3]

$$\hat{H}_{lat} = \sum_{j,\vec{q}} \hbar\omega_{j\vec{q}} \Big(\hat{b}_{j\vec{q}}^{\dagger} \hat{b}_{j\vec{q}} + \frac{1}{2} \Big) \tag{2.26}$$

by having inserted equation (2.25) into equation (2.24). The product of the two operators $\hat{n} = \hat{b}^{\dagger}\hat{b}$ is the number operator.

[3]Mathematical details are given in [25].

Thus the Schrödinger equation of the lattice vibrations can also be written in the following form

$$\hat{H}_{lat}|\psi\rangle = \sum_{j\vec{q}} \hbar\omega_{j\vec{q}}\Big(\hat{n}_{j\vec{q}} + \frac{1}{2}\Big)|\psi\rangle = E|\psi\rangle. \tag{2.27}$$

The total energy and the wave functions are specified there by

$$E = \sum_{j}^{3r}\sum_{\vec{q}}^{N} \hbar\omega_{j\vec{q}}\Big(n_{j\vec{q}} + \frac{1}{2}\Big) \tag{2.28}$$

and

$$|\psi\rangle = |n_{j_1,\vec{q}_1}, \ldots, n_{j_{3s},\vec{q}_1}, \ldots\ldots, n_{j_1,\vec{q}_N}, \ldots, n_{j_{3s},\vec{q}_N}\rangle \tag{2.29}$$

with

$$|n_{j,\vec{q}}\rangle = \frac{1}{\sqrt{n_{j\vec{q}}!}}\Big(\hat{b}^{\dagger}_{j\vec{q}}\Big)^{n}|0\rangle, \tag{2.30}$$

where $n_{j,\vec{q}} = 0, 1, 2, \ldots$ is the number of phonons with wavevector $\vec{q}$, branch j and energy $\hbar\omega_j(\vec{q})$. The total energy is simply the sum over the energies of all eigenvibrations.

At last, the displacements of the ions can be rewritten in terms of creation and annihilation operators

$$\hat{s}_{nmi} = -\sqrt{\frac{\hbar}{2NM}}\sum_{j\vec{q}} \frac{1}{\sqrt{\omega_{j\vec{q}}}}\Big[c^{(j)}_{mi}(\vec{q})\hat{b}_{\vec{q}j}e^{i\vec{q}\vec{R}_n} + c^{*(j)}_{mi}(\vec{q})\hat{b}^{\dagger}_{-\vec{q}j}e^{-i\vec{q}\vec{R}_n}\Big]. \tag{2.31}$$

It can be seen that the displacements of the lattice ions can be described by a collective creation and annihilation of phonons. Due to (2.28) it is easy to see that the number of phonons depends on the energy of the lattice. For $T = 0\ K$ the number of phonons goes to zero and the energy of the lattice is the zero-point energy. So we see that in contrast to the number of electrons the number of phonons is not a constant and depends on the temperature. It shall be recalled here, that the temperature dependence of the phonon occupation number is given by the Bose distribution

$$\bar{n}_{j\vec{q}} = \frac{1}{\exp\left[\frac{\hbar\omega_{j\vec{q}}}{k_B T}\right] - 1}. \tag{2.32}$$

2.4 Group Theory of Lattice Dynamics

The first goal in a quantum mechanical problem is usually to diagonalize the Hamiltonian $\hat{H}$. In the presence of degeneracy, the states may be classified by means of quantum numbers in addition to the energy. These are characterized by eigenvalues of operators which commute with $\hat{H}$. The existence of such operators reflects symmetry properties of a physical system and gives rise to the observed degeneracy.

These symmetries have their origin in the symmetry properties of a given crystal lattice, which can be displayed by consecutively applied rotations and translations, which leave the crystal invariant.[4] The symmetry properties of crystalline solids and their effects on physics can be handled very effectively by group theory, what can be a great help in simplifying a given physical problem.

So as a first step, it will be shown that the symmetry properties of a crystal can be expressed by operators which commute with $\hat{H}$. As a second step, these operators will be analyzed and a recipe will be extracted, of how the problem of determining the eigenvectors of the normal vibrations of equation (2.15) can be simplified.

A symmetry operation in solid state physics may be specified by operators as $\hat{S}_{\{\tau|\vec{t}\}}$ in the Hilbertspace which are defined in the following way

$$\hat{S}_{\{\tau|\vec{t}\}} f(\vec{r}) \;=\; f(\{\tau|\vec{t}\}\vec{r}). \tag{2.33}$$

Here τ is a unitary rotation matrix, which describe the transformation $\vec{r}\,' = \tau\vec{r}$, and $\vec{t}$ is a vector which moves $\vec{r}\,'$ to a vector $\vec{r}\,'' = \vec{r}\,' + \vec{t}$. Since these operators act on an orthonormal system of functions, as follows,

$$\begin{aligned}
\hat{S}_{\{\tau|\vec{t}\}}|\vec{r}\rangle &= |\{\tau|\vec{t}\}\vec{r}\rangle, \\
\langle\vec{r}|\hat{S}^{\dagger}_{\{\tau|\vec{t}\}} &= \langle\{\tau|\vec{t}\}\vec{r}|, \\
\langle\vec{r}\,'|\hat{S}^{\dagger}_{\{\tau|\vec{t}\}}\hat{S}_{\{\tau|\vec{t}\}}|\vec{r}\rangle &= \langle\{\tau|\vec{t}\}\vec{r}\,'|\{\tau|\vec{t}\}\vec{r}\rangle = \delta(\vec{r}-\vec{r}\,'), \\
\hat{S}^{\dagger}_{\{\tau|\vec{t}\}}\hat{S}_{\{\tau|\vec{t}\}} &= \mathbb{1}
\end{aligned} \tag{2.34}$$

they are unitary. For the operator of a lattice periodical potential $\hat{V}(\vec{r})$ the following relation holds:

$$\hat{S}_{\{\tau|\vec{t}\}}\hat{V}(\vec{r})\hat{S}^{\dagger}_{\{\tau|\vec{t}\}} = \hat{V}(\vec{r}) \tag{2.35}$$

or

$$\hat{S}_{\{\tau|\vec{t}\}}\hat{V}(\vec{r}) = \hat{V}(\vec{r})\hat{S}_{\{\tau|\vec{t}\}} \quad\longrightarrow\quad \left[\hat{S}_{\{\tau|\vec{t}\}}, \hat{V}(\vec{r})\right] = 0. \tag{2.36}$$

[4] In this context, invariant means that after applying a symmetry operation to a crystal it is not possible to distinguish between the crystal and the transformed crystal.

Since the Laplace operator is always invariant with respect to translations and rotations, it follows for a particle in a lattice periodical potential with the Hamiltonian

$$\hat{H}(\vec{r}) = -\frac{\hbar^2\nabla^2}{2m_e} + \hat{V}(\vec{r}), \qquad m_e = \text{free electron mass} \tag{2.37}$$

that its $\hat{H}$ operator is always invariant with respect to transformations of the crystal's space group, what can mathematically be expressed by:

$$\left[\hat{S}_{\{\tau|\vec{t}\}}, \hat{H}(\vec{r})\right] = 0. \tag{2.38}$$

of a group, the corresponding Schrödinger equation has to be invariant respective to the symmetry operations of that group. Wigner [26] theorem, eigenvalue of the Hamiltonian belongs to a irreducible representation of symmetry group, and that the corresponding eigenfunctions transform commensurate to the symmetry operations

2.4.1 The Space Group

As indicated above the total number of symmetry operations $\hat{S}_{\{\tau|\vec{t}\}}$ which leave a crystal invariant are forming a group, where the multiplication is defined as a successive execution of group elements. The operator τ represents a transformation, where at least one point of the crystal is left unchanged and the vector $\vec{t}$ consists of linear combinations of primitive ($\vec{R}_n$) and (or) non primitive translations ($\vec{u}$). The point group $P = \{\tau|0\}$ only consists of the rotational parts of the group elements τ, which may be proper as well as unproper[5] rotations.

The periodicity of a crystal (see Sec. 2.2) is mathematically taken into account by the corresponding translation group $T = \{\mathbb{1}|\vec{R}_n\}$. The order of the in principle infinite translation group may be restricted by cyclic boundary conditions to $N = N_1N_2N_3$. The space group itself is constructed then by all possible combinations of elements of P with vectors $\vec{t}$:

$$\hat{S}_{\{\tau|\vec{t}\}} = \left\{\tau \in P_\tau, \qquad \vec{t} = \vec{R}_n + \vec{u}\right\} \tag{2.39}$$

If the set of vectors $\vec{t}$ does not include non-primitive translation vectors $\vec{u}$ the space-group is termed symmorphic otherwise nonsymmorphic. A nonsymmorphic space group contains additional symmetry elements like screw axis and glide planes, which are formed by elements of P and non primitive translation vectors $\vec{u}$.

[5] An unproper rotation is a proper rotation followed by an inversion.

The Representation of the Point Group

The representation of a group is understood as a homomorphic mapping of a group to a group of matrices. In order to get a representation of the point group P, each of its symmetry operations is then identified by an appropriated matrix $D(\tau)$. The set of matrices $D(\tau)$ also forms a group, its elements fulfill the same relations like the elements of the point group P. If the matrix representations $D(\tau)$ build an Abelian[6] group, it is possible to find a transformation matrix U such that

$$D'(\tau) = UD(\tau)U^{-1} = \begin{pmatrix} D^{(1)}(\tau) & \dots & 0 \\ \vdots & \ddots & \vdots \\ 0 & \dots & D^{(m)}(\tau) \end{pmatrix}. \tag{2.40}$$

U diagonalizes the matrix representations simultaneously. $D(\tau)$ is termed the reducible and $D'(\tau)$ the irreducible representation. In the case of a non-Abelian group it is only possible to find a unitary matrix which transforms all regular matrices to the generalized form:

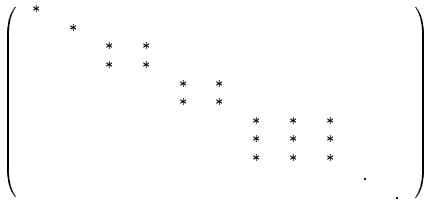

This expression is a reduced representation decomposed into irreducible submatrices of dimension 1, 2, and 3, which are placed along the main diagonal[7]. Now some group theoretical definitions and theorems will be presented which will be proven to be useful during the next sections:

1. The dimension of a representation matrix is the dimension of the representation.

2. For each group there exists an infinite number of representations, which can be described like the transformation of coordinates:

$$x'_i = \sum_{k=1}^{n} D_{ik}(\tau)x_k \tag{2.41}$$

   Thereby it is supposed that the matrices $D_{ik}(\tau)$ form a group and that the n coordinates are orthogonal and linear independent. These conditions are fulfilled if during a transformation according to (2.41) for each τ of

[6] A group is called Abelian if its elements satisfy the commutative law with respect to the multiplication operation.

[7] For crystals the maximum dimension of a submatrix of an irreducible representation is 3.

P the n coordinates x_k are totality mapped to the coordinates x'_k. The primed coordinates are thus linear combinations of the primary ones. The coordinates x_k are also called a basis of the n-dimensional representation $D_{ik}(\tau)$.

3. The traces of the representation matrices are invariant with respect to orthogonal transformations. Therefore they characterize each particular symmetry element. Accordingly they are called the *characters* of a representation.

4. Each group G can be divided into classes which are defined as follows: An element $b \in G$ is said to be *conjugate* to $a \in G$ if there exists another group element $p \in G$ such that $b = pap^{-1}$. Elements of a group which are conjugate to each other are said to form a class. The characters of elements which belong to the same class are equal.

5. There exists a well defined number of representations with the smallest possible dimension. These are the irreducible ones. The number of irreducible representations $D^{(i)}$ is equal to the number of classes. Each reducible representation may be composed of the irreducible representations according to:

$$D(\tau) = \sum n_i D^{(i)}(\tau) \tag{2.42}$$

6. The irreducible representations are labeled by the Mullikan symbols A, B, E, and F with the indices 1, 2, g, and u, and the superscripts ' and ". These symbols have the following meaning: A and B are one-dimensional representations, either symmetric or unsymmetric with respect to the main rotation axis. E and F are two- or three-dimensional representations, g and u stand for even (gerade) and odd (ungerade) with respect to the center of inversion. 1 and 2 denote symmetry or antisymmetry with regard to a side rotoreflection axis or a mirror plane. Finally ' and " refer to an additional symmetry or antisymmetry with respect to a further mirror plane. The irreducible representations of the 32 point groups and the corresponding characters can be found e.g. in the book of Kuzmany [27].

The Representation of the Translation-Group

For the representation of the translation group $\widehat{T}$ the Taylor expansion of a general function $f(\vec{r}) = f(x, y, z)$ around $x = x_0$

$$f(x, y, z) = \sum_{\nu=0}^{\infty} \frac{1}{\nu!} \Big[\frac{\partial^\nu f(x, y, z)}{\partial x^\nu} \Big]_{x=x_o} (x - x_o)^\nu \tag{2.43}$$

serves as a starting point. If now x it is set to $x = x_0 + a$ one yields

$$f(x_0 + a, y, z) = \sum_{\nu=0}^{\infty} \frac{1}{\nu!} \Big[\frac{\partial^\nu f(x, y, z)}{\partial x^\nu} \Big]_{x=x_0} a^\nu. \tag{2.44}$$

This expression is valid for any arbitrary x_0 and also for $x = x_0$ and this may be written in the form

$$f(x + a, y, z) = \sum_{\nu=0}^{\infty} \frac{1}{\nu!} \Big[a \frac{\partial}{\partial x} \Big]^\nu f(x, y, z). \tag{2.45}$$

Taking into account the momentum operator $\hat{p} = -i\nabla$ ($\hbar \equiv 1$) leads to

$$f(x + a, y, z) = \sum_{\nu=0}^{\infty} \frac{1}{\nu!} \Big[ia\hat{p}_x \Big]^\nu f(x, y, z). \tag{2.46}$$

Moreover, if a, b, c are understood as components of a vector $\vec{R}_n$ one obtains

$$\begin{aligned} f(x + a, y + b, z + c) &= e^{i(a\hat{p}_x + b\hat{p}_y + c\hat{p}_z)} f(x, y, z) \\ f(\vec{r} + \vec{R}_n) &= e^{i\vec{R}_n \hat{p}} f(\vec{r}) = e^{i\vec{R}_n \vec{q}} f(\vec{r}) = D f(\vec{r}), \end{aligned} \tag{2.47}$$

where $\vec{q}$ are the eigenvalues of of the operator $\hat{p}$. Equation (2.47) shows that a representation of the translation symmetries is realized by the operator D (Bloch factor) which may be expressed by[8]

$$D^{\hat{p}} = D^{\vec{q}} = e^{i\vec{q}\vec{R}_n}, \tag{2.48}$$

where

$$\vec{q} = \frac{m_1}{N_1}\vec{b}_1 + \frac{m_2}{N_2}\vec{b}_2 + \frac{m_3}{N_3}\vec{b}_3 \qquad (0 \leq m_i \leq N_i - 1), \tag{2.49}$$

and

$$\vec{b}_i = 2\pi \frac{\vec{a}_j \times \vec{a}_k}{|\vec{a}_i \cdot (\vec{a}_j \times \vec{a}_k)|}, \qquad (i, j, k = 1, 2, 3) \tag{2.50}$$

are the reciprocal lattice vectors. Another fact which can be easily seen in equation (2.47) is that the group of the representations of T is Abelian and that therefore the dimensions of the irreducible representations of T have to be one. This fact allows us to formulate the irreducible representation of the space group $P \bigotimes T$ in such a way that the translational part can be factorized, what leads to

$$D^{\vec{q}(\{\tau'|\vec{t}(\tau')\})} = e^{i\vec{q}\cdot\vec{R}_n} D^{\vec{q}(\{\tau'|\vec{u}(\tau')\})} = D^{\vec{q}(\{\tau'|\vec{u}(\tau')\})}, \tag{2.51}$$

[8] $\hat{p}$ can be replaced by $\vec{q}$ as a quantum number, which labels the different states if $f(x, y, z)$ in equation (2.47) is replaced by a wave function $\psi(\vec{r})$.

where $D^{\vec{q}}$ is the representation of the group of the vector $\vec{q}$, and τ' stands for all rotations, which leave the vector $\vec{q}$ invariant. This gives rise to a justification of the procedure described in section 2.2 (equations (2.14)-(2.17)). Equation (2.51) describes the fact that the representation of a space group for $\vec{q} = 0$ is identical to the representation of the crystal point group[9].

In section 2.3 normal coordinates Q_j have been introduced, which transformed the total energy to (see 2.24):

$$E = \frac{1}{2} \sum_{\substack{j=1,\ldots,n_j \\ f=1,\ldots,n_f}} \dot{Q}_{j,f}^2 + \sum_{j=1,\ldots,n_j} \omega_j^2 \sum_{f=1,\ldots,n_f} Q_{j,f}^2 \quad , \tag{2.52}$$

where n_j is the total number of modes and n_f is the order of degeneracy of the mode j. Since the application of space group operations to a crystal should not change the total energy, all Q_j have to be mapped to themselves or to $-Q_j$. In case of degenerate modes all $Q_{j,f}$ have to be mapped among each other allowing for a change of sign. Therewith the normal coordinates are building a basis for a representation of the point group P according to equation (2.41). Corresponding to the number of normal coordinates the representation is $3N$-dimensional and therefore reducible, and it can be fragmented into the irreducible representations of the point group P, what will be shown in the next section. **All vibrations including translations and rotations can be classified by the irreducible representations of the point group P.** Therefore a certain vibration can be assigned to a specific symmetry type or species. The vibrations are also labeled with Mullikan symbols according to the irreducible representations.

2.4.2 Group Analysis of Normal Modes Regarding $q = 0$

The kinematics of the Raman scattering may be characterized in the following way: An incident photon is destroyed; simultaneously another photon with slightly higher or lower energy is created and emitted. Thereby the wavevectors of the photons $\vec{k}_{in} \approx \vec{k}_{out} \approx 10^5$ cm^{-1} are much smaller than the Brillouin zone size $(\frac{2\pi}{a_i}) \approx 10^8$ cm^{-1} of the solid. This is the reason why considering Raman scattering and infrared absorption of first order, momentum conservation can only be fulfilled if $q \approx 0$. This fact simplifies the analysis of the Raman active normal modes, which can be restricted to the center of the Brillouin zone (Γ-point). These kinds of vibrations are equal in any unit cell of the crystal and therefore it is possible to get the number of vibrations and their spectroscopic selection rules from the so called factor-group analysis.

Counting of the Γ-Point Normal Modes

[9] It is possible to show that $D^{\vec{q}}(\{\tau'|\vec{u}(\tau')\}) = e^{-i\vec{q}\cdot\vec{u}(\tau')} D^{\vec{q}}(\tau')$ holds for non-symmorphic groups.

In order to classify the vibrations it is not necessary to know one of the infinitely many $3N$-dimensional representations and to evaluate equation (2.41) explicitly. It is enough to calculate the traces $\chi(\tau)$ of the representation matrices. Furthermore, a simple consideration reveals, that only those coordinates, which are transformed via the main diagonal elements are not changed by symmetry operations of the point group P.

The simplest transformation matrix is given by

$$\tau = \begin{pmatrix} \cos\phi & -\sin\phi & 0 \\ \sin\phi & \cos\phi & 0 \\ 0 & 0 & \pm 1 \end{pmatrix}, \tag{2.53}$$

which describes a rotation with respect to the z-axis with the rotation angle $\phi = 2\pi/n$ ($n = 1, 2, 3, 4, 6$). The $+$ sign in τ_{33} stands for proper rotations (E, C_n) and the $-$ sign for the improper rotations (σ_n, I). Note that this matrix only has this simple form if the coordinate system and the rotation axis are chosen in a special way, otherwise (2.53) has to be transformed according to an orthogonal transformation. In this case, as before, only the trace is left invariant.

The traces may now be used to calculate the characters: The character $\chi^{red}(\tau)$ of the τ-th symmetry operation of the $3r$ dimensional representation is given by

$$\chi^{red}(\tau) = r_c(\tau)(\pm 1 + 2\cos\phi), \tag{2.54}$$

where $r_c(\tau)$ is the number of atoms which are left invariant. If all characters $\chi^{red}(\tau)$ are obtained in this manner one can get a classification of all possible vibrations according to the symmetry with the help of

$$n_{irred} = \frac{1}{g} \sum_{\substack{\text{over} \\ \text{all classes}}} n_\tau \chi^{red}(\tau)\chi^{irred}(\tau). \tag{2.55}$$

Here g is the order of the point group and n_τ is the number of elements in the class for which the operation τ is a representative. termed as the total representation Since the normal coordinates of pure translations and pure rotations correspond to transformations of coordinates and axial vectors, they can be easily factorized from the total number of normal vibrations. They are often denoted as x, y, z (translations) and X, Y, Z (rotations) in the character tables.

Quantum Mechanical Selection Rules

Via the classification of lattice vibrations and the help of group theory it is also possible to determine the selection rules for the optical transitions [28, 29], and thus get an assistance in the assignment of the experimentally observed phonon modes. These selection rules also predict, which of the modes are infrared active

or Raman active, and in which kind of experimental geometry (polarization) they can be observed. For an optical transition, the transition probability per unit time W is given by Fermi's golden rule

$$W = \frac{2\pi}{\hbar}|M_{fi}|^2\delta(E_f - E_i), \tag{2.56}$$

where

$$M_{fi} = \int \psi_f^\star \hat{H}'\psi_i d\vec{r} \tag{2.57}$$

is the matrix element of the perturbation $\hat{H}'$, which induces a transition between the states i and f. The integral is simply reduced to the form

$$\int \psi_f^\star d_\sigma \psi_i d\vec{r} \tag{2.58}$$

in case of absorption or emission, and to

$$\int \psi_f^\star \alpha_{\sigma\rho}\psi_i d\vec{r} \tag{2.59}$$

for Raman scattering, where d_σ are the components of the dipole moment of the vibration and $\alpha_{\sigma\rho}$ are the components of the polarizibility tensor. A selection rule can be derived from equations (2.58) or (2.59) taking into account that those integrals vanish in case of a centrosymmetrical system if the integrands are odd functions. In a general group theoretical treatment the integrals are written as direct products of the form

$$\overline{\psi}_f \otimes M \otimes \psi_i. \tag{2.60}$$

The product generally transforms according to some reducible representation. It will have a non-zero value only if it contains the totally symmetric irreducible representation of the considered point group. Applied to the point group of a given crystal this means

$$\frac{n_\tau}{g}\sum_\tau \overline{\chi_j^f}(\tau)\cdot\chi^M(\tau)\chi_j^i(\tau) \neq 0, \tag{2.61}$$

where $\chi^M(\tau) = \chi^d(\tau)$ and $\chi^M(\tau) = \chi^\alpha(\tau)$ in the case of Infrared and Raman spectroscopy, respectively. Due to the fact that d and α transform like Cartesian coordinates and products of those coordinates, respectively, one yields

$$\chi^d(\tau) = \pm 1 + 2\cos\phi \tag{2.62a}$$

and

$$\chi^\alpha(\tau) = 2\cos\phi(\pm 1 + 2\cos\phi). \tag{2.62b}$$

In these expression the $-$ sign refers to the proper and the $+$ sign to the unproper rotations of the point group. It is assumed that either the initial state or the final state of the transition is the total symmetric ground state, a fact which simplifies equation (2.61). For a one-phonon process regarding inversion symmetry one gets those vibrations which are odd with respect to the center of inversion as Raman-forbidden but infrared-allowed and vice versa. Equations (2.62a) and (2.62b) present the conditions for infrared and Raman activity without answering the question, which components of d_σ or $\alpha_{\sigma\rho}$ are different from zero. By replacing $\chi^M(\tau)$ by its irreducible components one can easily find those components which are non-zero and investigate their relation to each other.

Determination of the Symmetry and the Normal Coordinates

Until now a tool to classify the eigenvibrations of a crystal according to its irreducible representations has been presented. However, one can also determine those vectors which describe the possible displacements of the atoms for each irreducible representation. In order to do so, one has to find the irreducible representations of the total displacement $\vec{U}$ of the atoms in the unit cell which form the basis for the reducible representation $D(\{\tau|\vec{v}(\vec{R})\})$. This factorization may be done with the help of so called projection operators $\hat{P}$.

Assuming the vectors of the coordinate system (the Cartesian displacements coordinates) are represented by $f(\vec{r})$ [30], then a projection operator P_k which projects out the part of $f(\vec{r})$ which belongs to the irreducible representation Γ_k can be defined as:

$$P_k f(\vec{r}) = g \sum_i \chi(\tau_i)\tau_i f(\vec{r}) \tag{2.63}$$

If the Cartesian displacement coordinates of all the atoms $\vec{U}$ are taken now as $f(\vec{r})$ the eigenvector can be obtained if only one set of eigenvibrations transforms like a certain irreducible representation. However, if several modes transform like a certain irreducible representation, one can only obtain the symmetry coordinates which are linear combinations of the eigenvectors. In this case the eigenvectors cannot be directly determined via the projection technique. In order to obtain them one has to diagonalize the dynamical matrix (see equation (2.17)[10].

[10]The factor-group analysis can also be performed with the help of the so called tabular method, which is described in Reference [31]. If one wants to make use of this method one has to know the number of atoms in the unit cell and their crystallographic positions as well as the space group of the crystal.

Chapter 3

Theory of Raman Scattering

This chapter starts with a short introduction to the general features of light scattering experiments. The main part, however, will focus on a detailed theoretical description of the Raman scattering process regarding a macroscopic as well as a microscopic point of view. Finally, at the end of this chapter formulas will be derived, which allow to calculate Raman spectra of crystalline materials starting from the total energy surface and the derivatives of the dielectric tensor.

3.1 Light Scattering

As known from many textbooks [32] a perfect optical homogeneous medium does not scatter light. Only inhomogeneities in the order of the wavelength of light passing through the crystal give raise to scattering of the radiation into different space directions. If these inhomogeneities only have local character, the scattering is elastic, what means that there is no change in the wavelength between incident and scattered light. According to size and kind of the inhomogeneities the scattering process is termed as Tyndall-, Mie-, or Rayleigh scattering. However, if the inhomogeneities show time-dependent fluctuations, then the scattering is inelastic. Raman and Brillouin scattering belong to this category, where a change in the frequency between incident and scattered light appears. In this case, the spectroscopy of the scattered light gives information about the electronic and the vibrational states of the observed medium. This is the reason why the main interest concerning Raman spectroscopy lies in the spectral distribution of the scattered light relative to the incident one.

Dealing with Raman or Brillouin scattering the frequency of the scattered light is pretty close to the one of the incident light, and the intensity of the scattered light is very small compared to the initial light beam. These facts makes the experimentalist use a laser to generate the incident light. In order to detect the scattered light in case of Raman or Brillouin scattering a photon counting system is often used, because of the very low intensities of 10 to 100

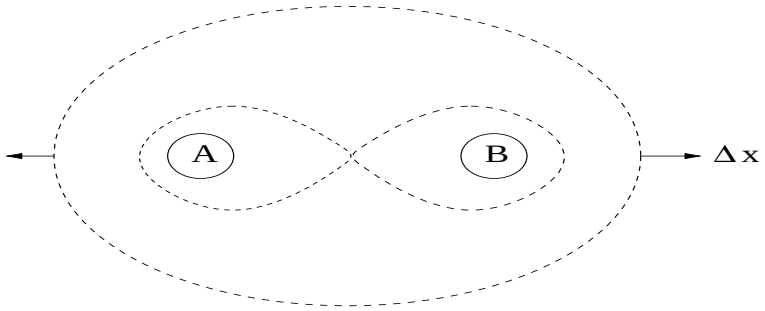

Figure 3.1: Model of a two-atomic molecule

photons per second.

3.1.1 A General View on Raman Spectroscopy

Raman scattering is based on a change in the polarizability and in the susceptibility of a crystal caused by quasi-particles. In case of phonon Raman scattering, the modulation of the dielectric function ϵ by phonons gives rise to the observed Raman effect.

A very good example to demonstrate and to understand the Raman effect in principle is a diatomic molecule: The polarizability α_0 of the orbitals (shown in Figure 3.1) results in the polarization $p(\omega) = \alpha_0 E(\omega)$, if an electric field $E(\omega)$ is applied to the molecule. As long as α_0 is constant in time, an incident electromagnetic wave will propagate linearly according to Huygen's principle. However, if α_0 is modulated by a vibrational induced change of the positions of the nuclei, one yields

$$p = [\alpha_0 + \alpha_1 \cos(\omega_v t)] E_0(\omega t) \tag{3.1}$$

with the assumption of a $\cos(\omega_v t)$ vibration. The application of trigonometric formulas to equation(3.1) then leads for $E_0(\omega t) = E_0 \cos(\omega t)$ to:

$$p = \alpha_0 E_0(\omega t) + \frac{\alpha_1 E_0}{2}\{\cos[(\omega + \omega_v)t] + \cos[(\omega - \omega_v)t]\} \tag{3.2}$$

As can be seen, the light now consists of three different parts: one part which keeps the frequency of the incident light, which is always the strongest in intensity, and two additional parts with their frequencies shifted by $\pm\omega_{ph}$ relative to the incident frequency. Concerning a crystalline lattice, there is an additional complication due to the fact that the contributions of different elementary cells to the resulting scattering intensity may interfere. It can be shown, that in this case constructive interference only occurs, if the condition

$$2\Lambda \sin\frac{\Theta}{2} = \frac{\lambda}{n} \tag{3.3}$$

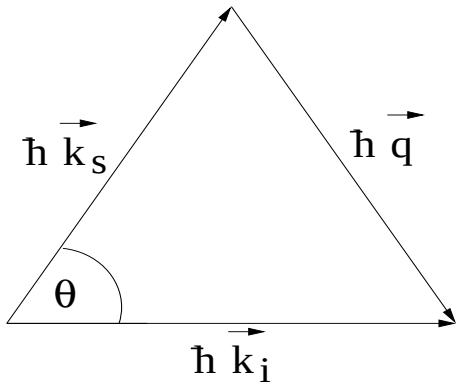

Figure 3.2: Conservation of the momentum in a scattering process.

is satisfied. Thereby Λ stands for the wavelength of the phonon, while λ is the wavelength of the incoming photon. Furthermore, n specifies the refraction index, and Θ describes the angle between the incident and the scattered light. This formulation corresponds to the conservation laws of the total momentum and the total energy in the quantum-mechanical description of a scattering problem. Here, the Raman as well as the Brillouin scattering may be described by an absorption and an emission process of a phonon or another quasi-particle where the conservation laws read

$$\hbar\omega_s = \hbar\omega_i \pm \hbar\omega_{ph}, \tag{3.4a}$$

$$\hbar\vec{k}_s = \hbar\vec{k}_i \pm \hbar\vec{q}. \tag{3.4b}$$

The indeces i and s refer to the incident and the scattered light, respectively. In solids, where vibrations are phonons, ω_{ph} is written instead of ω_v. It should be recalled again that in the case of Raman scattering only scattering processes with very small q are taken into account. The maximal q one can obtain is given by 180° backward scattering, where $\vec{q}_{max} = \vec{k}_i - \vec{k}_s \approx 2\vec{k}_i$ (see Figure 3.2). Regarding the fact, that in terms of Raman scattering $\vec{k}_i$ lies in the visible spectral region being of the order of 10^5 cm^{-1}, this leads to $|\vec{q}| \approx 0$, i.e. phonons of the Brillouin zone center, as it can be seen in Section 2.4.2. Depending on whether a quasi-particle is absorbed or emitted the scattered light has a higher or lower frequency than the incident light. The former case is called an anti-Stokes process whereas the latter one is termed Stokes scattering.

Another criterion, which may be very useful in the assignment of the Raman spectra to phonon modes is the fact, that if a phonon participates in the Raman process the polarizability of the considered crystal or molecule has to be changed. It is not self-evident that this happens in each vibration. Generally it can be

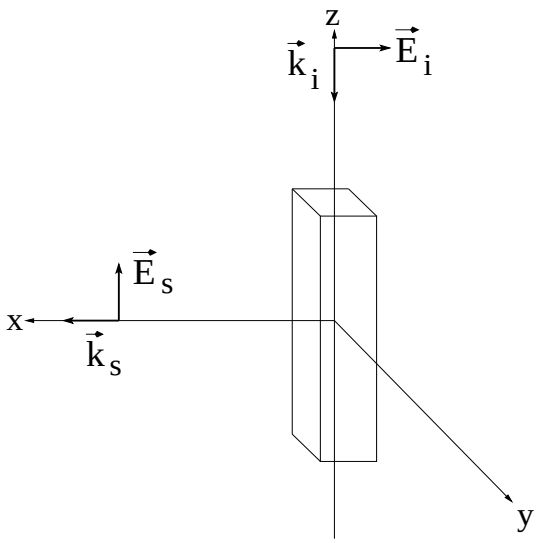

Figure 3.3: Typical geometrical arrangement for a Raman scattering experiment.

said that vibrations which induce a dipole moment are infrared active and those which change the polarizability are Raman active. All other vibrations are called silent modes. The classification of the phonons in Raman-active and infrared-active vibrations matches exactly the group theoretical selection rules derived in Section 2.4.2.

The intensity of the light in the side bands of the spectrum is proportional to the intensity of the incident light, thus the ratio of those intensities may be written in the form of a scattering cross section:

$$\begin{aligned} \frac{d\sigma}{d\Omega} &= \frac{1}{I_i}\frac{dP_s}{d\Omega} \quad \text{(differential scattering cross section)} \\ S &= \frac{1}{V_s}\frac{d\sigma}{d\Omega} \quad \text{(Raman scattering cross section).} \end{aligned} \tag{3.5}$$

Here dP_s describes the emitted light power (in Watt) into a solid-angle element $d\Omega$, $I_i = P_i/F$ the incident light power per unit area (in Watt/m^2) and V_s the scattering volume.

3.1.2 Symmetry and Nomenclature

In order to explicitly calculate the scattering intensity it is the best way to start from a well defined scattering geometry as shown in Figure 3.3. The light comes in from z-direction and is observed in x-direction, therefore the scattering plane is the xz-plane. For this given scattering geometry the incident light can only be x- or y-polarized, whereas for the observation of the scattered light one can

only expect z- or y-polarization. In the description of the scattering process it is common to refer to the scattering plane and to label the orientations of the scattered light with $\parallel$ and $\perp$ relative to this plane. A more detailed description of the scattering geometry, shown in Figure 3.3, can be achieved by labeling the directions and polarizations of incident and observed light by coordinates of the form

$$a(bc)d. \tag{3.6}$$

In this notation, the letters refer to the axis of an orthogonal coordinate system. a and d specify the directions of incident and scattered light, respectively, whereas b and c label the corresponding polarizations. In Figure 3.3 the notation has the form $\bar{z}(\bar{x}z)x$. The contribution of the Raman tensor $\chi^{\eta\sigma}(\zeta)$ of the ζ-th mode to the scattering intensity may be written in the following form:

$$I(\zeta) = C' \Big| \sum_{\eta,\sigma} e_s^{\eta} \chi^{\eta\sigma}(\zeta) e_i^{\sigma} \Big|^2. \tag{3.7}$$

This relation shows immediately that a specific component of the Raman tensor is determined by choosing the appropriate polarizations for incident and scattered light.

3.2 Macroscopic Theory of Light Scattering

The description below follows References [33] and [34] with the aim to calculate Raman spectra from observables which can be directly obtained from frozen-phonon ab initio band structure calculations. In the following it is assumed that the incident light is laser light and therefore the index i (for incident light) is always replaced by the index L (for incident laser light).

The simplest way to establish the relation between the scattered radiation and the dielectric function is to study the scattered radiation field at a long distance R with the polarization vector $\vec{e}_s$ according to an oscillating dipole moment represented by its second derivative $\ddot{\vec{p}}_s(t)$:

$$E_s\Big(t + \frac{R}{c}\Big) = \frac{1}{4\pi\epsilon_0 c^2 R} \vec{e}_s \ddot{\vec{p}}_s(t) \tag{3.8}$$

ϵ_0 and c are the vacuum permittivity and the velocity of light, respectively. Within one unit cell with volume V_E the η component of the dipole moment $\vec{p}_s$ induced by the ξ component of the applied laser field E_L with the polarization vector $\vec{e}_L$ is

$$p_s^{\eta}(t) = V_E \epsilon_0 \big(\epsilon^{\eta\xi}(t) - \delta^{\eta\xi}\big) E_L(t) e_L^{\xi}, \tag{3.9}$$

where $\epsilon^{\eta\xi}(t)$ is the complex dielectric tensor.

As mentioned in the previous section inelastic scattering is caused by time fluctuations of the dielectric function. Thus the non-fluctuating part $\delta^{\eta\xi}$ does not contribute. Taking the ω_s Fourier component indicated by the brackets $[\,]_{\omega_s}$ the second derivative of the oscillating dipole moment at frequency ω_s for one elementary cell reads:

$$\ddot{p}_s^{\eta}(t) = V_E \epsilon_0 \omega_s^2 \left[\epsilon^{\eta\xi}(t) E_L(t) e_L^{\xi}\right]_{\omega_s}. \tag{3.10}$$

The time-fluctuations of the dielectric function at the incident laser frequency ω_L can be expanded into a Fourier series. Considering the spatial-dependence of E_L, $\epsilon^{\eta\xi}$, and E_s the scattered radiation field E_s for one elementary cell at position $\vec{R}_n$ is obtained

$$E_s\left[\omega_s\Big(t+\frac{R}{c}\Big), \vec{k}_s\big(\vec{R}-\vec{R}_n\big)\right] = \frac{V_E\omega_s^2}{4\pi c^2 R}\left[\sum_{\omega,\vec{k}} e_s^{\eta}\epsilon_{\omega_L}^{\eta\xi}\left(\omega t, \vec{k}\vec{r}_l\right) e_L^{\xi} E_L\left(\omega_L t, \vec{k}_L\vec{R}_n\right)\right]_{\omega_s}. \tag{3.11}$$

Fluctuations of the dielectric function in time and space are considered by the Fourier components ω and $\vec{k}$ which are related by the dispersion relation $\omega(\vec{k})$ of the quasi-particle causing the fluctuations. In the same way the frequencies ω_L and ω_s and the wavevectors $\vec{k}_L$ and $\vec{k}_s$ of incident and scattered radiation, are related. The long-time average of equation (3.11) directly results in the energy conservation $\omega_s = \omega_L \pm \omega$. Since, in the solid the phonon has a coherence volume consisting of N_c elementary cells (with volume V_E), the scattered radiation field E_s has to be summed over these N_c cells because they all contribute in a certain phase relation.[1] For finite N_c (3.11) becomes:

$$E_{s,\vec{k}_s}\left(\omega_s\Big(t+\frac{R}{c}\Big)\right) = \frac{N_c V_E\omega_s^2}{4\pi c^2 R}\left[\sum_{\omega(\vec{k})} e_s^{\eta}\epsilon_{\omega_L}^{\eta\xi}\left(\omega_{\vec{k}}t\right) e_L^{\xi} E_{L,\vec{k}_L}\left(\omega_L t\right)\right]_{\omega_s} \tag{3.12}$$

Using the time average indicated by the brackets $\langle\rangle$ and the relation

$$dP_s = c\epsilon_0\langle E_s, E_s^*\rangle R^2 d\Omega \tag{3.13}$$

the scattered power dP_s per solid angle $d\Omega$ is obtained for the scattering volume V_s:

$$\frac{dP_s}{d\Omega} = \frac{V_s N_c V_E \epsilon_0 \omega_s^4}{(4\pi)^2 c^3}\left\langle \sum_{\omega(\vec{k})} e_s^{\eta}\epsilon_{\omega_L}^{\eta\xi}\left(\omega_{\vec{k}}t\right) e_L^{\xi} E_L(\omega_L t), \sum_{\omega(\vec{k})} e_s^{\eta}\epsilon_{\omega_L}^{\eta\xi *}\left(\omega_{\vec{k}}t\right) e_L^{\xi} E_L^*(\omega_L t)\right\rangle_{\omega_s}. \tag{3.14}$$

It is assumed that there are several coherence volumina $N_c V_E$ in the scattering volume V_s incoherently contributing to the total scattered radiation. Therefore,

[1] This is performed by integrating $\vec{R}_n$ over the coherence volume $N_c V_E$. In the limit $N_c \to \infty$ the momentum conversation ($\vec{k}_s = \vec{k}_L \pm \vec{k}$) is obtained.

the total scattered power is increased by the factor V_s/N_cV_E. The Raman efficiency S is defined with the help of the differential cross section $d\sigma/d\Omega$

$$S = \frac{1}{V_s}\frac{d\sigma}{d\Omega}. \tag{3.15}$$

Introducing the quantity $e_L^\xi(\omega_L t)$ which is the normalized electric field containing the polarization and variations in time

$$e_L^\xi E_L(\omega_L t) = |E_L| e_L^\xi(\omega_L t), \tag{3.16}$$

and using the relation between differential cross section, power and laser intensity I_L

$$\frac{dP_s}{d\Omega} = \frac{d\sigma}{d\Omega}\frac{\omega_s}{\omega_L} I_L \tag{3.17}$$

$$I_L = c\epsilon_0 |E_L|^2 \left\langle e_L^\xi(\omega_L t), e_L^{\xi *}(\omega_L t) \right\rangle \tag{3.18}$$

the Raman cross section finally reads

$$S(\omega_s) = \frac{N_c V_E \omega_L \omega_s^3}{(4\pi)^2 c^4} \frac{\left\langle \sum_{\omega(\vec{k})} e_s^\eta \epsilon_{\omega_L}^{\eta\xi}(\omega_{\vec{k}} t) e_L^\xi(\omega_L t), \sum_{\omega(\vec{k})} e_s^\eta \epsilon_{\omega_L}^{\eta\xi *}(\omega_{\vec{k}} t) e_L^{\xi *}(\omega_L t), \right\rangle_{\omega_s}}{\left\langle e_L^\xi(\omega_L t), e_L^{\xi *}(\omega_L t) \right\rangle} \tag{3.19}$$

or in other notation [32]

$$S_{\omega_s}^{\eta\xi} = \frac{N_c V_E \omega_l \omega_s^3}{(4\pi)^2 c^4} \left\langle \delta\epsilon^{\eta\xi}, \delta\epsilon^{\eta\xi *} \right\rangle_{\omega_s}. \tag{3.20}$$

If the time fluctuations of the dielectric tensor are caused by phonons they can be described classically by the derivative of the dielectric tensor with respect to the phononic normal coordinate $\partial\epsilon^{\eta\xi}/\partial Q_{\omega_{\vec{k}_L}}$ and the phonon amplitude $Q^0_{\omega_{\vec{k}}}$. The time average of the ω_s Fourier component of the scattered light intensity normalized to the time averaged laser intensity is given in the classical limit by

$$\left\langle \partial\epsilon^{\eta\xi}, \partial\epsilon^{\eta\xi *} \right\rangle_{\omega_s} = \left[\frac{1}{2} \frac{\partial\epsilon^{\eta\xi}(\omega_L, \vec{k}_L)}{\partial Q_{\omega_{\vec{k}_L}}} Q^0_{\omega_{\vec{k}_L}} \right]^2_{\omega_s = \omega_L \pm \omega}. \tag{3.21}$$

This expression fails, however, to reproduce the correct intensity ratio between Stokes ($\omega_s = \omega_L - \omega$) and anti-Stokes scattering ($\omega_s = \omega_L + \omega$), since in the classical limit both processes have the same intensities (see equation 3.2).

3.3 Microscopic Theory of Light Scattering

In order to go beyond the classical treatment one has to consider that equation (3.20) only expresses some general relation between the fluctuations in the dielectric function and the Raman efficiency. It can also be evaluated quantum-mechanically by calculating the expectation value of the fluctuations in the dielectric function caused by transitions between the eigenstates $|i\rangle$ and $|f\rangle$:

$$\left\langle \partial\epsilon^{\eta\xi}, \partial\epsilon^{\eta\xi *} \right\rangle_{\omega_s} = \left| [\epsilon^{\eta\xi}_{i\to f}]_{\omega_s=\omega_L-\omega_{if}} \right|^2 \tag{3.22}$$

For that purpose, first the dielectric function $\epsilon^{\eta\xi}_{\omega_L}$ has to be expanded with respect to $Q_{\omega_{\vec{k}}}$

$$\epsilon^{\eta\xi}_{\omega_L}\left(Q_{\omega_{\vec{k}}}\right) = \epsilon^{\eta\xi}_{\omega_L}\Big|_0 + \sum_{\omega(\vec{k})} \frac{\partial\epsilon^{\eta\xi}_{\omega_L}}{\partial Q_{\omega_{\vec{k}}}}\bigg|_0 Q_{\omega_{\vec{k}}} + \frac{1}{2}\sum_{\omega(\vec{k})}\sum_{\omega'(\vec{k}')} \frac{\partial^2\epsilon^{\eta\xi}_{\omega_L}}{\partial Q_{\omega_{\vec{k}}}\partial Q_{\omega'_{\vec{k}'}}}\bigg|_0 Q_{\omega_{\vec{k}}} Q_{\omega'_{\vec{k}'}} + \cdots \tag{3.23}$$

Using equation (3.23) and assuming that the system can be split into states $|\mu\rangle$ and $|\nu\rangle$ depending on the parameter Q and a state $|g\rangle$ with matrix elements independent of Q one obtains:

$$\begin{aligned}
\left[\epsilon^{\eta\xi}_{i\to f}\right]_{\omega_s} &= \left\langle f \middle| \epsilon^{\eta\xi}_{\omega_L} \middle| i \right\rangle_{\omega_s=\omega_L-\omega_{if}} \\
&= \sum_n \frac{1}{n!} \sum_{\omega_{\vec{k}}} \cdots \sum_{\omega^{(n)}_{\vec{k}(n)}} \left\langle g\nu \middle| \frac{\partial^n \epsilon^{\eta\xi}_{\omega_L}}{\partial Q_{\omega_{\vec{k}}} \ldots \partial Q_{\omega^{(n)}_{\vec{k}(n)}}} \hat{Q}_{\omega_{\vec{k}}} \ldots \hat{Q}_{\omega^{(n)}_{\vec{k}(n)}} \middle| g\mu \right\rangle_{\omega_s=\omega_L-\omega_{\mu\nu}} \\
&\sim \sum_n \frac{1}{n!} \sum_{\omega_{\vec{k}}} \cdots \sum_{\omega^{(n)}_{\vec{k}(n)}} \left\langle g \middle| \frac{\partial^n \epsilon^{\eta\xi}_{\omega_L}}{\partial Q_{\omega_{\vec{k}}} \ldots \partial Q_{\omega^{(n)}_{\vec{k}(n)}}} \middle| g \right\rangle \left\langle \nu \middle| \hat{Q}_{\omega_{\vec{k}}} \ldots \hat{Q}_{\omega^{(n)}_{\vec{k}(n)}} \middle| \mu \right\rangle_{\omega_s=\omega_L-\omega_{\mu\nu}} \\
&\sim \sum_n \frac{1}{n!} \sum_{\omega_{\vec{k}}} \cdots \sum_{\omega^{(n)}_{\vec{k}(n)}} \frac{\partial^n \epsilon^{\eta\xi}_{\omega_L}}{\partial Q_{\omega_{\vec{k}}} \ldots \partial Q_{\omega^{(n)}_{\vec{k}(n)}}} \left\langle \nu \middle| \hat{Q}_{\omega_{\vec{k}}} \ldots \hat{Q}_{\omega^{(n)}_{\vec{k}(n)}} \middle| \mu \right\rangle_{\omega_s=\omega_L-\omega_{\mu\nu}}
\end{aligned} \tag{3.24}$$

Note that the transition of the many-body eigenstates $|i\rangle$ to $|f\rangle$ only occurs in the phononic subsystem: $|i\rangle \to |f\rangle = |g\mu\rangle \to |g\nu\rangle$. Therefore the matrix element can be split into two parts, an electronic one ($|g\rangle$) and a phononic one ($|\mu\rangle$, $|\nu\rangle$), which can be calculated separately.

Taking into account only one phononic branch $\omega(\vec{k})$ equation (3.24) can further be split into one-, two-, three-, four-phononic contributions, etc., all with

total momentum transfer $\Delta\vec{k} = 0$ as needed for light scattering in solids:

$$\begin{aligned}
\left[\epsilon^{\eta\xi}\right]^{(1)}_{\omega_s} &= \frac{\partial\epsilon^{\eta\xi}_{\omega_L}}{\partial Q_0}\langle\mu|\hat{Q}_0|\nu\rangle + \frac{1}{2}\frac{\partial^2\epsilon^{\eta\xi}_{\omega_L}}{\partial Q_0^2}\langle\mu|\hat{Q}_0^2|\nu\rangle + \frac{1}{6}\frac{\partial^3\epsilon^{\eta\xi}_{\omega_L}}{\partial Q_0^3}\langle\mu|\hat{Q}_0^3|\nu\rangle + \dots \\
\left[\epsilon^{\eta\xi}\right]^{(2)}_{\omega_s} &= \sum_{\vec{k}\neq 0}\left\{\frac{1}{2}\frac{\partial^2\epsilon^{\eta\xi}_{\omega_L}}{\partial Q_{\vec{k}}\partial Q_{-\vec{k}}}\langle\mu|\hat{Q}_{\vec{k}}\hat{Q}_{-\vec{k}}|\nu\rangle + \frac{1}{24}\frac{\partial^4\epsilon^{\eta\xi}_{\omega_L}}{\partial Q^2_{\vec{k}}\partial Q^2_{-\vec{k}}}\langle\mu|\hat{Q}^2_{\vec{k}}\hat{Q}^2_{-\vec{k}}|\nu\rangle + \dots\right\} \\
&\dots
\end{aligned} \tag{3.25}$$

As each of these processes contributes to the Raman intensity with different phase the complete Raman efficiency can be written as a thermal average of intensity contributions of all possible transitions:

$$S^{\eta\xi}_{\omega_s} = \frac{N_c V_E \omega_L \omega_s^3 \sum_\mu e^{-E_\mu/kT} \sum_\mu \sum_\nu \left|\left[\epsilon^{\eta\xi}_{\mu\to\nu}\right]^{(n)}_{\omega_s}\right|^2}{(4\pi)^2 c^4 \sum_\mu e^{-E_\mu/kT}}. \tag{3.26}$$

This expression describes the integrated line intensity of the observed Raman spectrum. A direct simulation of the experiment can be achieved by introducing a Lorentzian term $L^{(n)}$ which accounts for life-time broadening. This procedure leads to an expression for the spectral density:

$$\frac{\partial S^{\eta\xi}_{\omega_s=\omega_L-\omega}}{\partial\omega}(\omega) = \frac{N_c V_E (\omega_L-\omega)^3 \sum_\mu e^{-E_\mu/kT} \sum_\mu \sum_\nu \left|\left[\epsilon^{\eta\xi}_{\mu\to\nu}\right]^{(n)}_{\omega_s}\right|^2 L^{(n)}(\omega,\omega_{\mu\nu},\gamma)}{(4\pi)^2 c^4 \sum_\mu e^{-E_\mu/kT}}, \tag{3.27}$$

3.4 Calculation of Raman Spectra from Ab Initio Frozen-Phonon Calculations

In order to be able to use equation (3.27) to calculate the Raman spectra from ab initio results one has to consider that in equation (3.25) $\vec{Q}$ refers to a specific eigenvector $\vec{Q}_\zeta = (e_{1\zeta}, \dots, e_{m\zeta}, \dots, e_{N\zeta})$ of a phonon mode ζ with the frequency ω_ζ, which in general consists of $3N$ components, where N is the number of atoms per unit cell. Index $m = 1, \dots, N$ numerates the nuclei, and $e_{m\zeta}$ is the displacement of the m-th ion.

For computing the Raman intensities the following procedure is useful: As a first step one has to determine the eigenfrequencies and the eigenvectors of all phonon modes by diagonalizing the dynamical matrix D given in equation 2.13. As a next step, the nuclei are displaced according to a specific eigenvector $\vec{Q}_\zeta$, where the total energy and the dielectric function are calculated for various displacements. At this point the one-dimensional quantity u_ζ is introduced, which

is defined as the absolute value of the displacement vectors of the atoms in one elementary cell. It is linked to the phononic normal coordinate by

$$u_\zeta = \sqrt{\sum_m |u_\zeta^m|^2} = \frac{1}{Nf_\zeta} Q_\zeta, \tag{3.28}$$

where the factor f_ζ is

$$1/f_\zeta = \sum_m \frac{(e_\zeta^m)^2}{M_m}. \tag{3.29}$$

The total energy per unit cell and the components of the complex dielectric tensor can now be expanded into u_ζ. A fit of the *ab initio* results determines the coefficients a_n and b_n of the following expressions:

$$\frac{V_\zeta(u_\zeta)}{N} = a_0 + a_1 u_\zeta + a_2 u_\zeta^2 + a_3 u_\zeta^3 + a_4 u_\zeta^4 + \cdots \tag{3.30}$$

$$\epsilon_\zeta^{\eta\xi} = b_0 + b_1 u_\zeta + b_2 u_\zeta^2 + b_3 u_\zeta^3 + b_4 u_\zeta^4 + \cdots \tag{3.31}$$

Using relation (3.28) the phononic potential is obtained:

$$\frac{V_\zeta(Q_\zeta)}{N} = a_0 + \frac{a_1}{(Nf_\zeta)^{1/2}} Q_\zeta + \frac{a_2}{Nf_\zeta} Q_\zeta^2 + \frac{a_3}{(Nf_\zeta)^{3/2}} Q_\zeta^3 + \frac{a_4}{(Nf_\zeta)^2} Q_\zeta^4 + \cdots \tag{3.32}$$

It is important to notice that for large N (solid state limit) only the second order term contributes (independently from N) and all higher order terms vanish (a_0 can be set to zero and a_1 vanishes if the potential is expanded around its minimum). Therefore, in the solid state limit the phonon feels a harmonic potential. Anharmonic effects only occur due to phonon-phonon interaction.

In the same way the derivatives of the dielectric function of equation (3.25) can be expressed by the *ab initio* results (3.31). For the one-phonon contribution one obtains:

$$\left[\epsilon^{\eta\xi}\right]_{\omega_s}^{(1)^2} = \left\{ \frac{b_1}{\sqrt{Nf_{\omega_0}}} \langle \nu | \hat{Q} | \mu \rangle + \frac{b_2}{Nf_{\omega_0}} \langle \nu | \hat{Q}^2 | \mu \rangle + \cdots \right\}^2 \tag{3.33}$$

For very large N only the first term in the brackets which describes the one-phonon process contributes to the scattering efficiency in equation (3.26).

Chapter 4

Density Functional Theory and the LAPW Formalism

This chapter contains a brief description of the basic ideas and formulas of density functional theory and describes the concepts of the LAPW formalism.

4.1 Density Functional Theory

The fundament of **d**ensity **f**unctional **t**heory (DFT) is the Hohenberg-Kohn theorem [35]. It states that the ground state energy E of a non-spin-polarized system of interacting electrons in an external potential is given exactly as a functional of the electronic ground state density ρ

$$E = E[\rho]. \tag{4.1}$$

It was also shown that the true ground state density is the density which minimizes $E[\rho]$, and that all ground state properties are also functionals of the ground state density. However, the Hohenberg-Kohn theorem does not give a recipe how to form $E[\rho]$ and therefore some approximations have to be made. For this purpose the unknown functional of $E[\rho]$ is split into several parts:

$$E[\rho] = T_s[\rho] + E_{ei}[\rho] + E_{ii}[\rho] + E_H[\rho] + E_{xc}[\rho], \tag{4.2}$$

where $T_s[\rho]$ describes the kinetic energy of the non-interacting system, $E_{ei}[\rho]$ gives the Coulomb interaction energy between the electrons and the nuclei, E_{ii} comes from the interaction of the nuclei with each other, and $E_H[\rho]$ is the Hartree component of the electron-electron energy given as:

$$E_H[\rho] = \frac{e^2}{2} \int d^3\vec{r} d^3\vec{r}' \frac{\rho(\vec{r})\rho(\vec{r}')}{|\vec{r} - \vec{r}'|} \tag{4.3}$$

$E_{xc}[\rho]$ is an unknown functional, called the exchange-correlation (xc) functional, and it is assumed to be smaller than the other parts of $E[\rho]$.

In the so called **l**ocal **d**ensity **a**pproximation LDA, $E_{xc}[\rho]$ has the following form:

$$E_{xc}[\rho] = \int d^3\vec{r}\rho(\vec{r})\epsilon_{xc}(\rho(\vec{r})) \tag{4.4}$$

ϵ_{xc} is approximated here by a local function of the density, which is the known energy of the uniform electron gas.

LDA is one way to treat the problem with the exchange-correlation part in the energy functional $E[\rho]$. Many efforts have been made to improve the LDA functional like the **g**eneralized **g**radient **a**pproximation (GGA) [36–38] and the **w**eighted **d**ensity **a**pproximation (WDA) [39–41]. In GGA $\epsilon_{xc}(\rho)$ is replaced by a functional which is also local, but not only a function of the density but also of its gradient $\epsilon_{xc}(\rho, |\nabla\rho|)$. In the WDA method true non-local information is brought in via Coulomb integrals of the density with model exchange-correlation holes. Generally it can be said that it depends on the structure and on the elements of a considered crystal which approximation is the best compared to experimental results. In this work all calculations have been carried out within LDA.

Using a variational scheme, Kohn and Sham [42] showed that the correct density is given by the self-consistent solution of a set of single particle Schrödinger-like equations, known as the Kohn-Sham (KS) equations, with a density dependent potential

$$[T + V_{ei}(\vec{r}) + V_H(\vec{r}) + V_{xc}(\vec{r})]\varphi_i(\vec{r}) = \epsilon_i\varphi_i(\vec{r}). \tag{4.5}$$

The total density is given then by a sum over the single particle densities of the occupied orbitals:

$$\rho(\vec{r}) = \sum_i \varphi_i^*(\vec{r})\varphi_i(\vec{r}) \tag{4.6}$$

Here φ_i are the single particle orbitals (KS orbitals), ϵ_i are the corresponding eigenvalues, T is the kinetic energy operator, V_{ei} is the Coulomb potential due to the nuclei, V_H is the Hartree potential and V_{xc} is the exchange-correlation potential. V_H and V_{xc} are ρ dependent:

$$V_H(\vec{r}) = e^2 \int d^3\vec{r}' \frac{\rho(\vec{r}')}{|\vec{r} - \vec{r}'|} \tag{4.7}$$

and

$$V_{xc}(\vec{r}) = \frac{\delta E_{xc}[\rho]}{\delta\rho(\vec{r})}. \tag{4.8}$$

So the problem of solving a many-body Schrödinger equation has been transformed to a self-consistent solution of equations (4.5) and (4.6) in such a way,

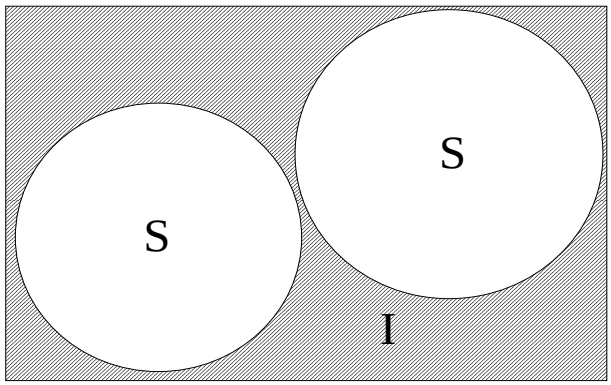

Figure 4.1: Fragmentation of the unit cell in the LAPW formalism

that a density must be found which yields an effective potential that, when inserted into the Schrödinger-like equations, yields orbitals which reproduce this density.

The DFT based electronic structure methods are classified according to the representations chosen for the KS orbitals, the density, and the potential. Among the most often used methods is the LAPW-method, which was used in all calculations done for this work. The basis set expansion of the KS orbitals has the form

$$\varphi_i(\vec{r}) = \sum c_{i\alpha}\phi_\alpha(\vec{r}), \tag{4.9}$$

where $\phi_\alpha(\vec{r})$ are the basis functions, and $c_{i\alpha}$ are the expansion coefficients, which are the only variables in the system. So the problem is to determine the $c_{i\alpha}$ for the occupied orbitals in such a way that they minimize the total energy.

In order to make the total energy functional more handy it is common to eliminate the unknown functional $T_s[\rho]$ of equation (4.2) by the single particle eigenvalues

$$E[\rho] = E_{ii}[\rho] + \sum_{\text{occ}} \epsilon_i + E_{xc}[\rho] - \int d^3\rho(\vec{r})(V_{xc}(\vec{r}) + \frac{1}{2}V_H(\vec{r})), \tag{4.10}$$

where the sum is taken over all occupied orbitals and ρ, V_H and V_{xc} are given by (4.6), (4.7), and (4.8).

4.2 The LAPW-Method

The LAPW method makes use of a basis set which is especially adapted to the problem of solving the Kohn-Sham equations in the case of a crystal. For that

purpose the unit cell is divided into non-overlapping atomic spheres S, which are centered at the atomic sites and an interstitial region I, like it is shown in Figure 4.1. In these two types of regions different basis sets are used.

1. In the interstitial region a plane wave basis is used for the KS orbitals

$$\phi_{\vec{k}_n+\vec{k}}(\vec{r}) = \frac{1}{\Omega^{1/2}} e^{i(\vec{k}_n+\vec{k})\cdot\vec{r}}, \tag{4.11}$$

where $\vec{k}$ is a wave vector inside the first Brillouin zone and $\vec{k}_n$ a reciprocal lattice vector.

2. Inside the spheres the basis functions are linear combinations of radial functions $u(r, E_l)$, $\dot{u}(r, E_l)$ times spherical harmonics $Y_{lm}(\hat{r})$:

$$\phi_{\vec{k}_n+\vec{k}}(\vec{r}) = \sum_{lm} [A_{lm} u_l(r, E_l) + B_{lm} \dot{u}_l(r, E_l)] Y_{lm}(\hat{r}) \tag{4.12}$$

The functions u_l are defined as regular solutions of the radial Schrödinger equation

$$\left\{ -\frac{d^2}{dr^2} + \frac{l(l+1)}{r^2} + V(r) - E_l \right\} r u_l(r) = 0 \tag{4.13}$$

for an energy E_l chosen usually at the center of the corresponding band with l-like character. $\dot{u}(r, E_l)$ is the energy derivative of u_l taken at the same energy E_l. A linear combination of these two functions constitute the linearization of the radial functions. The coefficients A_{lm} and B_{lm} are functions of k_n, determined by requiring that this basis function matches a plane wave with wavevector k_n at the sphere boundary in value and slope.

The solutions to the Kohn-Sham equations are expanded into this combined basis set of LAPW's

$$\varphi_{\vec{k}}(\vec{r}) = \sum_n c_n \phi_{\vec{k}_n} \tag{4.14}$$

and the coefficients c_n are determined by the Rayleigh-Ritz variational principle. Note that each plane wave is augmented by an atomic-like function in every atomic sphere, therefore the number of plane waves determines the size of the linear eigenvalue problem.

In order to improve upon the linearization and to make a consistent treatment of semicore and valence states in one energy window (to ensure orthogonality) possible, additional ($\vec{k}$ independent) basis functions can be added. They are called "local orbitals" [43] and consist of a linear combination of two radial functions at two different energies and one energy derivative taken at one of these energies:

$$\phi^{LO}_{lm} = [A_{lm} u_l(r, E_{1,l}) + B_{lm} \dot{u}_l(r, E_{1,l}) + C_{lm} u_l(r, E_{2,l})] Y_{lm}(\hat{r}) \tag{4.15}$$

The coefficients A_{lm}, B_{lm} and C_{lm} are determined by the requirements that ϕ^{LO} should be normalized and should have zero value and slope at the sphere boundaries.

Within the LAPW method the potential (and the electron density) is expanded in the following form:

$$V(\vec{r}) = \begin{cases} \sum_{lm} V_{lm}(r) Y_{lm}(\hat{r}) & \text{inside sphere} \\ \sum_{\vec{K}} V_{\vec{K}} e^{i\vec{K}\vec{r}} & \text{outside sphere} \end{cases} \tag{4.16}$$

Since no shape approximation for the potential is made, the procedure is called the "full-potential LAPW method" (FLAPW). The WIEN97 program package [44] was used in all calculations done for this thesis.

Chapter 5

The Dielectric Function

5.1 Macroscopic Description

Generally the interaction between a medium and an electromagnetic wave can be characterized via the Maxwell equations. In Maxwell's material equations, the electric displacement $\vec{D}$ and the induced current density $\vec{j}$ are connected to the electric field $\vec{E}$ and the magnetic induction $\vec{B}$ is linked to the magnetic field $\vec{H}$. In the case of a non-magnetic medium the magnetic permeability μ is equal to 1 and so $\vec{B} = \vec{H}$. In order to describe the relation between $\vec{D}$ and $\vec{E}$ the electric displacement is considered as a response to the applied electric field $\vec{E}$. Hence for $\vec{D}$ the following ansatz can be made:

$$D^{\eta} = \sum_{\xi} \epsilon^{\eta\xi} E^{\xi} + \sum_{\xi\gamma} \epsilon^{\eta\xi\gamma} E^{\xi} E^{\gamma} + \dots \tag{5.1}$$

This equation represents a Taylor expansion of the electric displacement $\vec{D}$ with respect to the electric field $\vec{E}$. A truncation after the first term leads to linear optical properties, with the linear term $\epsilon^{\eta\xi}$ being the dielectric tensor.

An induced current density $\vec{j}$ in a medium may be displayed by a linear ansatz again:

$$j^{\eta} = \sum_{\xi} \sigma^{\eta\xi} E^{\xi} + \dots, \tag{5.2}$$

where $\sigma^{\eta\xi}$ is the optical conductivity. Both quantities can be summarized in the complex dielectric tensor ϵ:

$$\epsilon^{\eta\xi}(\omega) = \epsilon_1^{\eta\xi}(\omega) + i\frac{4\pi}{\omega}\epsilon_2^{\eta\xi}(\omega) \tag{5.3}$$

The real and imaginary part in this equation are interrelated via the Kramers-Kronig relations.

5.2 Calculation of the Dielectric Function from First Principles.

In case of a metal, there are two contributions to the dielectric function. There is the *inter*band contribution, which takes into account the transitions from valence bands to conduction bands, and the *intra*band contribution, which accounts for free electron transitions in a partly filled conduction band. The intraband contribution to the dielectric function was not taken into account in all calculations done for this work, because of the fact, that it only occurs in an energy range with is not considered in Raman scattering.[1]

The dielectric function itself is calculated in the random-phase approximation described in Reference [45]. It should also be noticed here that it is calculated within the independent-particle picture where the Coulomb interactions between initial and final state are not considered. If local field effects are neglected and only linear terms are considered, the microscopic dielectric tensor can be calculated from solutions of the unperturbed system. Finally the interband contributions to the imaginary part of the macroscopic dielectric tensor in the dipole approximation is given by the following expression:

$$\begin{aligned} \mathrm{Im}\epsilon^{\eta,\xi}(\omega) &= \frac{4\pi^2 e^2}{m_e^2 \omega^2 V_E} \sum_{i,j,\vec{k}} \langle i\vec{k}|\hat{p}^{\eta}|j\vec{k}\rangle\langle j\vec{k}|\hat{p}^{\xi}|i\vec{k}\rangle \\ &\times \delta(E_{j\vec{k}} - E_{i\vec{k}} - \hbar\omega) \times f_{i,\vec{k}}(1 - f_{j,\vec{k}}) \end{aligned} \tag{5.4}$$

Here $|i\vec{k}\rangle$ and $|j\vec{k}\rangle$ are the one-electron Kohn-Sham orbitals with wavevector $\vec{k}$. $E_{i\vec{k}}$ and $E_{j\vec{k}}$ are the corresponding band energies which are involved in a transition, and $\hat{p}^{\eta}$ ($\hat{p}^{\xi}$) is the η (ξ)-th component of the momentum operator. e denotes the electron charge. More details about the calculation of $\mathrm{Im}\epsilon^{\eta\xi}(\omega)$ in the WIEN97 program package can be found in Reference [46].

[1] The photon energy is typically between 1.5 and 3 eV.

Chapter 6

Crystal Structure and Symmetry

With the help of group theory, as shown in the previous sections, one obtains the number of eigenvibrations and the symmetry coordinates classified according to their irreducible representations. In the framework of this thesis, the force constants are calculated in the following way: Atoms which take part in an eigenvibration are displaced seperately from their equilibrium positions. For each of these configurations the forces acting on the atoms are calculated within the LAPW method. From these data the force constants are obtained with the help of a fitting procedure and the dynamical matrix is determined. The diagonalization of the dynamical matrix yields then the eigenfrequencies and eigenvectors.

6.1 $YBa_2Cu_3O_7$

6.1.1 Structural Data

In Figure 6.1 the unit cell of $YBa_2Cu_3O_7$ is shown. $YBa_2Cu_3O_7$ crystallizes in the orthorhombic space group Pmmm with D^1_{2h} symmetry (Schönflies notation), and the corresponding point group is D_{2h}. There are 13 atoms in the unit cell, where 8 of them are non-equivalent. These are Y, Ba, two copper atoms Cu1 and Cu2, and 4 different types of oxygen. The lattice parameters and atomic positions given in Table 6.1 are obtained by fully optimizing the crystal structure, i.e. searching for the total energy minimum with respect to lattice parameters and ion displacements [20]. The motions of Ba, Cu2, O2, O3, and O4 in z direction do not offend the crystal's symmetry and thus give rise to the five total symmetric A_{1g} modes which will be seen below. fully-optimized unit cell of

6.1.2 Factor Group Analysis

In this section it is shown for the $q = 0$ modes of $YBa_2Cu_3O_7$, how the number of eigenvibrations for each irreducible representation and the corresponding symmetry coordinates can be obtain with the help of the previously discussed

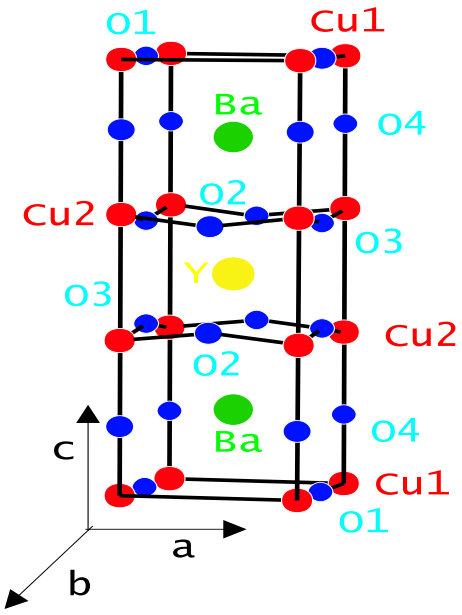

Figure 6.1: Unit cell of $YBa_2Cu_3O_7$

factor group analysis (see Section 2.4.2). The 13 atoms of the unit cell lead to a 39 dimensional reducible matrix representation for each symmetry operation. Each matrix represenation transforms the x_i-coordinate of atom j into the x_i'-coordinate of atom j', where the atoms j and j' have to be the same or equivalent, respectively. It should be noticed that in these representations diagonal elements occur only if the symmetry operation leaves the position of an atom unchanged or one of the coordinates changes sign. Since the character of the representation is given by the trace of the representation matrix only those atomic coordinates x_i contribute which transform to $\pm x_i$ when applying a symmetry operation. Therefore the characters of a reducible representation can be easily determined by considering these coordinates only (see Table 6.2).
The next step is now to determine how many of the various irreducible representations are contained in the reducible representations. This can be done with the help of equation (2.55) and will explicitly be shown for the case of the irreducible represenation B_{1u}:

$$\begin{aligned} n_{B_{1u}} &= \frac{1}{8}\{[1]*(39)+[1]*(-13)+[-1]*(-3)+[-1]*(-3) \\ &+ [-1]*(-9)+[-1]*(3)+[1]*(13)+[1]*(13)\} = 8 \end{aligned} \tag{6.1}$$

	Y	Ba	Cu1	Cu2	O1	O2	O3	O4
x $[a]$	$\frac{1}{2}$	$\frac{1}{2}$	0	0	0	$\frac{1}{2}$	0	0
y $[b]$	$\frac{1}{2}$	$\frac{1}{2}$	0	0	$\frac{1}{2}$	0	$\frac{1}{2}$	0
z $[c]$	$\frac{1}{2}$	0.1814	0	0.6493	0	0.3774	0.3765	0.1620

a	=	7.104 a.u.
b	=	7.214 a.u.
c	=	21.476 a.u.

Table 6.1: Internal coordinates in units of c and the lattice parameters of the fully-optimized unit cell of $YBa_2Cu_3O_7$.

	E	C_2^z	C_2^y	C_2^x	I	σ^{xy}	σ^{xz}	σ^{yz}
invariant atoms	13	13	3	3	3	3	13	13
$\chi^{red}(R)$	39	-13	-3	-3	-9	3	13	13

Table 6.2: Characters χ^{red} of the reducible representation of $YBa_2Cu_3O_7$.

Here the numbers in the [] brackets are the characters of the irreducible representations taken from Table 6.3[1] and the other factors are the characters of the reducible representation taken from Table 6.2. The results of all irreducible representations are given in Table 6.4.

By investigating the transformation properties of the components of the dipole moment vector and the polarizability tensor it is also possible to determine their reducible characters. This can be done in the same way as it has been done in the case of the atomic coordinates. The results are given in Table 6.5 and with the help of equations (2.62) also the Raman and infrared selection rules can be derived, which are listed in Table 6.6.

Symmetry Coordinates:
The symmetry coordinates Q_n should give evidence for the symmetry properties of a crystal and its possible vibrational species. These symmetry coordinates can be written as linear combinations of the Cartesian coordinates

$$Q_n = \sum_{s=1}^{r} [a_n(s)x(s) + b_n(s)y(s) + c_n(s)z(s)], \qquad n = 1, \ldots, 3r \tag{6.2}$$

where the coefficients can be determined by the condition that the symmetry operations of the point group have to transform the coordinates according to the characters of a concerned symmetry type.

[1] The character tables of the irreducible representations of all point groups, called character tables, can be found in [29].

D_{2h}	E	C_2^z	C_2^y	C_2^x	I	σ^{xy}	σ^{xz}	σ^{yz}
A_{1g}	1	1	1	1	1	1	1	1
A_{1u}	1	1	1	1	-1	-1	-1	-1
B_{1g}	1	1	-1	-1	1	1	-1	-1
B_{1u}	1	1	-1	-1	-1	-1	1	1
B_{2g}	1	-1	1	-1	1	-1	1	-1
B_{2u}	1	-1	1	-1	-1	1	-1	1
B_{3g}	1	-1	-1	1	1	-1	-1	1
B_{3u}	1	-1	-1	1	-1	1	1	-1

Table 6.3: Characters χ^{irred} of the point group D_{2h}.

	A_{1g}	A_{1u}	B_{1g}	B_{1u}	B_{2g}	B_{2u}	B_{3g}	B_{3u}
n_{irred}	5	0	0	8	5	8	5	8

Table 6.4: Modes per irreducible representation in case of $YBa_2Cu_3O_7$.

	E	C_2^z	C_2^y	C_2^x	I	σ^{xy}	σ^{xz}	σ^{yz}
χ^d	3	-1	-1	-1	-3	1	1	1
χ^{d_x}	1	-1	-1	1	-1	1	1	-1
χ^{d_y}	1	-1	1	-1	-1	1	-1	1
χ^{d_z}	1	1	-1	-1	-1	-1	1	1
χ^{α}	6	2	2	2	6	2	2	2
$\chi^{\alpha_{\rho\rho}}(\rho = x, y, z)$	1	1	1	1	1	1	1	1
$\chi^{\alpha_{xy}}$	1	1	-1	-1	1	1	-1	-1
$\chi^{\alpha_{xz}}$	1	-1	1	-1	1	-1	1	-1
$\chi^{\alpha_{yz}}$	1	-1	-1	1	1	-1	-1	1

Table 6.5: Characters of the dipole moment χ^d and the polarizability χ^{α} as well as their components.

	A_{1g}	A_{1u}	B_{1g}	B_{1u}	B_{2g}	B_{2u}	B_{3g}	B_{3u}
Raman active	x		x		x		x	
Infrared active				x		x		x
Polarization	$\alpha_{xx}, \alpha_{yy}, \alpha_{zz}$		α_{xy}	d_z	α_{xz}	d_y	α_{yz}	d_x

Table 6.6: The Raman and infrared selection rules of the point group D_{2h}.

In the case of $YBa_2Cu_3O_7$ ($r = 13$) $s = Y$, Ba, $\boldsymbol{Ba}$, $Cu1$, $Cu2$, $\boldsymbol{Cu2}$, $O1$, $O2$, $\boldsymbol{O2}$, $O3$, $\boldsymbol{O3}$, $O4$, $\boldsymbol{O4}$, where the atoms written in bold letters refer to equivalent sites of one atomic species. The coefficients $a_n(s)$, $b_n(s)$ and $c_n(s)$ are obtained now in the following way:

- Type A_{1g}: $n_{irred} = 5$ ($n = 1, \ldots, 5$)

  Applying a symmetry operation (e.g C_2^z) to the symmetry coordinate

$$C_2^z Q_n = \sum_{s=1}^{13} [-a_n(s)x(s) - b_n(s)y(s) + c_n(s)z(s)] \stackrel{!}{=} \chi^{A_{1g}}(C^{z_2})Q_n = Q_n$$

  leads to

$$a_n(s) = b_n(s) = 0,$$
$$Q_n = \sum_{s=1}^{13} c_n(s)z(s).$$

  Furthermore, from

$$\begin{aligned} C_2^y Q_n \;=\; & -c_n(Y)z(Y) - c_n(Ba)z(\boldsymbol{Ba}) - c_n(\boldsymbol{Ba})z(Ba) \\ & -c_n(Cu1)z(Cu1) - c_n(Cu2)z(\boldsymbol{Cu2}) - c_n(\boldsymbol{Cu2})z(Cu2) \\ & -c_n(O1)z(O1) - c_n(O2)z(\boldsymbol{O2}) - c_n(\boldsymbol{O2})z(O2) \\ & -c_n(O3)z(\boldsymbol{O3}) - c_n(\boldsymbol{O3})z(O3) \\ & -c_n(O4)z(\boldsymbol{O4}) - c_n(\boldsymbol{O4})z(O4) \stackrel{!}{=} \chi^{A_{1g}}(C^{y_2})Q_n = Q_n \end{aligned}$$

  follows

$$\begin{aligned} c_n(Y) &= c_n(Cu1) = c_n(O1) = 0 \\ c_n(Ba) &= -c_n(\boldsymbol{Ba}) \\ c_n(Cu2) &= -c_n(\boldsymbol{Cu2}) \\ c_n(O2) &= -c_n(\boldsymbol{O2}) \\ c_n(O3) &= -c_n(\boldsymbol{O3}) \\ c_n(O4) &= -c_n(\boldsymbol{O4}). \end{aligned}$$

  The equations for the transformations according to C_2^x, I, σ^{xy}, σ^{xz} and σ^{yz} may be neglected because of the fact that they do not give any new conditions for the coefficients. Thus

$$\begin{aligned} Q_1 &= z(Ba) - z(\boldsymbol{Ba}) \\ Q_2 &= z(Cu2) - z(\boldsymbol{Cu2}) \\ Q_3 &= z(O2) - z(\boldsymbol{O2}) \\ Q_4 &= z(O3) - z(\boldsymbol{O3}) \\ Q_5 &= z(O4) - z(\boldsymbol{O4}). \end{aligned}$$

- Type B_{1u}: $n_{irred} = 8$ $(n = 6, \ldots, 13)$
  Similarly to the A_{1g} representation one obtains

$$\begin{array}{lcl}
Q_6 & = & z(Y) \\
Q_7 & = & z(Cu1) \\
Q_8 & = & z(O1) \\
Q_9 & = & z(Ba) + z(\boldsymbol{Ba}) \\
Q_{10} & = & z(Cu2) + z(\boldsymbol{Cu2}) \\
Q_{11} & = & z(O2) + z(\boldsymbol{O2}) \\
Q_{12} & = & z(O3) + z(\boldsymbol{O3}) \\
Q_{13} & = & z(O4) + z(\boldsymbol{O4}).
\end{array}$$

- Type B_{2g}: $n_{irred} = 5$ $(n = 14, \ldots, 18)$

$$\begin{array}{lcl}
Q_{14} & = & x(Ba) - x(\boldsymbol{Ba}) \\
Q_{15} & = & x(Cu2) - x(\boldsymbol{Cu2}) \\
Q_{16} & = & x(O2) - x(\boldsymbol{O2}) \\
Q_{17} & = & x(O3) - x(\boldsymbol{O3}) \\
Q_{18} & = & x(O4) - x(\boldsymbol{O4}).
\end{array}$$

- Type B_{2u}: $n_{irred} = 8$ $(n = 18, \ldots, 26)$

$$\begin{array}{lcl}
Q_{19} & = & y(Y) \\
Q_{20} & = & y(Cu1) \\
Q_{21} & = & y(O1) \\
Q_{22} & = & y(Ba) + y(\boldsymbol{Ba}) \\
Q_{23} & = & y(Cu2) + y(\boldsymbol{Cu2}) \\
Q_{24} & = & y(O2) + y(\boldsymbol{O2}) \\
Q_{25} & = & y(O3) + y(\boldsymbol{O3}) \\
Q_{26} & = & y(O4) + y(\boldsymbol{O4}).
\end{array}$$

- Type B_{3g}: $n_{irred} = 5$ $(n = 27, \ldots, 31)$

$$\begin{array}{lcl}
Q_{27} & = & y(Ba) - y(\boldsymbol{Ba}) \\
Q_{28} & = & y(Cu2) - y(\boldsymbol{Cu2}) \\
Q_{29} & = & y(O2) - y(\boldsymbol{O2}) \\
Q_{30} & = & y(O3) - y(\boldsymbol{O3}) \\
Q_{31} & = & y(O4) - y(\boldsymbol{O4}).
\end{array}$$

- Type B_{3u}: $n_{ired} = 8$ $(n = 32, \ldots, 39)$

$$\begin{aligned}
Q_{32} &= x(Y) \\
Q_{33} &= x(Cu1) \\
Q_{34} &= x(O1) \\
Q_{35} &= x(Ba) + x(\boldsymbol{Ba}) \\
Q_{36} &= x(Cu2) + x(\boldsymbol{Cu2}) \\
Q_{37} &= x(O2) + x(\boldsymbol{O2}) \\
Q_{38} &= x(O3) + x(\boldsymbol{O3}) \\
Q_{39} &= x(O4) + x(\boldsymbol{O4}).
\end{aligned}$$

All the Q_n are orthogonal to each other. They are, however, not necessarily normal coordinates, since more than one eigenvibrations belong to each symmetry type. Therefore the eigenvectors, which are linear combinations of the symmetry coordinates of the same symmetry, can only be determined by a lattice dynamical calculation. The three acoustic phonon modes, which are pure translational oscillations, can be assigned as B_{1u}, B_{2u} and B_{3u} vibrations. Thus one ends up with 36 optical modes:

$$\Gamma = 5A_{1g} + 5B_{2g} + 5B_{3g} + 7B_{1u} + 7B_{2u} + 7B_{3u} \tag{6.3}$$

6.1.3 Comparison between $YBa_2Cu_3O_7$ and $YBa_2Cu_3O_6$

In the $YBa_2Cu_3O_{7-\delta}$ system, T_c may be varied via oxygen doping. The critical temperature which is 93 K at optimal doping ($\delta \approx 0.05$) is systematically reduced when oxygen is lost from the CuO chains. For $\delta \approx 0.5$ superconductivity disappears and the system undergoes a transformation to an antiferromagnetic insulator. $YBa_2Cu_3O_6$ has a tetragonal structure with point group D_{4h} with D_{2h}, the point group of $YBa_2Cu_3O_7$, being a subgroup of D_{4h}. In this work, only the phonon modes of $YBa_2Cu_3O_7$ will be presented. However, since $YBa_2Cu_3O_7$ is close to the tetragonal structure of $YBa_2Cu_3O_6$ in many papers the analysis of the $YBa_2Cu_3O_7$ modes is carried out in terms of the tetragonal symmetry. Therefore a comparison of the two point groups is given here.

Table 6.7 gives an overview over the eigenvibrations in $YBa_2Cu_3O_6$ and their optical activity, while Figure 6.2 shows the evolution of the vibrational species if the symmetry is reduced from D_{4h} to D_{2h}. Because of the fact that the orthorhombic deformation in $YBa_2Cu_3O_7$ is not that large, the eigenvectors of the compatible vibrations of both structures should be similar. There has been substantial interest in the vibrations of the O2 and O3 atoms in z direction. In the case of D_{2h} symmetry, there are two vibrations dominated by these two atoms, both having A_{1g} symmetry. Since O2 and O3 are not equivalent their displacements are different but similar in magnitude. One of the modes exhibits in-phase vibrations of O2 and O3, where in the other mode they are oscillating

D_{4h}	n_{irred}	involved atoms	selection rules
A_{1g}	4	Ba, $Cu2$, $O2$, $O3$, $O4$ $\boldsymbol{Ba}$, $\boldsymbol{Cu2}$, $\boldsymbol{O2}$, $\boldsymbol{O3}$, $\boldsymbol{O4}$	$\alpha_{xx}, \alpha_{yy}, \alpha_{zz}$
B_{1g}	1	$O2$, $O3$ $\boldsymbol{O2}$, $\boldsymbol{O3}$	$\alpha_{xx} = -\alpha_{yy}$
A_{2u}	6	Y, Ba, $Cu1$, $Cu2$, $O1$, $O2$, $O3$, $O4$ $\boldsymbol{Y}$, $\boldsymbol{Ba}$, $\boldsymbol{Cu1}$, $\boldsymbol{Cu2}$, $\boldsymbol{O1}$, $\boldsymbol{O2}$, $\boldsymbol{O3}$, $\boldsymbol{O4}$	d_z
B_{2u}	1	$O2$, $O3$ $\boldsymbol{O2}$,$\boldsymbol{O3}$	forbidden
E_g	5	Ba, $Cu2$, $O2$, $O3$, $O4$ $\boldsymbol{Ba}$, $\boldsymbol{Cu2}$, $\boldsymbol{O2}$, $\boldsymbol{O3}$, $\boldsymbol{O4}$	$\alpha_{xz} = \alpha_{yz}$
E_u	7	Y, Ba, $Cu1$, $Cu2$, $O1$, $O2$, $O3$, $O4$ $\boldsymbol{Y}$, $\boldsymbol{Ba}$, $\boldsymbol{Cu1}$, $\boldsymbol{Cu2}$, $\boldsymbol{O1}$, $\boldsymbol{O2}$, $\boldsymbol{O3}$, $\boldsymbol{O4}$	$d_x = d_y$

Table 6.7: The number of the eigenvibrations with all atoms involved as well as the optical selection rules for all vibrational species of $YBa_2Cu_3O_6$.

out-of-phase. In case of D_{4h} symmetry, O2 and O3 are equivalent and thus their amplitudes are the same in case of the total symmetric in-phase vibration. The out-of-phase motion reduces the symmetry to D_{2h}, therefore this mode is a B_{1g} vibration in $YBa_2Cu_3O_6$. Analogously, the B_{1u} modes are split into A_{2u} and B_{2u} vibrations when going from $YBa_2Cu_3O_7$ to $YBa_2Cu_3O_6$. In case of an intermediate oxygen content $YBa_2Cu_3O_{7-\delta}$ the defect structure is either orthorhombic ($\delta < 0.5$) or tetragonal ($\delta > 0.5$), thus certain selection rules may be lost and forbidden vibrations may become active.

6.2 $HgBa_2Ca_{n-1}Cu_nO_{2n+2}$ (n =1,2,3,4)

6.2.1 Structural Data

The record critical temperature of $HgBa_2Ca_2Cu_3O_{8+\delta}$ [7, 8], 136 K at ambient pressure, which can be further increased to over 160 K by applying high pressure [8, 47, 48], has led to an increase of interest in the physical properties of the homologous Hg based series $HgBa_2Ca_{n-1}Cu_nO_{2n+2+\delta}$. All members of the Hg-family crystallize in a tetragonal lattice with space group P4/mmm, where the c axis is perpendicular to the CuO_2 planes. A short notation for the different representatives is given according to the number of CuO_2 layers as Hg-12(n-1)n. Hereby 1 stands for the one Hg atom, and 2 for the two Ba atoms in each cell, while the n-1 Ca atoms, and the n CuO_2 planes further determine this nomenclature. Pictures of the unit cells of Hg-1201, Hg-1212, Hg-1223, and Hg-1234 are shown in Figure 6.3 and the corresponding structural data are given in

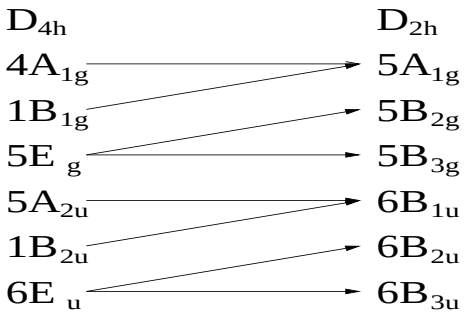

Figure 6.2: Comparison between the eigenvibrations of the space-groups D_{4h} and D_{2h}.

Table 6.9.

It is a common feature of the $HgBa_2Ca_{n-1}Cu_nO_{2n+2+\delta}$ superconductors that their T_c can be varied via doping. In that case additional charge is introduced into the crystal by an excess oxygen OI located at (1/2,1/2,0) in the Hg plane as shown in Figure 6.3. In the Hg-1201 crystal the doping parameter δ varies between δ=0.04 and δ=0.23 [49]. Furthermore it is claimed that there is a second doping site at (0, 1/2, z), but this is not taken into account in our calculations, because it can only be occupied if two Hg atoms are replaced by two Cu atoms in the nearest neighbourhood [50]. The doping parameter δ is one if all OI positions are occupied and zero if all OI positions are empty.

6.2.2 Factor Group Analysis

In case of the Hg-family, the factor-group analysis has to be carried out analogously to the sections 6.1.2 and 6.1.3, but will not be shown in detail here. Only the most important results will be presented. These are the number of Raman active eigenvibrations and the atoms participating in these irreducible representations. These data are shown in Table 6.8 for n=1, 2, 3, 4.

In all Hg-based structures the A_{1g} vibrations involving Ba and O2 are very similar. These two atoms are displaced from their equillibrium positions in z-direction and perform coupled vibrations with their equivalent partners. Compared to the single layer Hg-1201, in case of $n = 2$, the CuO_2 plane is doubled with a layer of Ca atoms in between. As a consequence, the oxygen and copper atoms of the planes are no longer sitting on positions with the highest possible symmetry, and therefore can participate in the A_{1g} vibrations. In the $n = 3$ structure, there are two Ca layers and three CuO_2 planes, such that the Ca atoms are also involved in the A_{1g} modes, whereas the CuO_2 plane situated in the middle of the unit cell does not participate due to symmetry. And last but not least, if $n = 4$, again a CuO_2 layer and a Ca layer are added, resulting in even more A_{1g}

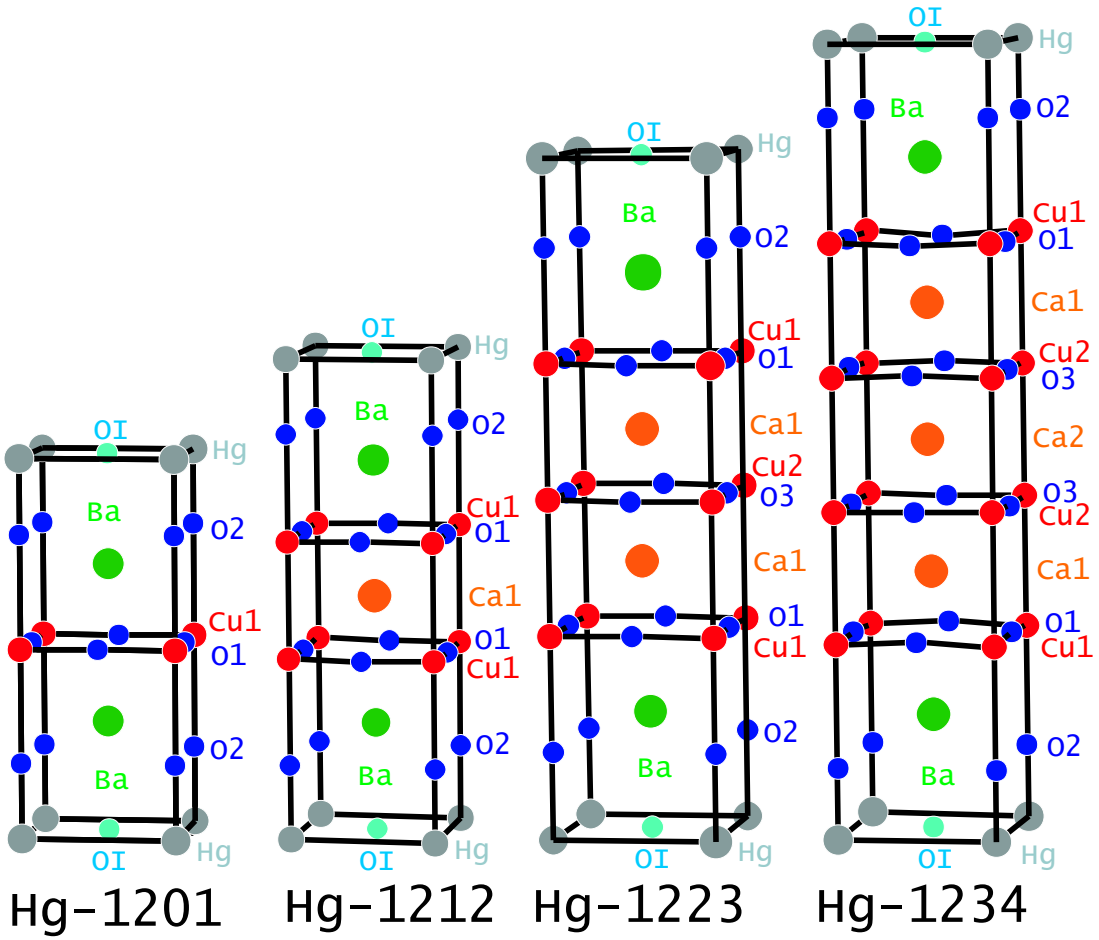

Figure 6.3: Crystal structures of the $HgBa_2Ca_{n-1}Cu_nO_{2n+2}$ family.

Atom	Hg-1201	Hg-1212	Hg-1223	Hg-1234
Hg				
Ba	$A_{1g} + E_g$	$A_{1g} + E_g$	$A_{1g} + E_g$	$A_{1g} + E_g$
Cu1		$A_{1g} + E_g$	$A_{1g} + E_g$	$A_{1g} + E_g$
Cu2				$A_{1g} + E_g$
O1		$A_{1g} + B_{1g} + 2E_g$	$A_{1g} + B_{1g} + 2E_g$	$A_{1g} + B_{1g} + 2E_g$
O2	$A_{1g} + E_g$	$A_{1g} + E_g$	$A_{1g} + E_g$	$A_{1g} + E_g$
O3				$A_{1g} + B_{1g} + 2E_g$
Ca1			$A_{1g} + E_g$	$A_{1g} + E_g$
Ca2				
total	$2A_{1g} + 2E_g$	$4A_{1g} + 1B_{1g} + 5E_g$	$5A_{1g} + 1B_{1g} + 6E_g$	$7A_{1g} + 2B_{1g} + 9E_g$

Table 6.8: The irreducible representations of all Raman active modes of $HgBa_2Ca_{n-1}Cu_nO_{2n+2}$ with the participating atoms.

atomic structure data [c]												
	Hg-1201			Hg-1212			Hg-1223			Hg-1234		
	x	y	z	x	y	z	x	y	z	x	y	z
Hg	0	0	0	0	0	0	0	0	0	0	0	0
Ba	$\frac{1}{2}$	$\frac{1}{2}$	$\pm z_{Ba}$	$\frac{1}{2}$	$\frac{1}{2}$	$\pm z_{Ba}$	$\frac{1}{2}$	$\frac{1}{2}$	$\pm z_{Ba}$	$\frac{1}{2}$	$\frac{1}{2}$	$\pm z_{Ba}$
Cu1	0	0	$\frac{1}{2}$	0	0	$\pm z_{Cu1}$	0	0	$\pm z_{Cu1}$	0	0	$\pm z_{Cu1}$
Cu2							0	0	$\frac{1}{2}$	0	0	$\pm z_{Cu2}$
O1	$\frac{1}{2}$	0	$\frac{1}{2}$	$\frac{1}{2}$	0	$\pm z_{O1}$	$\frac{1}{2}$	0	$\pm z_{O1}$	$\frac{1}{2}$	0	$\pm z_{O1}$
O1'	0	$\frac{1}{2}$	$\frac{1}{2}$	0	$\frac{1}{2}$	$\pm z_{O1}$	0	$\frac{1}{2}$	$\pm z_{O1}$	0	$\frac{1}{2}$	$\pm z_{O1}$
O2	0	0	$\pm z_{O2}$	0	0	$\pm z_{O2}$	0	0	$\pm z_{O2}$	0	0	$\pm z_{O2}$
O3							$\frac{1}{2}$	0	$\frac{1}{2}$	$\frac{1}{2}$	0	$\pm z_{O3}$
O3'							0	$\frac{1}{2}$	$\frac{1}{2}$	0	$\frac{1}{2}$	$\pm z_{O3}$
Ca1				$\frac{1}{2}$	$\frac{1}{2}$	$\frac{1}{2}$	$\frac{1}{2}$	$\frac{1}{2}$	$\pm z_{Ca1}$	$\frac{1}{2}$	$\frac{1}{2}$	$\pm z_{Ca1}$
Ca2										$\frac{1}{2}$	$\frac{1}{2}$	$\frac{1}{2}$

Table 6.9: Internal coordinates for the Hg-compounds.

vibrations of the CuO_2 planes. The irreducible representation of E_g symmetry is two-dimensional and the E_g modes are related to the atomic motions in the (a, b) plane. Since the structure is tetragonal the a - and b - axes are equivalent and therefore in case of Hg-1201, Hg-1212, Hg-1223, and Hg-1234 only 2, 5, 6, and 9 E_g frequencies, respectively, will be detected.

Chapter 7

Results for $YBa_2Cu_3O_7$

In this section all Raman-active phonon modes of $YBa_2Cu_3O_7$ are investigated by first-principles LAPW calculations. As already shown in section 6.1.2 these phonon modes can be devided into three different symmetry classes, namely A_{1g}, B_{2g}, and B_{3g}. Thereby each of these classes consists of five eigenmodes which are coupled vibrations of Ba, the plane copper atom Cu2, the plane oxygens O2 and O3 and the apical oxygen O4. The A_{1g} modes are characterized there by c-axis vibrations of these five atoms, while within the B_{2g} and B_{3g} modes these atoms move in a and b-direction, respectively.

After a short description of the computational details a summary about the calculated phonon frequencies and corresponding eigenvectors of the Raman-active phonon vibrations will be given. Technologically, it is possible to produce the $YBa_2Cu_3O_7$ crystals with a site-selective oxygen isotope substitution, i.e. where only the plane or the apical oxygen sites are occupied by another isotope [51–55]. Thereby the influence on T_c strongly depends on the type of the substitution. A recipe, how the frequencies and eigenvectors in case of a site-selective isotope substitution can be obtained from the results of an unsubstituted crystal , will be presented. With the help of this procedure, the changes in the frequencies and eigenvectors in the case of site-selective isotope substitutions will be studied and compared to experimental results. Then the computed Raman scattering intensities of the A_{1g}-modes will be presented and cross checked with measured spectra. Finally, also the influence of site-selective isotope substitutions on the scattering intensities will be shown and discussed in detail. The last section will deal with Y point phonons in this material.

7.1 Computational Details

All calculations have been carried out within the full-potential linearized augmented plane-wave (LAPW) method [56] using the program package WIEN97 [44]. Exchange and correlation effects have been treated in the local-density ap-

proximation (LDA). As indicated before the totally relaxed crystal structure has been the starting point in order to account for overbinding effects by LDA.

The basis set, which was used, included approximately 2000 basis functions supplemented by local orbitals for the treatment of the semicore states Y-4s, Y-4p, Ba-5s, Ba-5p, Ba-4d, Cu-3s, Cu-3p, and O-2s. For the A_{1g} modes the Brillouin zone integrations were carried out on a $\vec{k}$-point mesh consisting of 243 points in the irreducible wedge (IBZ) using a Gaussian smearing of 0.002 mRyd. For the B_{2g} and B_{3g} vibrations 144 $\vec{k}$-points in the IBZ turned out to give sufficient accuracy. In all cases, the $\vec{k}$-point mesh was further increased for computation of the dielectric tensor. The details of the optimization procedure can be found in Reference [20].

The force constants were established by least-square fits of atomic-force values calculated for 8 to 13 different distortion patterns for each class of modes (the actual number depending on the symmetry). After diagonalization the dynamical matrix the atoms were again displaced along the eigenvector. Thereby the accuracy of the fitting procedure was cross-checked,and more important, an accurate description of the dielectric tensor as a function of displacement according to the normal coordinate was guaranteed.

7.2 Results and Discussion

7.2.1 Phonon Frequencies and Eigenvectors

Table 7.1 shows the phonon frequencies and the corresponding eigenvectors of all the Raman-active modes obtained by solving equation (2.12). The A_{1g} data and the frequencies of the B_{2g} and B_{3g} modes have been published elsewhere [63, 64]. They are repeated for completeness and further comparison to the results of site-selective isotope substitutions. All phonon frequencies excellently reproduce their experimental counterparts, with a significant improvement achieved compared to the calculations carried out for the experimental structural parameters [65–67]. For the eigenvectors it can be generally said that the atomic displacements are less coupled. This was pointed out already in Reference [63] for the A_{1g} modes. In particular, it should be mentioned that the O4 contribution to the O2–O3 mode is much smaller in comparison to the results obtained with experimental lattice parameters, since this admixture is responsible for dramatic effects on the Raman scattering intensity as will be shown below. It should also be noted that the eigenvectors are in good agreement to those estimated from experimental Raman data [68]. For the B_{2g} and B_{3g} vibrations, the modes are clearly dominated by one atomic species. Note that O2 (O3) in the B_{2g} (B_{3g}) mode has a large vibrational frequency due to the stretching of a rigid Cu-O2 (Cu2-O3) bond in x (y) direction.

	mode	ω_{exp}	ω_{th}	Ba	Cu2	O2	O3	O4
	Ba	116-123	123	0.91	0.41	0.05	0.05	0.04
	Cu2	145-152	147	0.42	-0.90	-0.08	-0.06	0.00
A_{1g} ($\parallel c$)	O2–O3	335-338	338	0.00	0.03	-0.77	0.63	-0.01
	O2+O3	435-442	422	0.03	0.11	-0.60	-0.73	-0.31
	O4	493-500	487	0.02	-0.02	0.19	0.24	-0.95
	Ba	69-79	65	0.90	0.29	0.14	0.08	0.29
	Cu2	140-142	142	-0.35	0.82	0.38	0.24	0.00
B_{2g} ($\parallel a$)	O4	209-210	222	-0.27	-0.09	-0.03	-0.04	0.96
	O3	370	389	0.00	-0.30	0.06	0.95	0.02
	O2	579-585	593	0.00	0.37	-0.91	0.18	0.02
	Ba	78-83	79	0.91	0.32	0.10	0.15	0.18
	Cu2	140-141	141	-0.36	0.81	0.25	0.37	-0.03
B_{3g} ($\parallel b$)	O4	303-307	293	-0.17	-0.04	-0.03	0.01	0.98
	O2	378	372	0.00	0.34	-0.93	-0.11	-0.01
	O3	526	546	0.00	-0.34	-0.23	0.90	-0.03

Table 7.1: Phonon frequencies (in cm^{-1}) and eigenvectors for the A_{1g}, B_{2g}, and B_{3g} modes at $q = 0$ in comparison to experimental data (References [33, 57–62]).

7.2.2 Raman Intensities

The calculated spectral densities are shown in Figure 7.1 for diagonal scattering geometries at room temperature. For the Lorentzian lineshapes an overall line broadening of $\Gamma = 35$ K has been chosen. Theory quantitatively reproduces the experimentally measured intensities presented in Figure 7.2. For comparison, in Figure 7.1 the calculated intensities of the Ba and Cu modes are displayed (grey lines) when a smaller broadening of $\Gamma = 18$ is used for the two low-energy modes. With this choice, for the (zz)-polarization not only the integrated intensities but also the spectral densities excellently agree with their experimental counterparts. The intensities of the in-plane polarizations are more than one order of magnitude smaller than those in (zz)-geometry as already found by Heyen *et al.* [69] in resonant Raman scattering.

The resonant behavior of the total efficiency $S_{zz}(\omega)$ (this is the integrated spectral density) is presented in Figure 7.3. Since Raman scattering experiments exhibit the phonon frequencies but at the same time probe the components of the normal vectors, the calculated Raman intensities contain much information about the precision of the calculated eigenvectors. The displacement of the apical oxygen has the strongest effect on the electronic structure and thus gives rise to the biggest scattering intensity [69, 70] among the A_{1g} modes in (zz)-polarization. Since $\partial\epsilon^{zz}(\omega)/\partial u_{O4}$, i.e. the change of the dielectric function with O4 displacement, is large, the contribution of the apical oxygen plays an important role for the Raman intensity of both, the O4 and the O2+O3 mode. The dependence

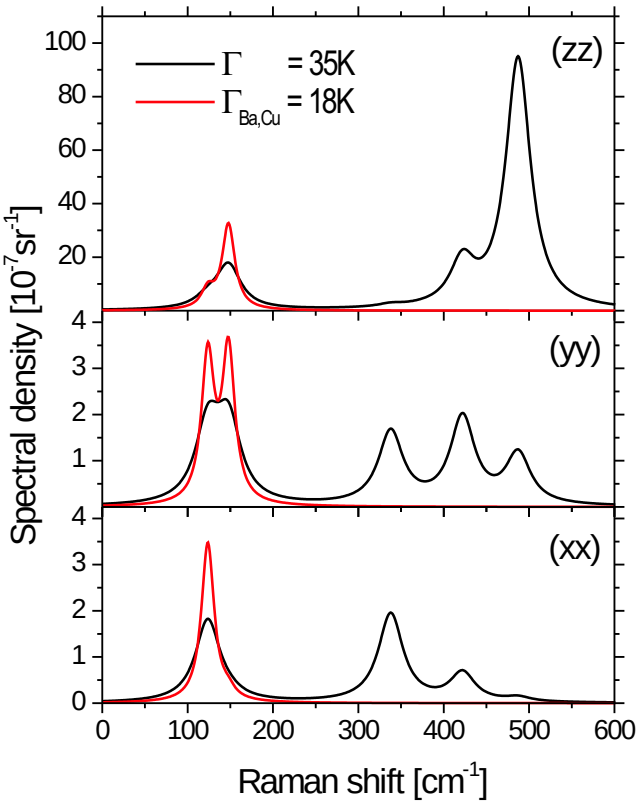

Figure 7.1: Calculated Raman intensities (black lines) of the A_{1g} modes for a laser wavelength of 514 nm in (xx)-, (yy)-, and (zz)-polarization at room temperature. An overall lifetime broadening of Γ=35 K was used. For comparison, the grey curves show the corresponding spectra for the Ba and Cu mode, when Γ=18 K.

of $\epsilon^{zz}(\omega)$ upon displacement of the atoms with respect to the eigenvectors of these two modes, is seen in Figs. 7.4 and 7.5. The strong change with the O4 coordinate (eigenvector) arises due to the large $z-$coordinate matrix element between the O4(p_z) and the Cu1$(d_{z^2-y^2})$ orbitals contributing to $\epsilon^{zz}(\omega)$. Due to a resonance of the incident light with the interband transition between the bands where these orbitals are heavily involved $\epsilon^{zz}(\omega)$ is strongly modulated by the ion's displacement. For the in-plane states this matrix element arises only due to the small buckling of the CuO_2 layers being weakly modulated by the displacements of plane oxygen ions. For this reason the plane oxygen atoms give a relatively small contribution to the Raman activity in (zz)-polarization.

In previous publications, a good overall agreement between theory and experi-

ment for the Raman intensities as a function of ω_L was found. The only exception was the O2–O3 mode in (zz)-polarization where a much too high intensity was obtained by the LMTO calculations [69]. This behavior can be understood by the large contribution of the O4 displacement in the normal vector used in Reference [69]. As can be seen in Figs. 7.1 and 7.3 this discrepancy is lifted when taking into account the eigenvector displayed in Table 7.1. In excellent agreement with experiment [68, 69] the intensity of the O4 mode at the peak position is approximately 7 times as big as for the O2+O3 mode, whereas the Raman efficiency of the O2–O3 mode is two orders of magnitude smaller than that of the O4 vibration.

During the vibrations of B_{2g} and B_{3g} symmetry, the atoms are displaced from positions lying in a mirror plane. The displacement to both directions is equivalent leading to a symmetric potential and a saddle point in the diagonal components of the dielectric function $\epsilon^{jj}(\omega)$. For the latter reason, the first derivative of this quantity and hence the Raman intensity in diagonal polarizations is zero. Due to the lowering of the symmetry finite non-diagonal terms are allowed but very small. Indeed, the measured Raman intensities are two orders of magnitude smaller than those of the A_{1g} modes. This finding is also reproduced by the present calculations.

7.2.3 Matrix Transformation for the Site-selective Isotope Substitution

Here it will be demonstrated how to obtain the eigenmodes and the variation of the dielectric function in case of site-selectively substituted crystals. Starting with the transformation of the dynamical matrix, which has the form

$$\widetilde{D} = S^{\mathrm{I}} D S^{\mathrm{I}} \tag{7.1}$$

where the diagonal matrix for the substitution of the atom with the mass M_m is written in the form $S^{\mathrm{I}}_{jj} = 1$ or $S^{\mathrm{I}}_{jj} = \sqrt{M_m/\widetilde{M}_m}$ where $\widetilde{M}_m$ specifies the mass of the introduced isotope and m numerate the ions. From the modified $\widetilde{D}$ the new eigenfrequencies and the corresponding eigenvectors $\widetilde{u}^{(m)}_\zeta$ are obtained. With the new eigenvectors the variations of the dielectric function $\delta\widetilde{\epsilon}_\zeta$ can be related to the already known results for $\delta\epsilon_\zeta$ in the following way. In A_{1g} taken as an example, the non-substituted crystal's $\delta\epsilon_\zeta$ is given by :

$$\begin{pmatrix} \delta\epsilon_1 \\ \delta\epsilon_2 \\ \delta\epsilon_3 \\ \delta\epsilon_4 \\ \delta\epsilon_5 \end{pmatrix} = \begin{pmatrix} u^{(1)}_{Ba} & u^{(1)}_{Cu} & u^{(1)}_{O2} & u^{(1)}_{O3} & u^{(1)}_{O4} \\ \cdot & \cdot & \cdot & \cdot & \cdot \\ \cdot & \cdot & \cdot & \cdot & \cdot \\ \cdot & \cdot & \cdot & \cdot & \cdot \\ u^{(5)}_{Ba} & u^{(5)}_{Cu} & u^{(5)}_{O2} & u^{(5)}_{O3} & u^{(5)}_{O4} \end{pmatrix} \begin{pmatrix} \partial\epsilon/\partial u_{Ba} \\ \cdot \\ \cdot \\ \cdot \\ \partial\epsilon/\partial u_{O4} \end{pmatrix} \tag{7.2}$$

The derivatives $\partial\epsilon/\partial u_m$ which are not changed with the substitution can be obtained as:

$$\begin{pmatrix} \partial\epsilon/\partial u_{Ba} \\ \cdot \\ \cdot \\ \cdot \\ \partial\epsilon/\partial u_{O4} \end{pmatrix} = \begin{pmatrix} u_{Ba}^{(1)} & u_{Cu}^{(1)} & u_{O2}^{(1)} & u_{O3}^{(1)} & u_{O4}^{(1)} \\ \cdot & \cdot & \cdot & \cdot & \cdot \\ \cdot & \cdot & \cdot & \cdot & \cdot \\ \cdot & \cdot & \cdot & \cdot & \cdot \\ u_{Ba}^{(5)} & u_{Cu}^{(5)} & u_{O2}^{(5)} & u_{O3}^{(5)} & u_{O4}^{(5)} \end{pmatrix}^{-1} \begin{pmatrix} \delta\epsilon_1 \\ \delta\epsilon_2 \\ \delta\epsilon_3 \\ \delta\epsilon_4 \\ \delta\epsilon_5 \end{pmatrix} \tag{7.3}$$

Therefore, in the substituted crystals the variation of the dielectric function is given by:

$$\begin{pmatrix} \delta\widetilde{\epsilon}_1 \\ \delta\widetilde{\epsilon}_2 \\ \delta\widetilde{\epsilon}_3 \\ \delta\widetilde{\epsilon}_4 \\ \delta\widetilde{\epsilon}_5 \end{pmatrix} = \begin{pmatrix} \widetilde{u}_{Ba}^{(1)} & \widetilde{u}_{Cu}^{(1)} & \widetilde{u}_{O2}^{(1)} & \widetilde{u}_{O3}^{(1)} & \widetilde{u}_{O4}^{(1)} \\ \cdot & \cdot & \cdot & \cdot & \cdot \\ \cdot & \cdot & \cdot & \cdot & \cdot \\ \cdot & \cdot & \cdot & \cdot & \cdot \\ \widetilde{u}_{Ba}^{(5)} & \widetilde{u}_{Cu}^{(5)} & \widetilde{u}_{O2}^{(5)} & \widetilde{u}_{O3}^{(5)} & \widetilde{u}_{O4}^{(5)} \end{pmatrix} \times \tag{7.4}$$

$$\times \begin{pmatrix} u_{Ba}^{(1)} & u_{Cu}^{(1)} & u_{O2}^{(1)} & u_{O3}^{(1)} & u_{O4}^{(1)} \\ \cdot & \cdot & \cdot & \cdot & \cdot \\ \cdot & \cdot & \cdot & \cdot & \cdot \\ \cdot & \cdot & \cdot & \cdot & \cdot \\ u_{Ba}^{(5)} & u_{Cu}^{(5)} & u_{O2}^{(5)} & u_{O3}^{(5)} & u_{O4}^{(5)} \end{pmatrix}^{-1} \begin{pmatrix} \delta\epsilon_1 \\ \delta\epsilon_2 \\ \delta\epsilon_3 \\ \delta\epsilon_4 \\ \delta\epsilon_5 \end{pmatrix} \tag{7.5}$$

With the knowledge of $\delta\widetilde{\epsilon}_\zeta$ one can then calculate the Raman intensities in the selectively substituted crystals.

7.2.4 Site-Selective Isotope Effect in Raman Spectra

Replacement of oxygen atoms by their ^{18}O isotopes has two effects on the Raman spectra. First, the vibrational frequencies are lowered due to the increased ionic mass. Second, the phonon eigenvectors are altered as well. As already mentioned above, the Raman intensities strongly depend on the eigenvector of a mode, and therefore modifications in the eigenvectors directly cause changes in the phonon intensities [71]. In contrast, a substitution of all oxygens by isotopes, only causes a frequency decrease of the oxygen modes by $\sqrt{16/18}$ and does not affect the eigenvectors, since the oxygen modes can be regarded to be decoupled from the Ba-Cu subsystem.

Figure 7.6 presents the Raman intensities for two different cases of the ^{16}O $\rightarrow^{18}$O substitution compared to the results for the non-substituted crystal. The eigenvectors and frequencies are represented in Tables 7.2 and 7.3, respectively.

The dramatic effects of the site-selective substitution on the intensities of the O2+O3 mode and the O4 mode can be understood in the following way. In the

sym.	mode	ω	$\Delta\omega$	$\Delta\omega_{exp}$	Ba	Cu2	O2	O3	O4
A_{1g}	O2–O3	318.5	-19.3	-17	0.01	-0.03	0.77	-0.63	-0.01
	O2+O3	399.7	-22.2	-21	0.03	0.12	-0.61	-0.75	-0.21
	O4	485.0	-2.0		-0.03	0.01	-0.14	-0.19	0.97
B_{2g}	O4	222.4	0.0		0.27	0.09	0.03	0.05	-0.96
	O3	368.6	-20.2		0.00	-0.30	0.04	0.95	0.02
	O2	564.3	-29.0		0.00	-0.38	0.91	-0.17	-0.02
B_{3g}	O4	292.9	0.0		-0.18	-0.03	-0.04	0.01	0.98
	O2	353.5	-18.7		0.00	-0.34	0.94	0.08	0.02
	O3	518.6	-27.3		0.00	-0.35	-0.22	0.91	-0.03

Table 7.2: Phonon frequencies and frequency shifts (in cm^{-1}), and eigenvectors for the oxygen modes in A_{1g}, B_{2g} and B_{3g} symmetries for plane oxygen isotope substitution. Experimental data are taken from Reference [52].

sym.	mode	ω	$\Delta\omega$	$\Delta\omega_{exp}$	Ba	Cu2	O2	O3	O4
A_{1g}	O2–O3	337.8	0.0		-0.01	0.03	-0.78	0.63	0.01
	O2+O3	418.3	-3.6	-8	0.04	0.11	-0.55	-0.67	-0.49
	O4	463.1	-23.9	-24	0.02	-0.03	0.28	0.35	-0.90
B_{2g}	O4	210.8	-11.6		0.27	0.09	0.03	0.04	-0.96
	O3	388.8	0.0		0.00	-0.30	0.06	0.95	0.02
	O2	593.3	0.0		0.00	-0.37	0.91	-0.18	-0.02
B_{3g}	O4	276.7	-16.2		0.18	0.03	0.02	-0.00	-0.98
	O2	372.2	0.0		0.00	-0.34	0.93	0.11	0.01
	O3	545.9	0.0		0.00	-0.34	-0.23	0.91	-0.03

Table 7.3: Phonon frequencies and frequency shifts (in cm^{-1}), and eigenvectors for the oxygen modes in A_{1g}, B_{2g} and B_{3g} symmetries for apical oxygen isotope substitution. Experimental data are taken from Reference [52].

non-substituted crystals these modes are close in frequency and hence considerably mixed [68]. In the case of ^{18}O4 (^{18}O2,^{18}O3) substitution the modes become more (less) close in frequency, and, therefore, the vibrations of the atoms involved get more (less) strongly coupled. This fact leads to changes in the Raman intensities, as shown in Figure 7.6, and their resonant behavior.

Excellent agreement between theory and experiment is found for the frequency shifts (see Tables 7.2 and 7.3) where experimental data are available [52]. The relatively small deviations from the measured values can be understood by the uncertainties in the substitution: For the O4 substituted samples a 15% replacement of the plane oxygens was estimated. Since the O4 mode is nearly completely decoupled from the plane atoms, the additional replacement of plane oxygens does not affect the O4 frequency. In this case, the experimental frequency shift is in perfect agreement with theory. In contrast, the shift of the experimental O2+O3

frequency is enhanced by the ^{18}O content of the planes. The same holds for the O2–O3 mode, where a small frequency shift can be seen in the spectrum, but no experimental value is given in Reference [52]. At the plane oxygen substitution only a 5% replacement of the apical and chain oxygen was determined. Therefore the effects can be estimated to be much smaller than in the case discussed above. The experimental scattering intensities also allow for a comparison with the calculated spectra to some extent: e.g. the relative increase of the O2+O3 mode with respect to the O4 mode, when ^{16}O4 is replaced by ^{18}O4, is well reproduced by our calculations. For a detailed analysis, however, more information from experimental side is needed.

Isotope substitution at the ^{134} Ba and ^{65}Cu sites shows only a minor influence on the intensities of corresponding phonons. This effect can be understood by the small mixing of these modes, clearly seen in Table 7.1. The effect on phonon frequencies and eigenvectors of the Ba and Cu dominated modes in all three symmetry classes are shown in Tables 7.4 and 7.5.

sym.	mode	ω	$\Delta\omega$	$\Delta\omega_{exp}$	Ba	Cu2	O2	O3	O4
A_{1g}	Ba	124.4	-1.2	-1.3±0.2	0.89	0.44	0.05	0.05	0.04
	Cu	147.6	-0.3	-0.1±0.2	0.44	-0.89	-0.08	-0.05	-0.00
B_{2g}	Ba	65.8	-0.6		-0.89	-0.30	-0.14	-0.08	-0.29
	Cu	142.3	-0.2	0.0±0.5	0.35	-0.82	-0.38	-0.24	0.00
B_{3g}	Ba	80.0	-0.8		-0.91	-0.33	-0.10	-0.16	-0.18
	Cu	140.9	-0.2	-0.4±0.5	-0.37	0.81	0.25	0.37	-0.04

Table 7.4: Phonon frequencies and frequency shifts (in cm^{-1}), and eigenvectors for the barium and cooper mode for A_{1g}, B_{2g} and B_{3g} symmetries for barium isotope substitution. Experimental values are taken from Reference [72].

sym.	mode	ω	$\Delta\omega$	$\Delta\omega_{exp}$	Ba	Cu2	O2	O3	O4
A_{1g}	Ba	122.9	-0.3	-0.2±0.2	0.90	0.44	0.05	0.05	0.04
	Cu	145.9	-1.3	-2.1±0.2	0.44	-0.90	-0.07	-0.05	-0.00
B_{2g}	Ba	65.1	-0.1		-0.90	-0.30	-0.14	-0.08	-0.29
	Cu	141.1	-1.1	-0.7±0.5	0.35	-0.83	-0.38	-0.23	0.00
B_{3g}	Ba	79.1	-0.1		-0.91	-0.33	-0.10	-0.15	-0.18
	Cu	139.6	-1.0	-1.3±0.5	-0.37	0.82	0.25	0.37	-0.03

Table 7.5: Phonon frequencies and frequency shifts (in cm^{-1}), and eigenvectors for the barium and cooper mode for A_{1g}, B_{2g} and B_{3g} symmetries for copper isotope substitution. Experimental values are taken from Reference [72].

Comparison with experiments [72] for the A_{1g} modes as discussed in Reference [73] demonstrates excellent agreement again confirming the precision of the calculated eigenvectors.

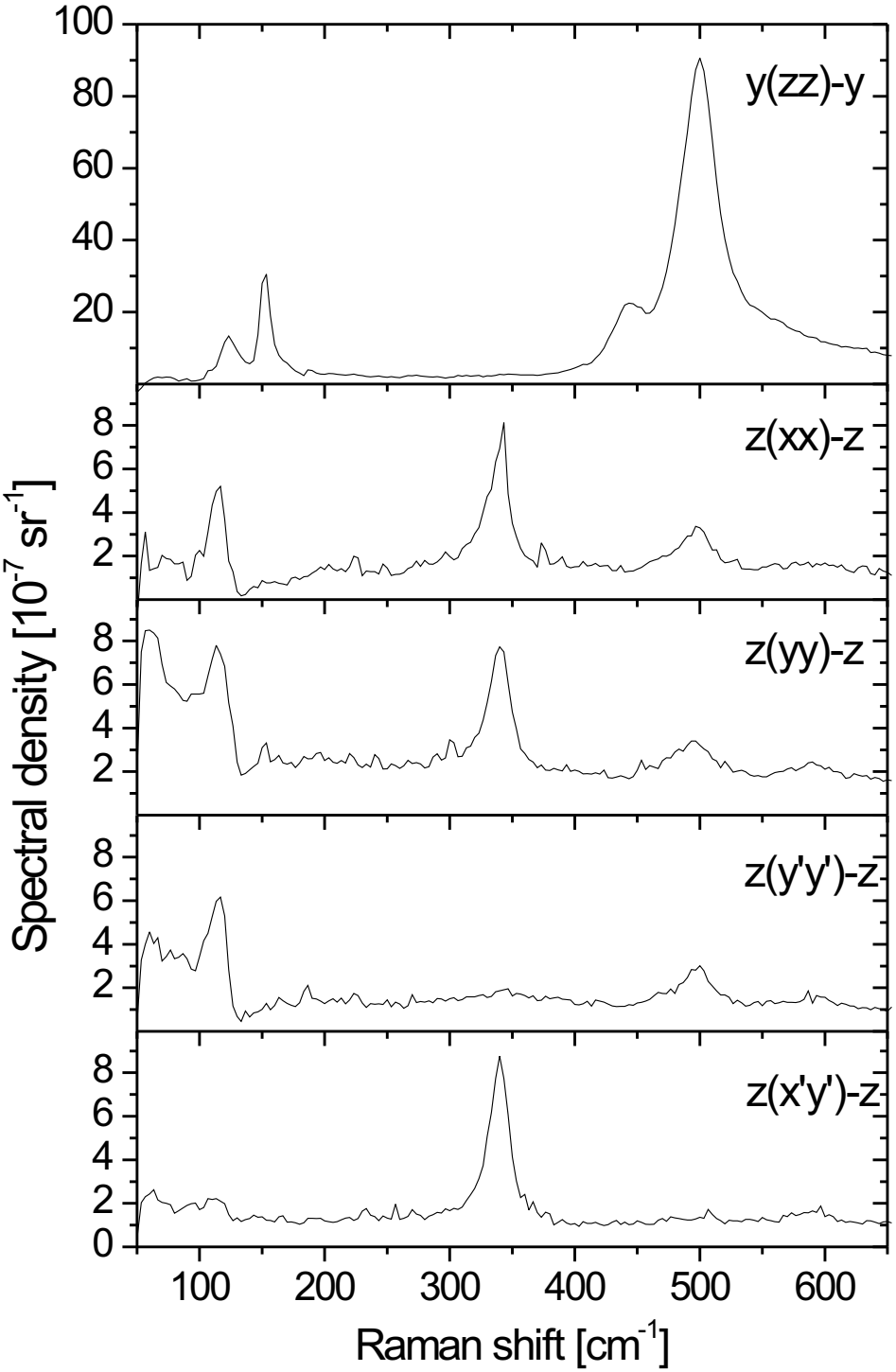

Figure 7.2: Measured Raman intensities in different geometries for a laser wavelength of 514 nm at room temperature taken from [33]. The A_{1g} frequencies are 123 cm^{-1}, 152 cm^{-1}, 338 cm^{-1}, 442 cm^{-1}, and 500 cm^{-1}, respectively.

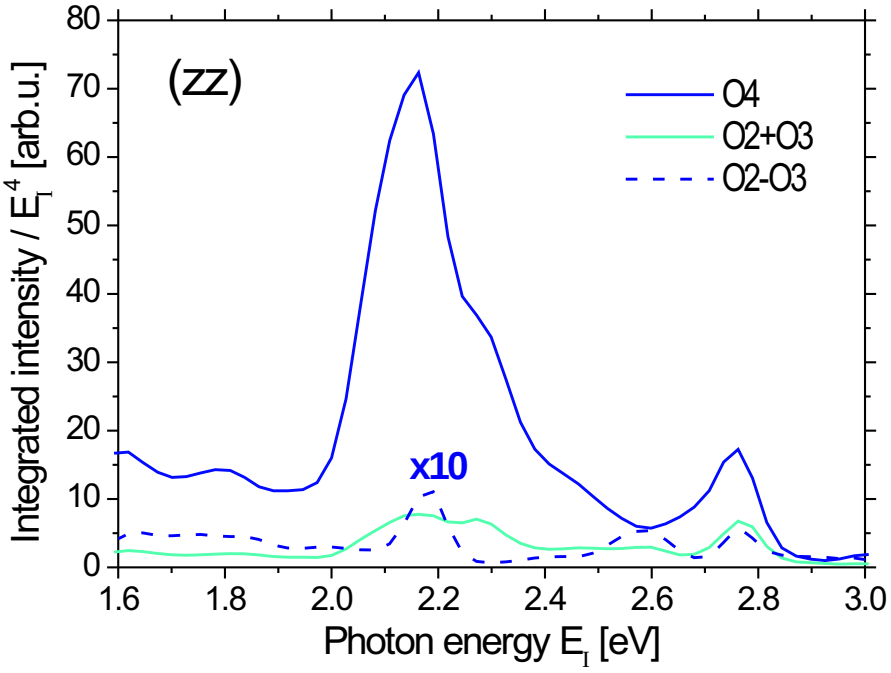

Figure 7.3: Resonance behavior of the Raman intensity in (zz)-polarization for the three oxygen dominated modes.

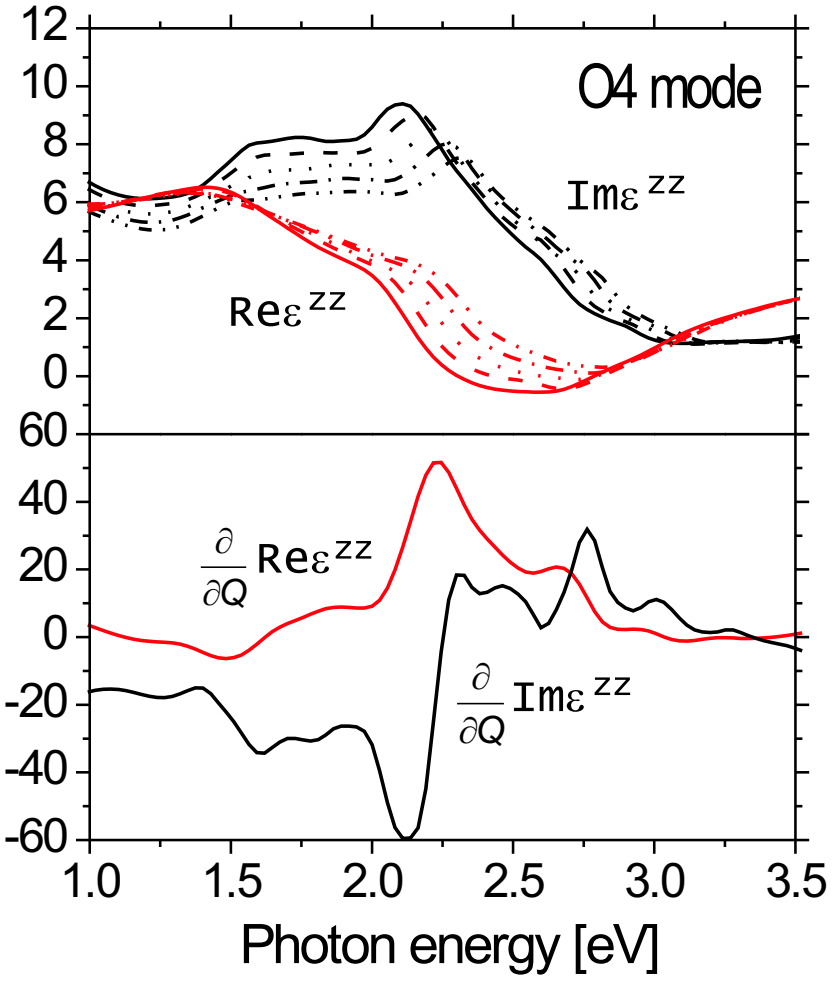

Figure 7.4: Real and imaginary part of the dielectric tensor component $\epsilon^{zz}(\omega)$ for different atomic displacements along the eigenvector of the O4 mode (upper panel). The lines correspond to the O4 displacements of 0.025 Å (solid), 0.0125 Å (dashed), 0 (dotted), -0.0125 Å (dash-dotted), and -0.025 Å (double dash-dotted), respectively. In addition the corresponding derivatives are displayed (lower panel).

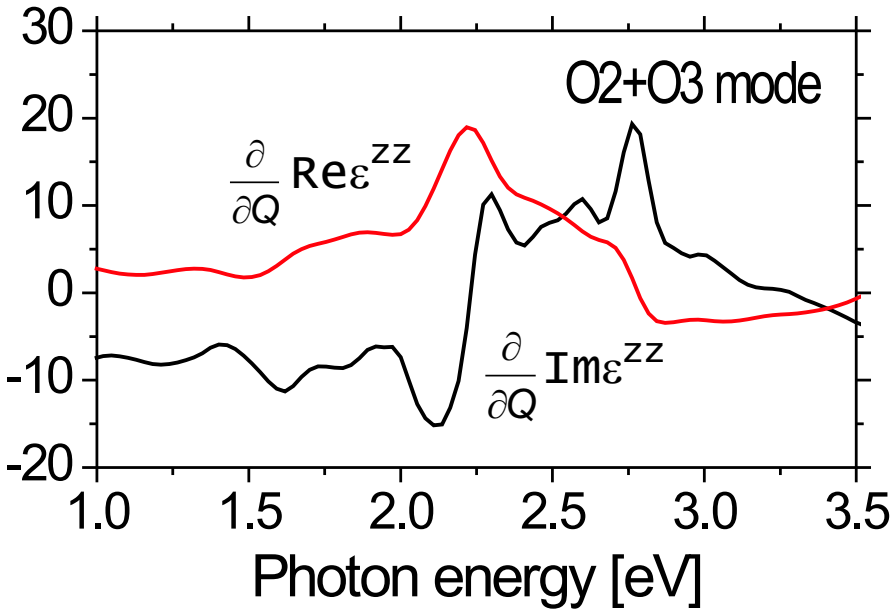

Figure 7.5: Derivatives of real and imaginary part of the dielectric tensor component $\epsilon^{zz}(\omega)$ with respect to the eigenvector of the O2+O3 mode.

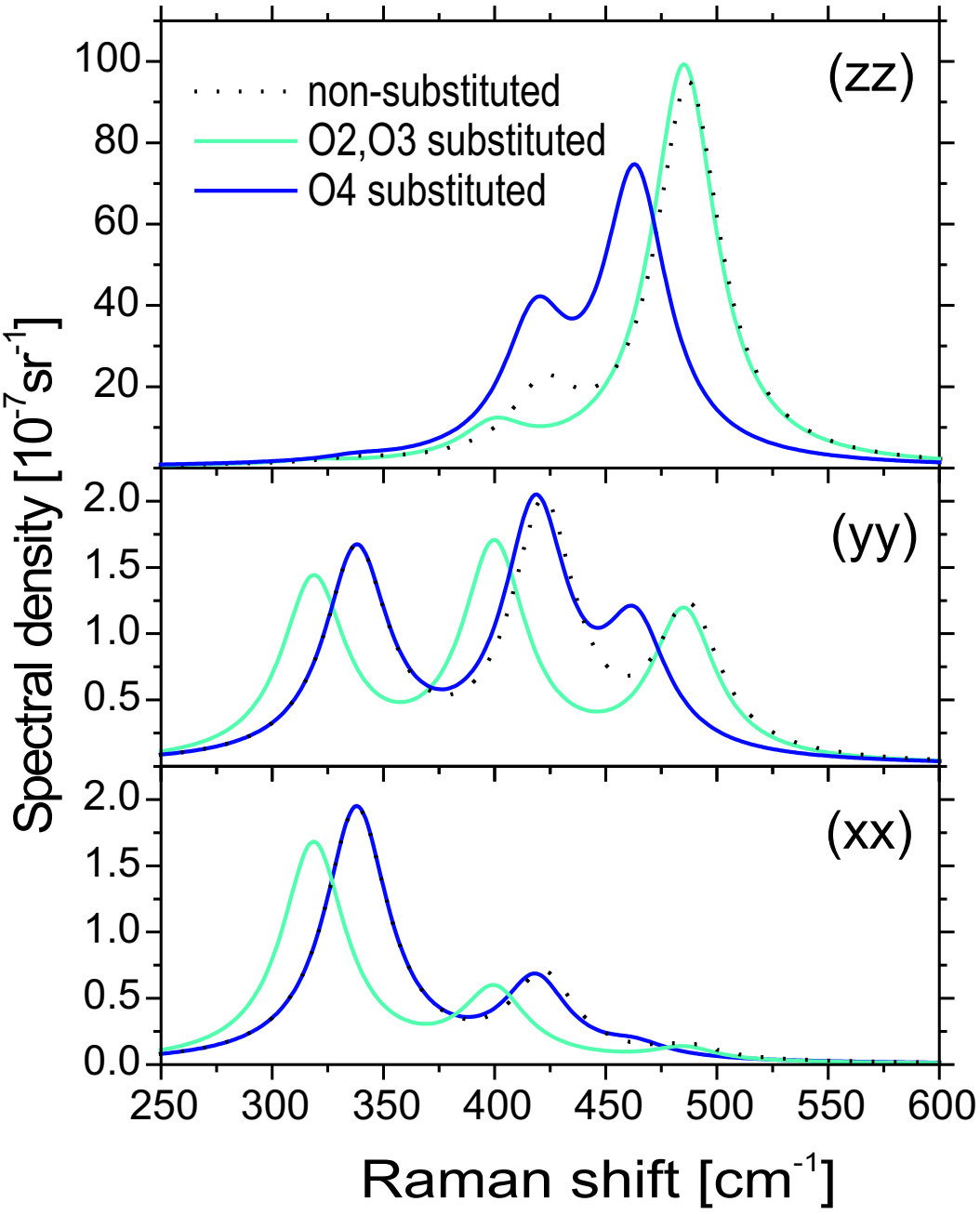

Figure 7.6: Site-selective isotope effect on the Raman spectra of the three oxygen modes in (xx)-, (yy)-, and (zz)-polarization. The grey (black) lines indicate substitution of the plane (apex) oxygen atoms by O^{18}, whereas the dotted lines correspond to the case without substitution.

7.3 Y-Point Phonon Modes of $YBa_3Cu_3O_7$

In the following the calculated frequencies of non-zone-center phonon modes will be presented. More specifically, the calculation was done for the Y-point ($\vec{k}_Y = (0, \pi, 0)$) of the Brillouin zone with the help of supercell calculations. Thus it was also necessary to determine the symmetry coordinates for the $YBa_3Cu_3O_7$ unit cell doubled along the $y-$direction. In the following we will describe the procedure how to obtain them. Assume, the pattern of displacements in one elementary cell is known. The displacements in the second cell are related to the displacements in the first cell by the Bloch factor (see equation 2.48) which is equal to -1 in the Y-point. In this point the $xy-$ and $yz-$planes are symmetry planes. For this reason, the pattern of ion displacements can be either even or odd with respect to reflections in these planes. In the calculations only modes even with respect to the $xy-$plane reflection were considered since they possess a similar symmetry as the Raman active phonons in the $\Gamma-$point. Thus some of these modes could be traced back to the Raman active phonons if the entire interval of k_y could be investigated from 0 to π. Taking into account the symmetry with respect to the $yz-$plane reflection, the displacements of ions along the $x-$axis are zero. This procedure leads to 13 independent displacements, which are listed in Table 7.6. In this table the superscripts A and B describe in which half of the doubled unit cell an atom is located, while ' labels equivalent atoms. The structural data needed for this calculations are given in Table 7.7. It shall be noted that in a study of Andersen *et al.* [74] only 7 out of 13 possible displacements were taken into account. It can be seen in Table 7.8 that all the 13 displacements couple. However, it turned out that the coupling between the 7 displacements, which were considered in Reference [74], and the additional 6 displacements is very weak. Thus the increase in the number of degrees of freedom in the dynamical matrix D in equation 2.13 does not show dramatic effects on the eigenfrequencies.

The results of the calculations presented in Table 7.8 can help to assignment the modes obtained by neutron scattering experiments for the Y-point [75]. These theoretical data are also a good starting point for the calculation of electron-phonon coupling constants which are highly desirable to be known for arbitrary vectors of the Brillouin zone.

$Cu1^A$	$0,$	$\pm y_1,$	0	$Cu1^B$	$0,$	$\frac{1}{2} \mp y_1,$	0
$O1^A$	$0,$	$\frac{1}{4} \pm y_2,$	0	$O1^B$	$0,$	$\frac{3}{4} \mp y_2,$	0
$Cu2^A$	$0,$	$\pm y_3,$	$z_{Cu2} \pm z_3$	$Cu2^B$	$0,$	$\frac{1}{2} \mp y_3,$	$z_{Cu2} \mp z_3$
$Cu2^{A'}$	$0,$	$\pm y_3,$	$1 - z_{Cu2} \mp z_3$	$Cu2^{B'}$	$0,$	$\frac{1}{2} \mp y_3,$	$1 - z_{Cu2} \pm z_3$
$O2^A$	$\frac{1}{2},$	$\pm y_4,$	$z_{O2} \pm z_4$	$O2^B$	$\frac{1}{2},$	$\frac{1}{2} \mp y_4,$	$z_{O2} \mp z_4$
$O2^{A'}$	$\frac{1}{2},$	$\pm y_4,$	$1 - z_{O2} \mp z_4$	$O2^{B'}$	$\frac{1}{2},$	$\frac{1}{2} \mp y_4,$	$1 - z_{O2} \pm z_4$
$O3^A$	$0,$	$\frac{1}{4} \pm y_5,$	$z_{O3} \pm z_5$	$O3^B$	$0,$	$\frac{3}{4} \mp y_5,$	$z_{O3} \mp z_5$
$O3^{A'}$	$0,$	$\frac{1}{4} \pm y_5,$	$1 - z_{O3} \mp z_5$	$O3^{B'}$	$0,$	$\frac{3}{4} \mp y_5,$	$1 - z_{O3} \pm z_5$
$O4^A$	$0,$	$\pm y_6,$	$z_{O4} \pm z_6$	$O4^B$	$0,$	$\frac{1}{2} \mp y_6,$	$z_{O4} \mp z_6$
$O4^{A'}$	$0,$	$\pm y_6,$	$1 - z_{O4} \mp z_6$	$O4^{B'}$	$0,$	$\frac{1}{2} \mp y_6,$	$1 - z_{O4} \pm z_6$
Ba^A	$\frac{1}{2},$	$\frac{1}{4} \pm y_7,$	$z_{Ba} \pm z_7$	Ba^B	$\frac{1}{2},$	$\frac{3}{4} \mp y_7,$	$z_{Ba} \mp z_7$
$Ba^{A'}$	$\frac{1}{2},$	$\frac{1}{4} \pm y_7,$	$1 - z_{Ba} \mp z_7$	$Ba^{B'}$	$\frac{1}{2},$	$\frac{3}{4} \mp y_7,$	$1 - z_{Ba} \pm z_7$
Y^A	$\frac{1}{2},$	$\frac{1}{4} \pm y_8,$	$\frac{1}{2}$	Y^B	$\frac{1}{2},$	$\frac{3}{4} \mp y_8,$	$\frac{1}{2}$

Table 7.6: Atomic displacements for the Y-point vibrations.

lattice parameters
$a = 7.103$ Bohr
$b = 14.428$ Bohr
$c = 21.476$ Bohr
atomic positions $[c]$
$z_{Cu2} = 0.3505$
$z_{O2} = 0.3772$
$z_{O3} = 0.1620$
$z_{O4} = 0.1813$
$z_{Ba} = 0.6237$

Table 7.7: Optimized structural data for a unit cell doubled in y-direction.

ω [cm^{-1}]	Y(y)	Ba(y)	Ba(z)	Cu1(y)	Cu2(y)	Cu2(z)	O1(y)	O2(y)	O2(z)	O3(y)	O3(z)	O4(y)	O4(z)
538.9	-0.01	0.02	0.00	0.00	0.00	-0.02	-0.74	0.00	0.07	0.16	-0.02	0.00	-0.65
459.7	-0.04	-0.02	0.00	0.00	0.00	0.01	0.54	-0.01	0.03	0.71	0.00	0.00	-0.45
441.6	0.00	0.00	0.03	0.09	0.28	0.00	-0.01	-0.88	-0.01	0.01	-0.22	-0.29	0.02
427.4	-0.01	0.00	0.00	-0.04	0.00	0.03	-0.39	0.02	-0.14	0.68	-0.10	0.10	0.59
420.1	-0.01	0.00	-0.03	0.30	-0.09	0.00	-0.06	0.13	0.00	0.10	0.53	-0.76	0.08
358.4	0.01	0.00	-0.01	0.22	0.12	0.02	0.02	0.40	-0.03	-0.02	-0.78	-0.41	-0.02
340.3	-0.13	-0.04	0.00	-0.03	0.01	-0.11	-0.02	0.01	0.97	0.06	-0.05	-0.02	0.15
269.9	0.00	0.00	-0.21	0.76	-0.51	0.00	0.00	-0.16	0.03	0.00	-0.09	0.28	0.01
254.3	-0.01	0.00	-0.02	0.49	0.79	-0.01	0.00	0.16	0.02	0.00	0.20	0.27	0.01
201.7	0.88	-0.07	0.00	0.00	0.00	-0.46	0.01	0.00	0.06	0.05	0.00	0.00	0.00
165.9	-0.28	-0.84	0.02	0.00	-0.01	-0.44	-0.02	0.00	-0.12	-0.02	-0.01	0.00	0.00
109.2	-0.27	0.44	0.58	0.11	-0.06	-0.61	0.02	0.00	-0.09	0.00	-0.01	0.02	0.01
105.2	0.21	-0.30	0.79	0.15	-0.08	0.46	-0.01	0.00	0.08	0.00	0.01	0.04	0.00

Table 7.8: Eigenfrequencies (cm^{-1}) and eigenvectors of the even phonon modes at the Y-point.

Chapter 8

The Results for $HgBa_2Ca_{n-1}Cu_nO_{2n+2}$

8.1 Computational Details

As in the previous Chapter, all the calculations have been performed within the LAPW method using the WIEN97 code [76]. The exchange and correlation effects have been treated in the local density approximation (LDA). In case of Hg-1201 the Brillouin zone integrations have been carried out on a $\vec{k}$-point mesh consisting of 42 points (in the irreducible wedge) applying a Gaussian smearing of 0.002 mRy. The number of $\vec{k}$-points has been reduced according to the unit-cell volume in the treatment of Hg-1212, Hg-1223, and Hg-1234. In the calculations of the dielectric tensors and the densities of states the number of $\vec{k}$-points has been increased by roughly a factor of 10. The basis set included about 1500 -2000 LAPW's supplemented by local orbitals for the low-lying semicore-states Hg-5p, Ba-5s, Ba-5p, Cu-3p and O-2s, Ca-3s, and Ca-3p. The atomic sphere radii have been chosen to be 2.0, 2.2, 1.9, 1.55, and 2.0 a.u. for Hg, Ba, Cu, O and Ca, respectively.

8.2 Hg-1201

8.2.1 The Optimization of the Crystal Structure

The starting point for the optimization procedure was the experimentally determined equilibrium volume $V_{\rm ref}$ of 976.3 a.u.^{3} with the corresponding structural data taken from Reference [49] (see also Table 8.1). For each volume the lattice parameters, i.e. the c/a-ratio, was optimized also allowing for the relaxation of the coordinates $z_{\rm Ba}$ and $z_{\rm O2}$. Figure 8.1 shows the total energy as a function of the unit cell volume. The calculated equilibrium volume turned out to be about 0.5% bigger than the experimental one [49], the c/a-ratio was found to be somewhat

		V	a	c	c/a
		$[a.u.^3]$	$[a.u.]$	$[a.u.]$	
Theory	this work	981.2			
		976.3	7.289	18.373	2.521
	Ref. [77]	1008.3	7.500	17.925	2.390
Experiment	Ref. [49]	976.3	7.362	18.015	2.447
	Ref. [78]	967.7	7.332	18.000	2.455

Table 8.1: Structural data of Hg-1201 obtained by the optimization procedure in comparison to data from the literature. The volume of 981.2 $a.u.^3$ has the lowest total energy (see text).

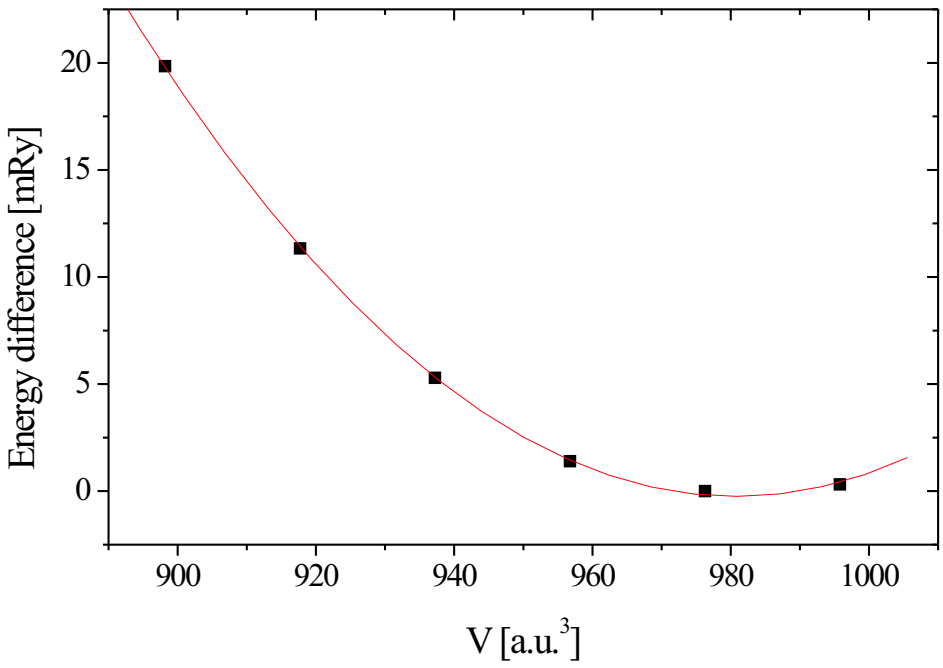

Figure 8.1: Total energy of $HgBa_2CuO_4$ with respect to the minimum energy as a function of the unit cell volume.

(+3%) larger than experimentally observed (see Table 8.1). This finding seems to be in contradiction to the common behavior of LDA based calculations, which generally show the trend of overbinding. The discrepancy, however, is much bigger for the results of Novikov *et al.* [77], who determined the equilibrium volume to be about 5% larger than the reference volume used [78]. At the same time a deviation in the c/a-ratio of -3% was obtained. In order to prove the quality of the lattice parameters obtained within the LAPW method, the total energy for the equilibrium data suggested by Novikov *et al.* has been computed, which was found to be by about 7.8 mRy higher. The discrepancy between the two structural data sets may only be traced back to differences between the LAPW and the FLMTO method (basis set) or to different convergence parameters. The influence of the $\vec{k}$-point mesh turned out not to be crucial.

A possible explanation for the *missing* difference between the experimentally and the theoretically obtained structural data may be found in the fact that the calculated data represent the lattice parameters for zero temperature with δ=0, whereas the experimental values are obtained from crystals at T=295 K and a finite oxygen doping level of δ=0.04 [49] [1]. Since the theoretical volume is very close to the experimental one, the latter one has been adopted to be the *optimal* volume $V_{\rm opt}$ = 976.3 $a.u.^3$, taking into account the 3% increased c/a-ratio and the relaxed atomic positions.

8.2.2 The Pressure Dependence of the Structural Data

The relation between pressure and the relative unit cell volume is presented in Figure 8.2. The pressure has been calculated according to the analytic expression $P = -\partial E(V)/\partial V$ by differentiating the fit curve of Figure 8.1. The change of the unit cell volume with pressure is almost linear up to 8 GPa. The same behavior was also found in Reference [77] in the pressure range from 0-10 GPa. Table 8.2 gives more insight into the behavior of the lattice parameters and the internal atomic coordinates under pressure. A detailed study of the bond

$V/V_{\rm opt}$	V	a	c	$z_{\rm Ba}$	$z_{\rm O2}$
	$[a.u.^3]$	$[a.u.]$	$[a.u.]$	$[c]$	$[c]$
1.00	976.3	7.289	18.373	0.3003	0.2014
0.96	937.2	7.214	18.008	0.2967	0.2049
0.94	917.7	7.164	17.882	0.2952	0.2061
0.92	898.2	7.136	17.638	0.2928	0.2086

Table 8.2: Theoretically obtained structural data of Hg-1201 for different volumes.

[1] It will be shown below that doping results in a reduction of the unit cell volume.

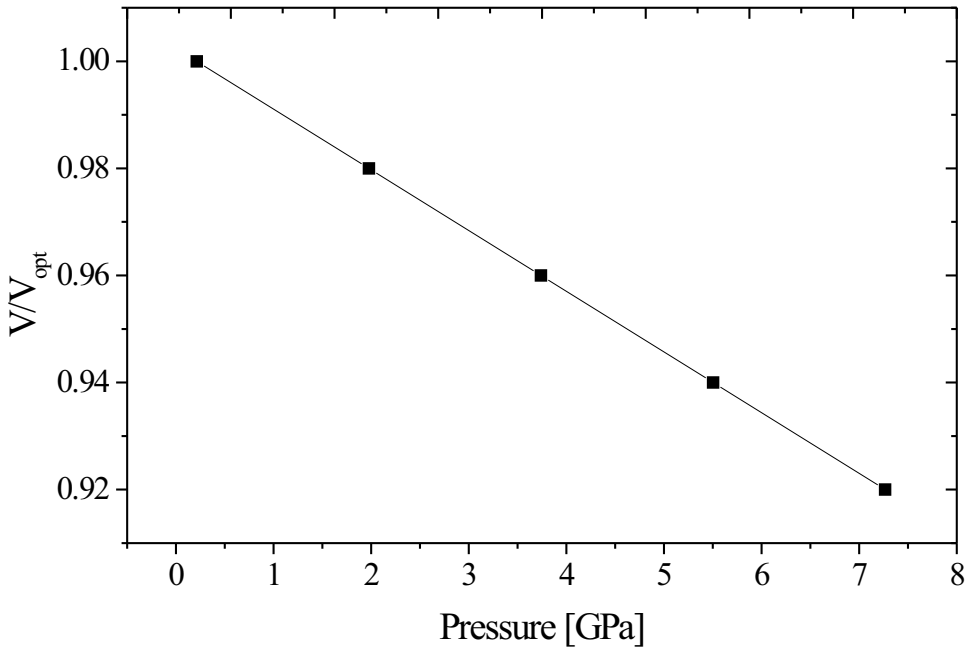

Figure 8.2: The pressure dependence of V/V_{opt}.

distances presented in Figure 8.3 indicates that nearly the whole change in the c parameter is due to the change of the Cu1-O2 bond, while the Hg-O2 bond reveals to be rigid, i.e. it shows a very small change with applied pressure. From this behavior a very strong pressure dependence of the electronic states in the Cu1-O1 plane might be expected due to the enhanced interaction of Cu1 with the apical oxygen O2.

Using the collection of data obtained during the optimization procedure the bulk modulus B, the compressibilities κ_V, κ_a, and κ_c, and the anisotropy parameter κ_c/κ_a have been calculated. The compressibility along an axis α with lattice constant l_α is given by

$$\kappa_\alpha = -\frac{1}{l_\alpha}\frac{\delta l_\alpha(P)}{\delta P}, \tag{8.1}$$

the volume compressibility by

$$\kappa_V = -\frac{1}{V}\frac{\delta V(P)}{\delta P} = \sum_\alpha \kappa_\alpha \tag{8.2}$$

and the bulk modulus by

$$B = \frac{1}{\kappa_V}. \tag{8.3}$$

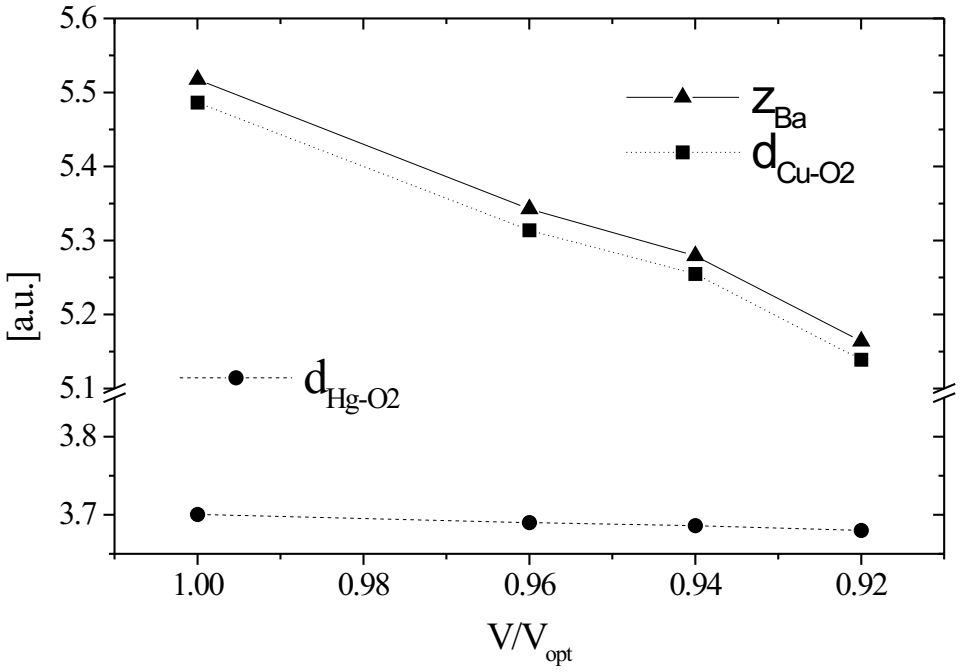

Figure 8.3: The bond distances of Hg-1201 as a function of the relative unit cell volume.

The calculated values (taken at $P \approx 0$) are displayed in Table 8.3. They are generally closer to the experimental data than most of the calculated results that have been published so far.

8.2.3 The Pressure Dependence of the Band Structure, the Density of States, and the Partial Charges

In Figure 8.4 the band structure of Hg-1201 along some high symmetry lines is shown for the optimized volume $V_{\rm opt}$. At the first sight it can be seen that the band states near the Fermi surface display a nearly two dimensional character. It can be observed that two bands intersect the Fermi level. One is a CuO_2 dominated band which appears as a characteristic in all the layered cuprates. This band crosses E_F between X and M, M and Γ, R and A, as well as between A and Z. The second band dips down to the Fermi level at X and is slightly below E_F at the R-point. This almost empty band can be identified to have Hg-O2 character. Comparing Figures 8.4 and 8.5 it can be seen that by increased pressure this band crosses the Fermi level when applying pressure and causes hole self-doping of the half filled Cu1($d_{x^2-y^2}$)-O1(p_x) band. Furthermore, the van Hove singularity at X shifts closer to the Fermi level and it might cross for pressures higher than 10 GPa as predicted in Ref. [79]. It was expected [79] that doping

	P [GPa]	κ_a	κ_c	κ_V	B	κ_c/κ_a	Ref.
Theory	0–7.2	3.31	5.07	11.6	86	1.53	this work
	0–0.6	3.50	6.21	13.0	77	1.77	[50]
	0–5.0	2.93	5.77	11.4	88	1.97	[50]
	0–10.0	2.60	5.50	10.4	96	2.12	[50]
		3.90	4.10	12.0	83	1.05	[79]
		4.00	3.40	11.4	88	0.85	[80]
Exp.	0-0.59	4.26	5.83	14.3	70	1.37	[78]
	0-5.07	3.34	4.58	11.4	88	1.37	[81]
	0-8.88	2.94	4.86	10.1	99	1.65	[82]

Table 8.3: Compressibilities in (10^{-3}GPa^{-1}) and bulk modulus in (GPa) of Hg-1201 compared to theoretical and experimental counterparts. P indicates the pressure range investigated.

with oxygen leads to similar effects, a topic which will be investigated in Section 8.6.

Figure 8.6 shows the total and the site-projected densities of states for Hg-1201 at the equilibrium volume $V_{\rm opt}$. It exhibits covalent bonding of Cu1 and O1 with peaks at $\approx$ -0.8 eV and small and nearly constant values at E_F. Additionally some covalent bonding can be resolved between Hg and O2, as well as between Ba and O1. The effects of pressure on the densities of states are characterized by shifts of the partial DOS's towards the Fermi level as depicted in Fig. 8.7.

Finally also the partial charges as a function of pressure have been investigated (see Table 8.4). As already mentioned, mainly the distances between the CuO_2 plane and the apical oxygen O2 decrease under applied pressure. This change is, in principle, reflected by an increase of the electron densities around these atoms. This fact, however, does not show up in the partial charges given in Table 8.4. The situation can be explained in the following way: As mentioned above, applying pressure leads to self-doping, i.e. the creation of holes in the Cu1-O1 plane. Thus one would expect smaller occupation numbers for the corresponding atomic spheres. These two effects partly cancel each other where the increase of the hole concentration should be stronger. Since, however, the muffin-tin radii of the atomic spheres have been kept constant when decreasing the unit cell volumes, the partial charges seem to stay approximately constant. For a more detailed analysis calculations with different sphere radii should be done.

8.2.4 The Raman Spectra and their Pressure Dependence

As already mentioned in Section 6.2.2 one would expect four peaks with different frequencies for the multi-polarized Raman spectra of $HgBa_2CuO_{4+\delta}$ with δ=0.

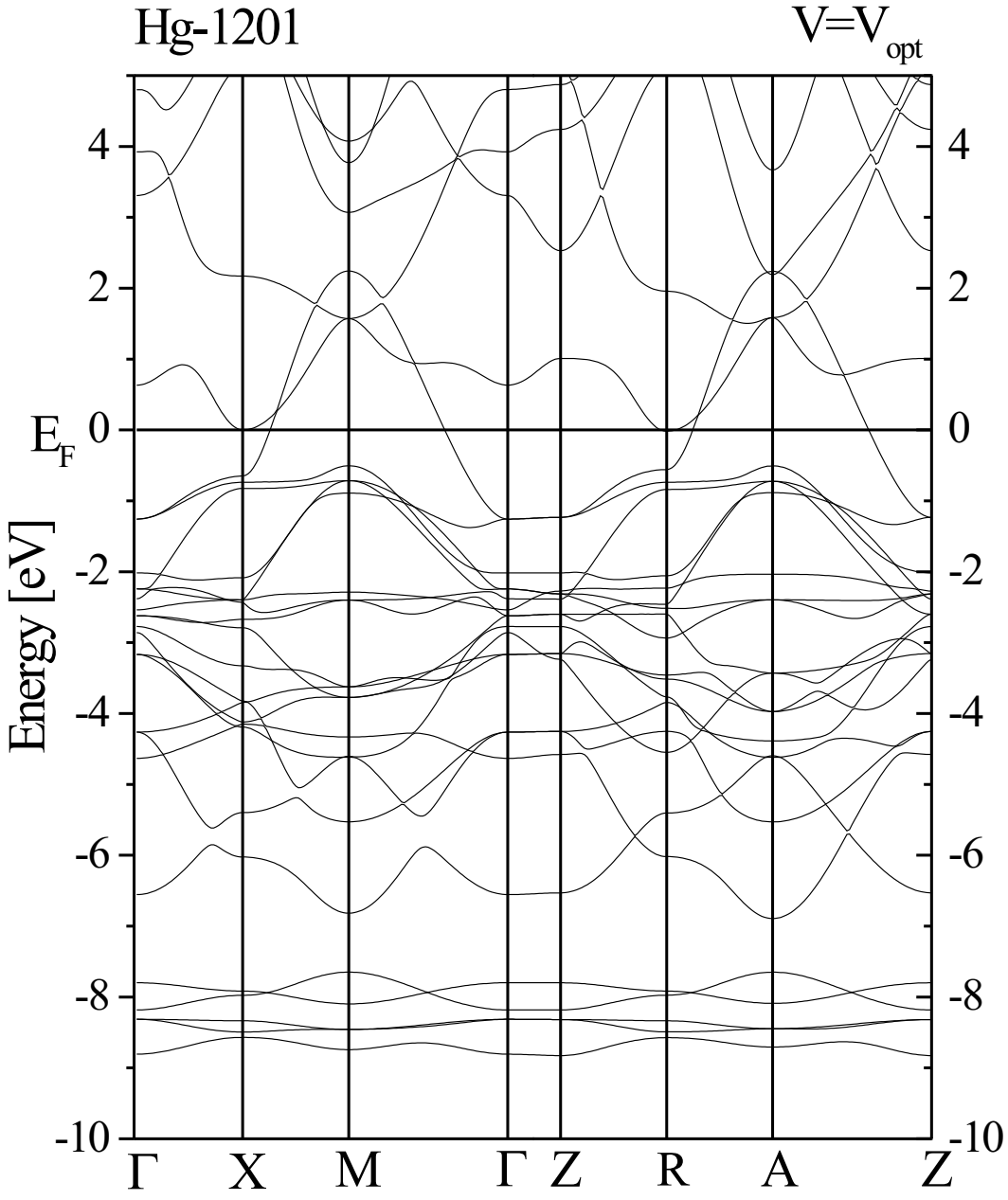

Figure 8.4: The band structure of Hg-1201 for the optimized unit cell volume.

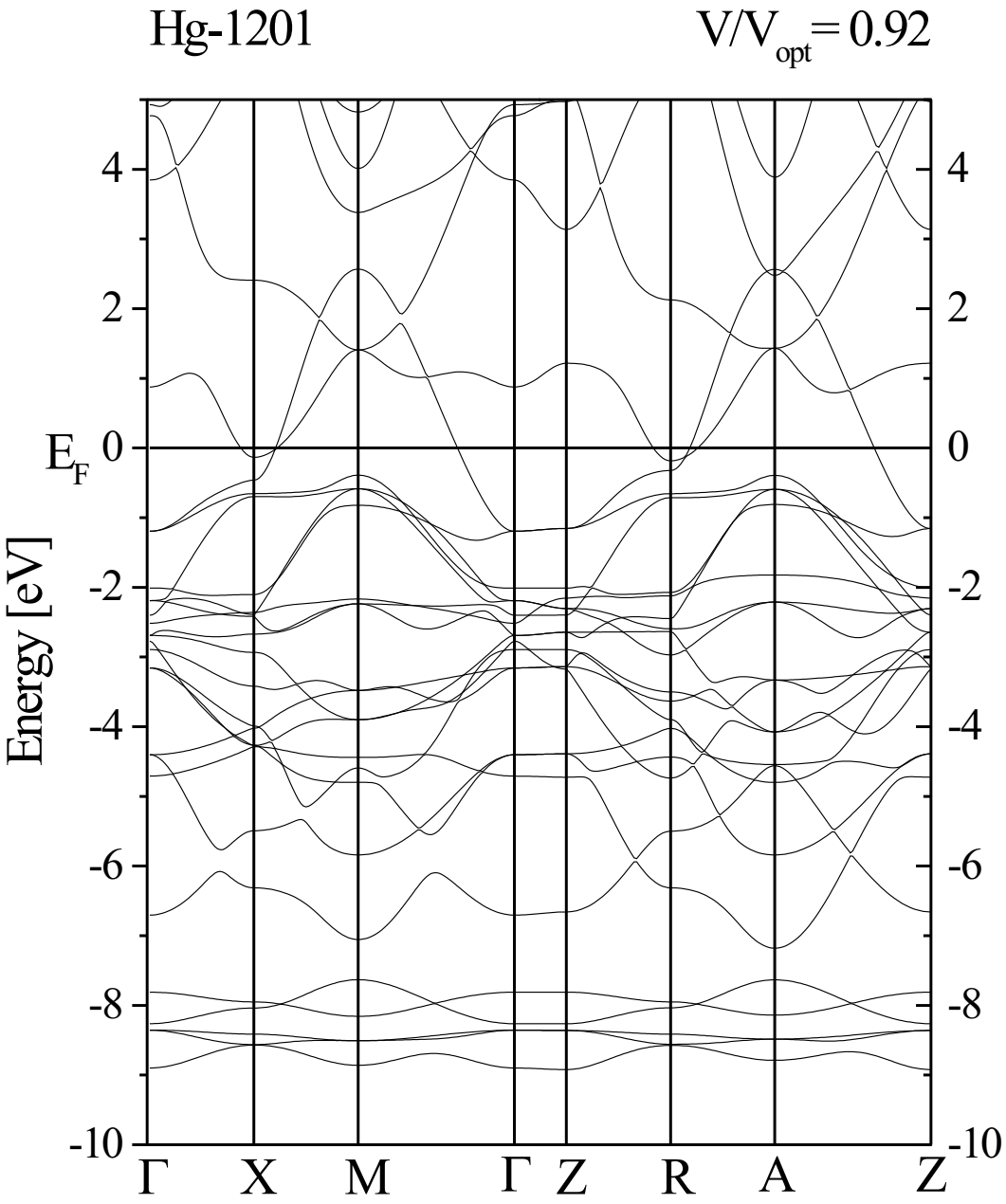

Figure 8.5: The band structure of Hg-1201 for V/V_{opt}=0.92.

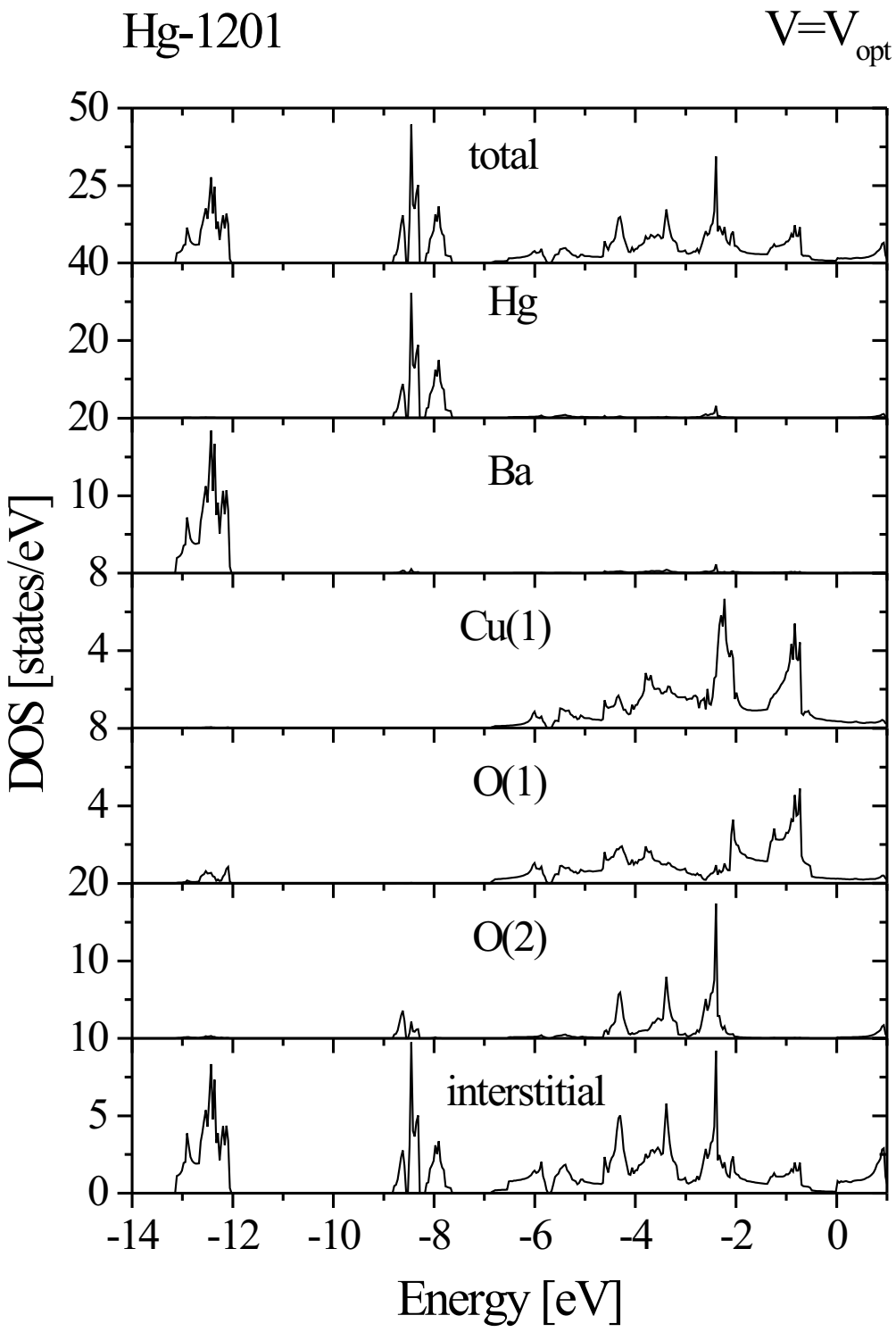

Figure 8.6: Total and partial densities of states of Hg-1201 for $V = V_{\mathrm{opt}}$.

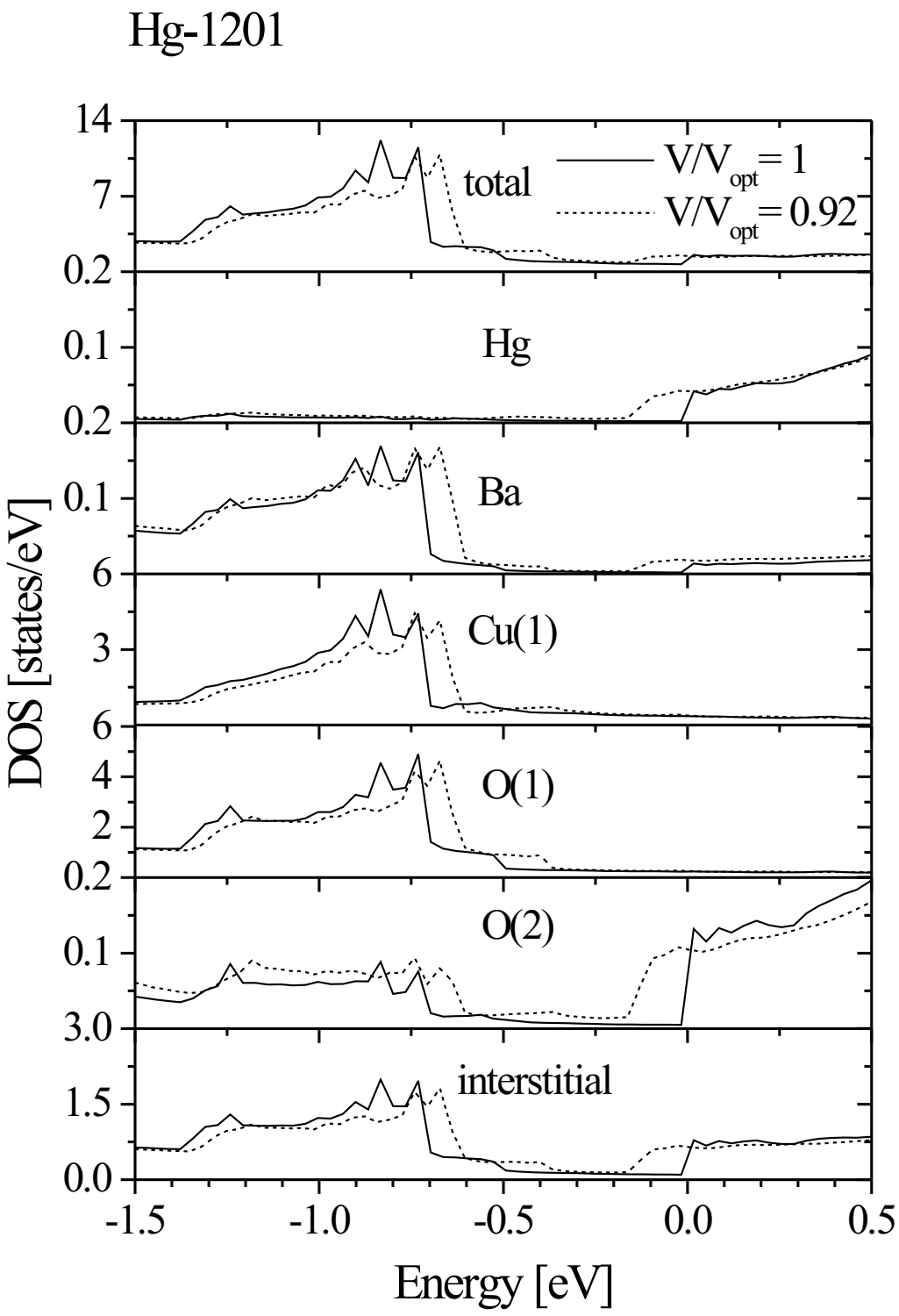

Figure 8.7: The total and site-projected DOS around the Fermi level for two different unit cell volumes.

	$V/V_{\rm opt}$	s	p	d	p_x	p_z	d_{z^2}	$d_{x^2-y^2}$	d_{xy}	d_{xz}
Hg	$V_{\rm ref}$	0.393	6.039	8.050	1.992	2.055	1.445	1.632	1.629	1.672
	1	0.393	6.041	8.049	1.992	2.056	1.440	1.633	1.630	1.674
	0.96	0.393	6.045	8.045	1.994	2.058	1.440	1.632	1.628	1.672
	0.92	0.393	6.050	8.040	1.996	2.059	1.440	1.630	1.627	1.672
Ba	$V_{\rm ref}$	1.738	4.280	10.004	1.430	1.421	2.000	2.000	2.001	2.002
	1	1.737	4.280	10.003	1.429	1.423	2.000	2.000	2.001	2.002
	0.96	1.738	4.283	10.004	1.430	1.422	2.000	2.000	2.001	2.002
	0.92	1.739	4.286	10.006	1.433	1.421	2.000	2.000	2.002	2.002
Cu1	$V_{\rm ref}$	0.217	6.150	8.705	2.067	2.017	1.750	1.440	1.854	1.830
	1	0.225	6.159	8.707	2.070	2.018	1.742	1.446	1.857	1.831
	0.96	0.229	6.170	8.703	2.075	2.020	1.747	1.431	1.859	1.833
	0.92	0.234	6.182	8.705	2.080	2.022	1.753	1.422	1.861	1.835
O1	$V_{\rm ref}$	1.528	3.442	0.010	1.120	1.204	0.001	0.003	0.002	0.002
	1	1.529	3.439	0.010	1.122	1.195	0.001	0.003	0.003	0.002
	0.96	1.529	3.451	0.011	1.124	1.202	0.002	0.003	0.003	0.002
	0.92	1.529	3.451	0.011	1.129	1.202	0.002	0.003	0.003	0.002
O2	$V_{\rm ref}$	1.545	3.355	0.010	1.195	0.967	0.005	0.000	0.000	0.002
	1	1.543	3.363	0.010	1.195	0.973	0.005	0.000	0.000	0.002
	0.96	1.543	3.377	0.011	1.202	0.973	0.006	0.000	0.001	0.002
	0.92	1.544	3.392	0.012	1.210	0.973	0.006	0.000	0.001	0.003

Table 8.4: The pressure dependence of the partial charges of Hg-1201 for different unit cell volumes. For comparison, the data for the experimental geometry are shown indicated by $V_{\rm ref}$.

The experimental spectra, however, show strong peaks at 592, 571 and 161 cm^{-1}, and a weaker one at 538 cm^{-1} in zz-polarization, which correspond to A_{1g} symmetry. In xz-polarization additional peaks at 76 cm^{-1} and 165 cm^{-1} are resolved and can be attributed to the two theoretically expected E_g phonon modes [21]. This work focuses on the A_{1g} vibrations. It is common to assign the 592 cm^{-1} peak to the A_{1g} vibration of the oxygen O2 and the 161 cm^{-1} peak to the vibration of the Ba atom. 161 cm^{-1} is a very big value for a A_{1g} Ba mode in a high-T_c cuprate superconductor. As a common value for the Ba frequency one would expect $\approx$ 120 cm^{-1}. A possible explanation for this high frequency may be found in the fact that in the Hg-1201 structure the two Ba atoms are only separated by one CuO_2 layer, while in most other cuprate superconductors they are separated by two or more layers. The presence of more than one CuO_2 layer is also reflected in the eigenvectors and eigenfrequencies of the normal modes. In a one-layer structure like Hg-1201 only oxygen and barium take part in the A_{1g} vibrations[2]. In a more-layer system, also the oxygen and the copper atoms of the other layers are involved in the normal vibrations, and their coupling to the Ba leads to a decrease of the frequency of the Ba dominated vibration. The calculated frequency of the Ba mode is determined to be 144 cm^{-1} (Table 8.5), where the difference to the experimental result is about 17 cm^{-1} which seems to be a quite big deviation. If it is considered, however, that the calculations have been made for zero temperature and without taking into account that the Ba position in the crystal is very sensitive to doping [83] the value is reasonable. (The measured peak at 571 cm^{-1} is an indication of excess oxygen.)

Concerning the two modes at 571 cm^{-1} and 538 cm^{-1}, various explanations have been proposed. It has to be recalled that at ambient pressure and room temperature the Hg-1201 crystal usually absorbs a certain amount of excess oxygen. This may result in two different effects. First, such an oxygen atom sitting at an interstitial site break the symmetry of the crystal. Vibrations around its equilibrium position therefore could be regarded as A_{1g} modes. Second, the presence of the excess oxygen changes charge density and lattice constants, which could also lead to a modulation of the frequency of the O2 mode. In reference [21] the peak at 571 cm^{-1} is assigned to a modulation of the A_{1g}-O2 mode by excess oxygen, while the 538 cm^{-1} peak is claimed to originate from a vibration of the excess oxygen itself.

The effect of doping on the A_{1g} modes will be discussed later. Here, the Raman spectra of the A_{1g} modes are presented for $\delta = 0$ and their dependence on pressure is studied. It turned out that the eigenvibrations remain uncoupled in the investigated pressure region up to8 GPa. In Table 8.5 the corresponding eigenfrequencies of the Ba and O2 modes are listed. In Figure 8.9 the Raman spectral density of the O2 mode is shown. Since the spectral density is dominated

[2]From the frozen-phonon calculations done in this thesis it turned out that they are nearly completely decoupled which could be expected due to the different masses of oxygen and barium.

by the derivative of $\epsilon^{zz}(\omega)$ with respect to the eigenvector Q, real and imaginary part of the (zz) component as a function of the laser energy are displayed in Figure 8.8 for different values of Q. The intensity of the barium vibration is

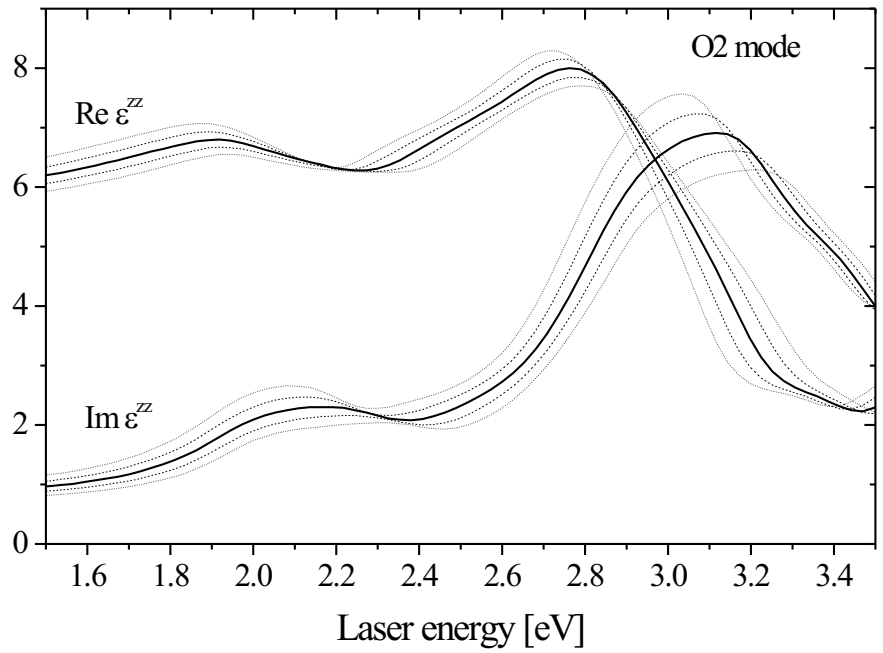

Figure 8.8: Real and imaginary part of the dielectric tensor component $\epsilon^{zz}(\omega)$ of Hg-1201 for V_{opt} with $|u_{O2}| \approx 0.0016\ c$ (dottet lines) and $|u_{O2}| \approx 0.0008\ c$ (dashed lines).

extremely small, such that its changes as a function of pressure could not be clearly resolved numerically.

The pressure dependence of the calculated Raman intensities at a laser energy of 2.4 eV using a Lorentzian broadening of $\Gamma = 25K$ is presented in Figure 8.9. The Raman intensity decreases while the peak is shifted to higher frequencies. In addition, Figure 8.10 shows the resonance behavior of the O2 mode, i.e. the integrated Raman intensities, again as a function of applied pressure. Figure 8.10 clearly demonstrates that the increase or decrease of the intensity sensitively depends on the used laser frequency. An experimental crosscheck of this finding would be highly desirable.

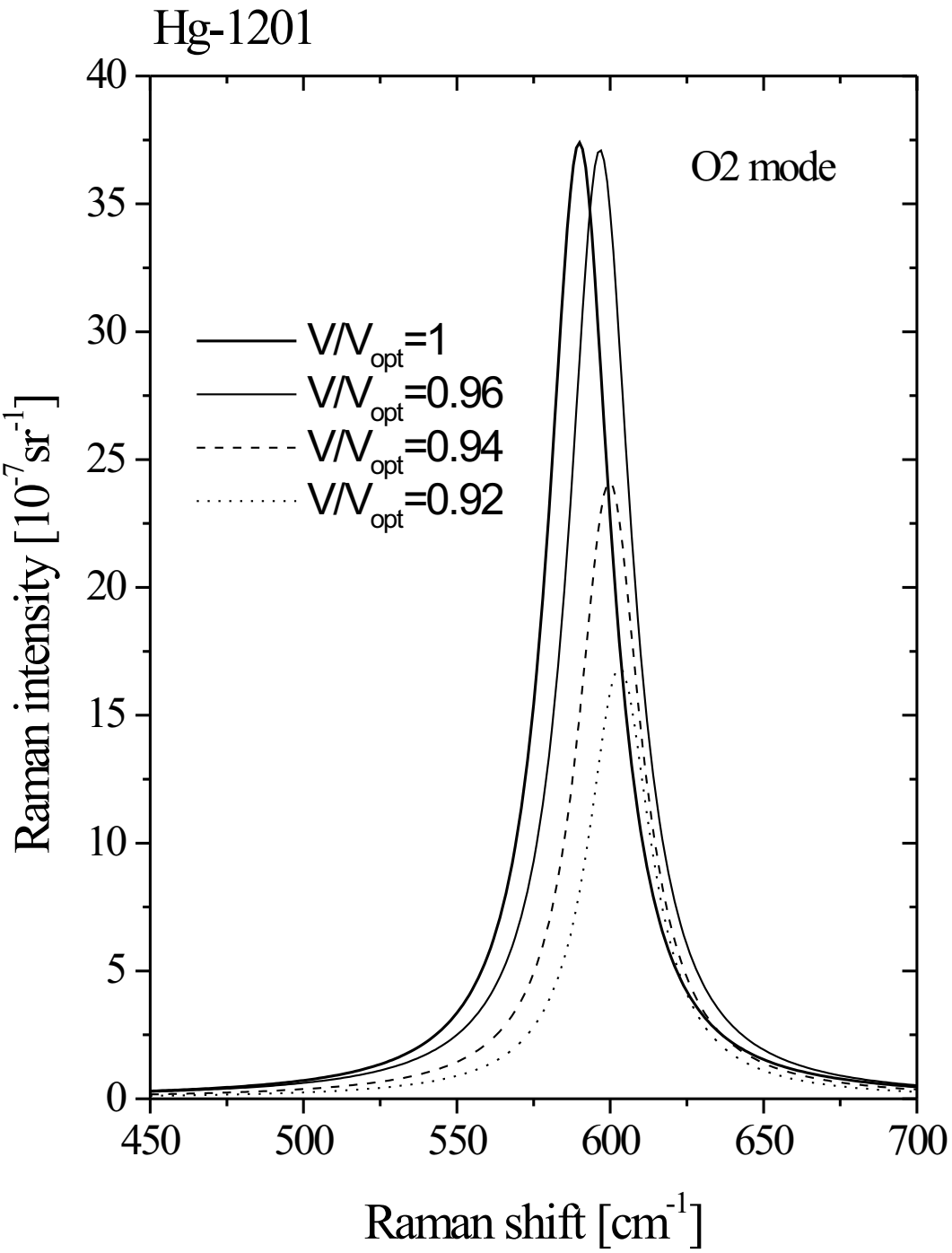

Figure 8.9: Raman spectra of the O2 mode in Hg-1201 as a function of the unit cell volume with $\Gamma = 25K$ at the laser energy of 2.4 eV for all curves.

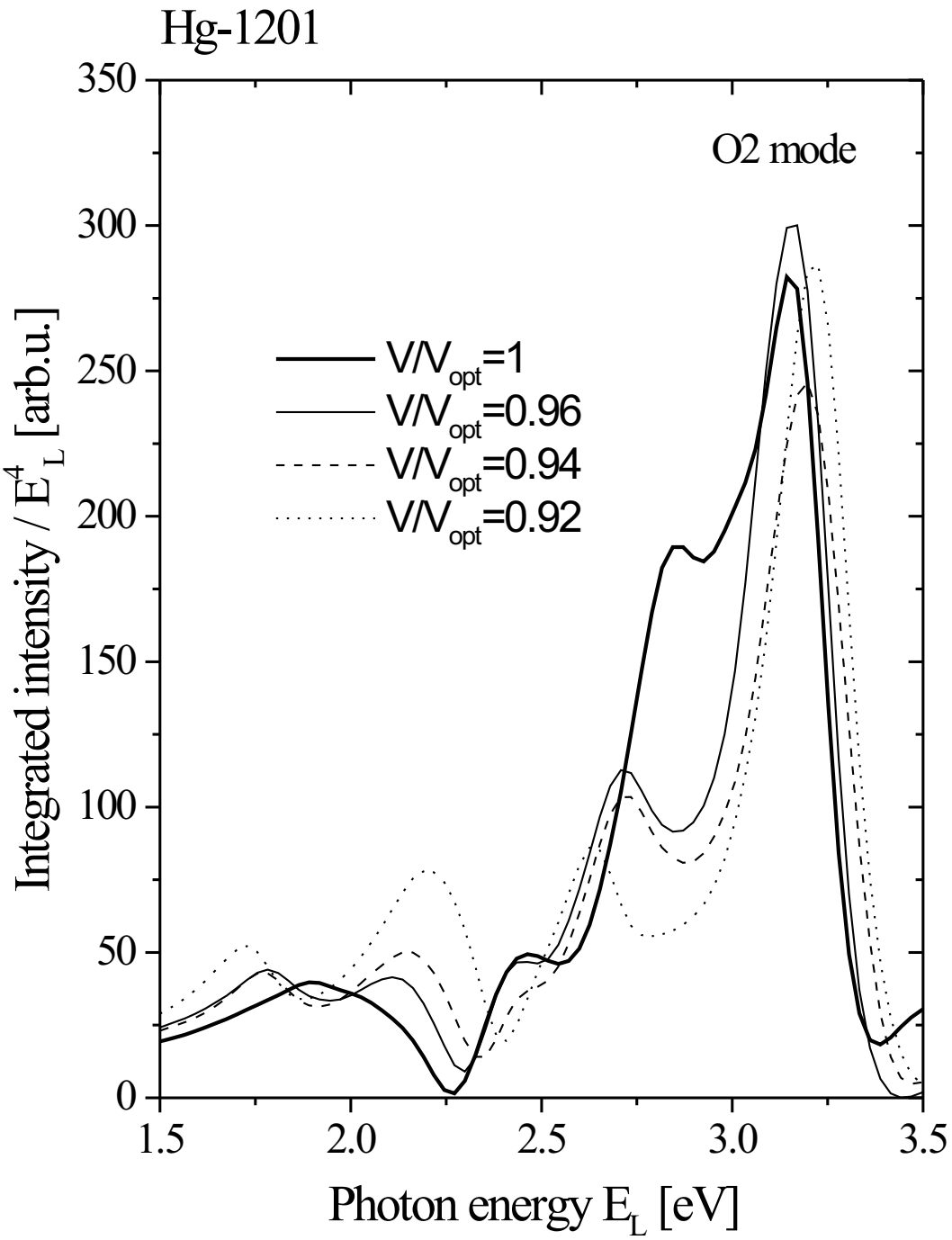

Figure 8.10: The resonance behavior of the integrated Raman intensities as a function of the unit cell volume.

$V/V_{\rm opt}$	P	ω_{O2}	ω_{Ba}
	[GPa]	$[cm^{-1}]$	$[cm^{-1}]$
1.00	0.21	590	144
0.96	3.74	597	144
0.94	5.50	599	147
0.92	7.27	603	152

Table 8.5: Phonon frequencies of the A_{1g} modes in Hg-1201 as a function of pressure.

8.3 Hg-1212

8.3.1 The Optimization of the Lattice Parameters and their Pressure Dependence.

The structural parameters as the starting point for the geometry optimization of Hg-1212 have been taken from Reference [84]. Therein, the data have been obtained by neutron powder diffraction on Argon reduced samples, which also contained a 30% fraction of Hg-1201. The authors claim, however, that this fact did not have much influence on the obtained structural data. Furthermore it is reported that in these samples the Hg and the interstitial oxygen sites had occupation factors of 0.96 and 0.008, respectively.

Compared to the experimental reference data, the optimization procedure leads to a 1.3% smaller volume and a c/a-ratio which is $\approx$ 3% bigger (see Table 8.6). Moreover, larger values for the calculated Hg-Ba, Hg-Cu, Hg-O1 distances and a smaller Hg-O2 distance is observed. Considering the pressure dependence of the lattice parameters it can be seen (Table 8.6) that with decreasing volume also the c/a-ratios are shrinking. This reduction of the c/a-ratio can be attributed to decreasing distances of all the layers similar in magnitude, with the only exception being the distance between Hg and the apical oxygen O2 which decreases only slightly. A significant difference between Hg-1201 and Hg-1212 is also displayed in Table 8.6: The CuO_2 layers are not planar any more.

8.3.2 The Pressure Dependence of the Band structure, the Density of States, and the Partial Charges

The band structure of Hg-1212 (see Figure 8.11) has also a very significant two dimensional character. The differences to the band structure of the Hg-1201 compound are the following: There are now two bands attributed to the CuO_2 layers, which are crossing the Fermi level. Another striking fact is that the Hg-O2 derived band significantly intersects E_F at $V = V_{\mathrm{opt}}$, which means hole doping of the two Cu1-O1 bands even at pressures close to zero. As can be expected from the findings for the single-layer compound, this effect can be increased by applying pressure (Figure 8.12). At the same time also the van Hove singularity at the X point moves closer to the Fermi level as a function of pressure.

Figure 8.13 shows the total and the partial densities of states of Hg-1212. Again, like in Hg-1201, a nearly constant and very small Cu1-O1 DOS dominates at E_F. Furthermore, in addition to this covalent bonds of Cu1 and O1 with peaks at $\approx$ -1 eV some small covalent bonding between the CuO_2 unit and the Ca1 atom arises in the whole valence band region. Some covalent character is made out between Hg and O2 around -8 eV, between Ba, O1 and Ca below -12 eV. The changes of the density of states with pressure (Figure 8.14) is nearly

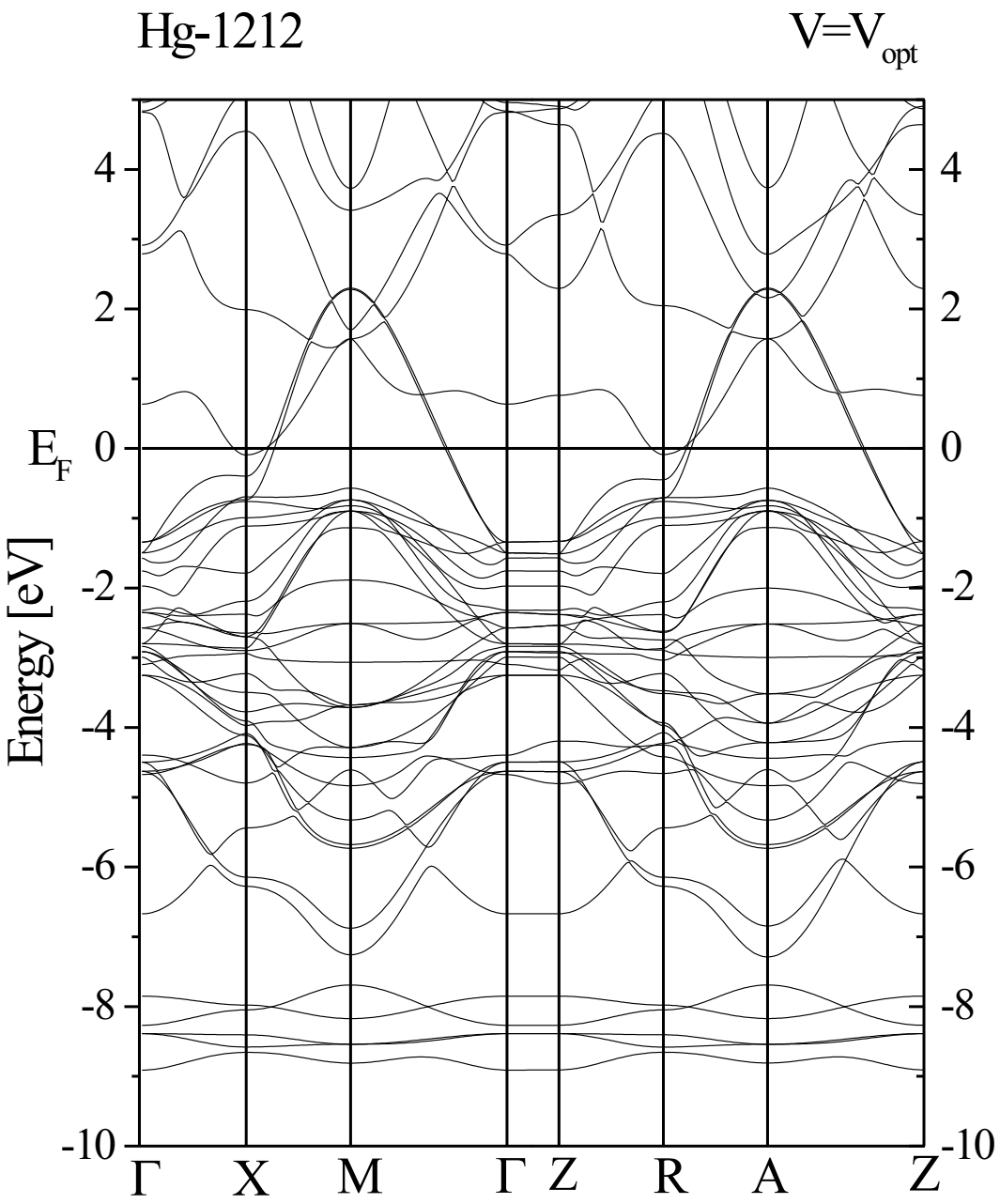

Figure 8.11: The band structure of Hg-1212 for the equilibrium volume V_{opt}.

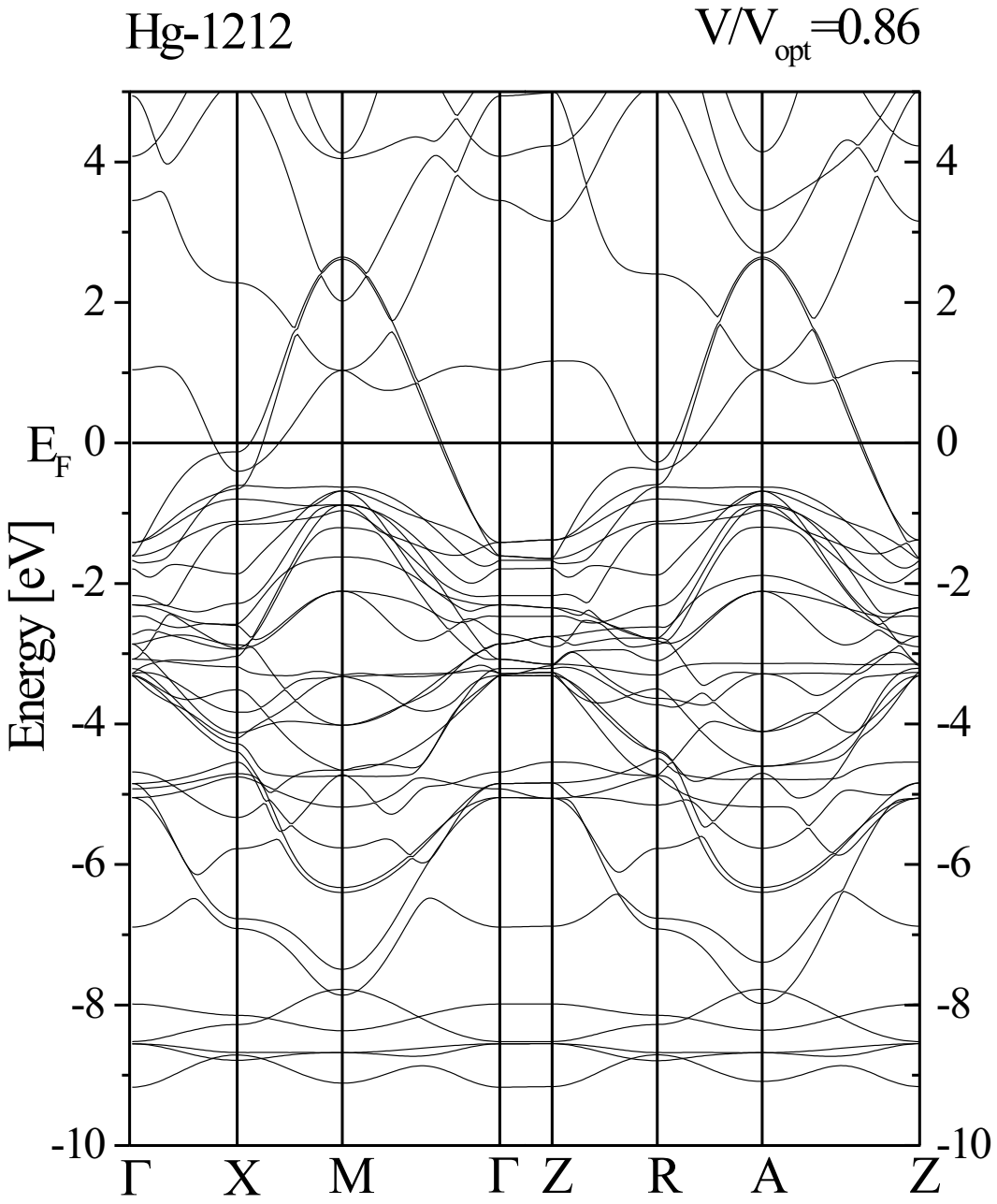

Figure 8.12: The band structure of Hg-1212 for $V/V_{\rm opt} = 0.86$.

	V_{ref}	V_{opt}	0.96 V_{opt}	0.91 V_{opt}	0.86 V_{opt}
a [a.u.]	7.300	7.204	7.153	7.072	6.986
$\Delta a/a_{\mathrm{opt}}$ [%]	1.3	0.000	-0.7	-1.8	-3.0
c [a.u.]	23.995	24.391	23.746	23.013	22.273
$\Delta c/c_{\mathrm{opt}}$ [%]	-1.6	0.000	-2.6	-5.7	-8.7
(c/a)	3.287	3.386	3.320	3.254	3.188
$\Delta(c/a)/(c/a)_{\mathrm{opt}}$ [%]	-2.9	0.000	-1.9	-3.9	-5.8
V [a.u.^{3}]	1278.694	1265.835	1214.974	1150.953	1087.016
$\Delta V/V_{\mathrm{opt}}$ [%]	1.0	0.0	-4.0	-9.0	-14.1
P [GPa]		-0.576	4.314	10.427	16.540
z_{Ba}[a.u.]	5.383	5.577	5.339	5.050	4.775
z_{Cu1}[a.u.]	9.052	9.532	9.259	8.931	8.601
z_{O1}[a.u.]	9.035	9.325	9.057	8.737	8.421
z_{O2}[a.u.]	3.715	3.700	3.686	3.670	3.655
$d_{z[\mathrm{Cu1\text{-}Cu1'}]}$	5.891	5.327	5.228	5.151	5.0253
$d_{z[\mathrm{Cu1\text{-}O1}]}$	0.017	0.207	0.202	0.194	0.180
$d_{z[\mathrm{Cu1\text{-}Ba}]}$	3.669	3.955	3.92	3.881	3.826
$d_{z[\mathrm{Cu1\text{-}O2}]}$	5.337	5.832	5.573	5.261	4.946

Table 8.6: The structural parameters of Hg-1212 as function of the unit cell volume.

negligible, except the small effect that some states of O2 and Hg become occupied.

Finally also the changes in the partial charges as a function of pressure are shown in Table 8.7. For comparison, the corresponding values for the reference geometry are depicted indicated by V_{ref}. Generally, it can be stated that the behavior is similar as for the Hg-1201 compound.

8.3.3 The Raman Spectra and their Pressure Dependence

In the following, phonon frequencies and Raman spectra of Hg-1212 as a function of pressure will be discussed. The frozen-phonon atomic-force calculations have yield the eigenmodes presented in Table 8.8 which all increase in frequency with applied pressure. The first eigenvibration, the highest in frequency, can be identified as a nearly decoupled vibration of the apical oxygen O2. The second vibration turned out to be dominated by O1 with a little admixture of Cu1, Ba, and O2. The third vibration can be attributed to a coupled out-of-phase vibration of Cu1 and Ba, while the fourth vibration is an in-phase vibration of these two atoms. When applying pressure, the eigenvectors exhibit changes in the relative amplitudes, but the character of each vibration remains unchanged. The most significant effect is a decrease (increase) of the Ba (Cu1) component in the eigenvector of the out-of-phase mode, whereas it is the other way round in the

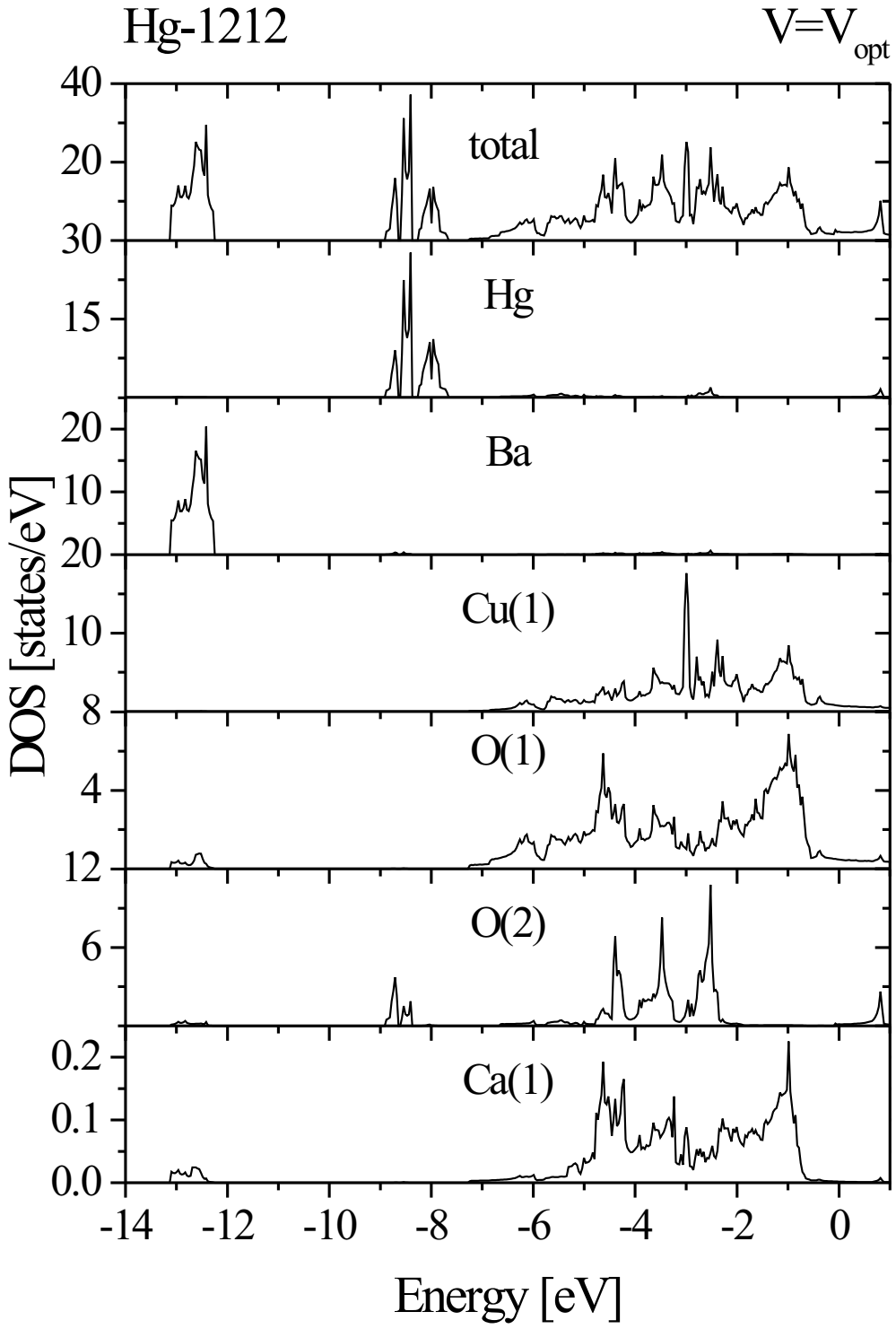

Figure 8.13: The total DOS and the site-projected densities of states of Hg-1212 for $V = V_{\text{opt}}$.

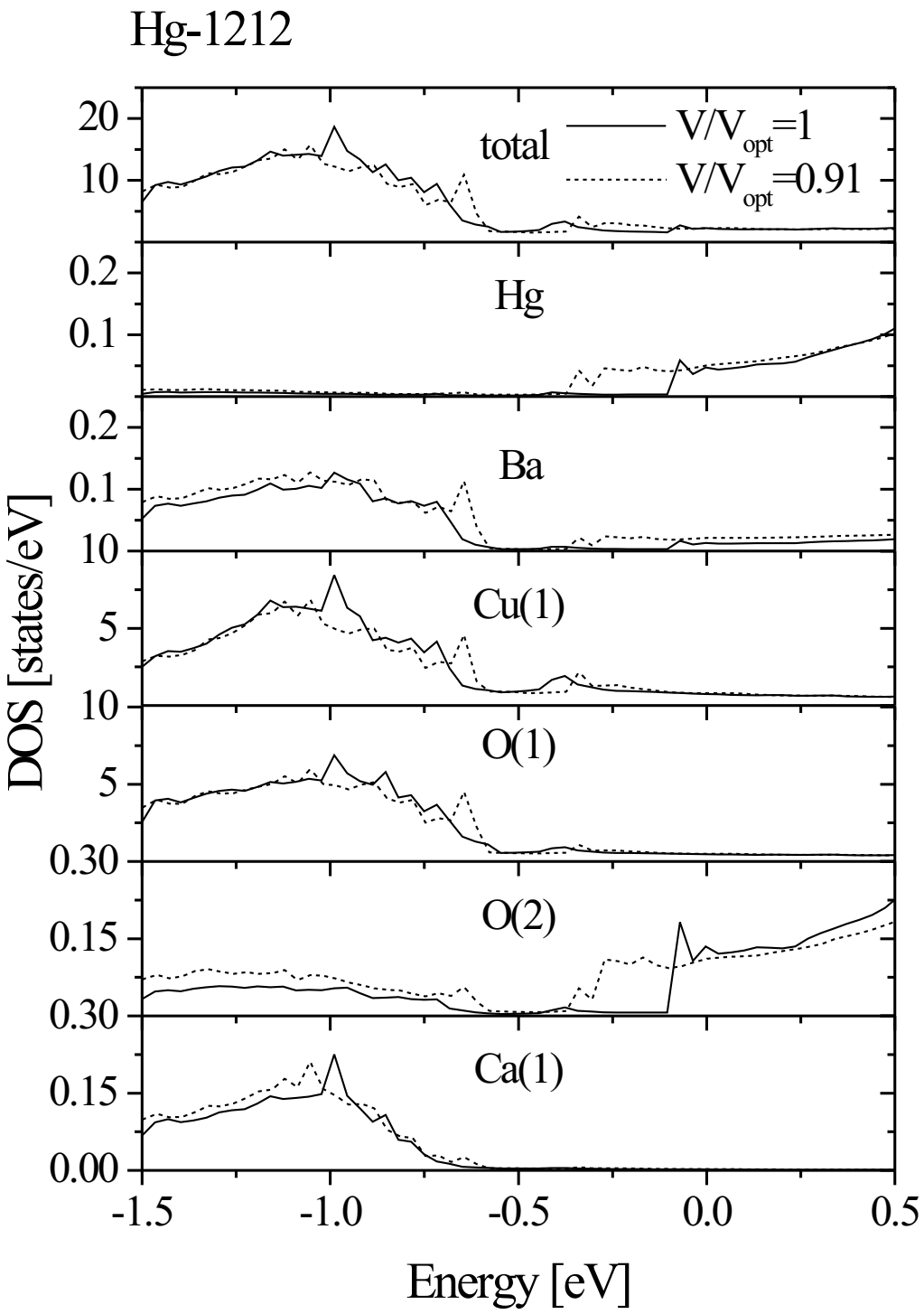

Figure 8.14: The total and partial densities of states of Hg-1212 at the Fermi level for different volumes.

	$V/V_{\rm opt}$	s	p	d	p_x	p_z	d_{z^2}	$d_{x^2-y^2}$	d_{xy}	d_{xz}
Hg	$V_{\rm ref}$	0.392	6.041	8.048	1.993	2.055	1.445	1.632	1.629	1.672
	1	0.390	6.042	8.048	1.993	2.056	1.439	1.633	1.630	1.673
	0.96	0.391	6.049	8.043	1.996	2.058	1.438	1.632	1.628	1.673
	0.91	0.393	6.057	8.035	1.998	2.060	1.438	1.630	1.626	1.671
	0.86	0.396	6.065	8.029	2.001	2.063	1.440	1.627	1.625	1.669
Ba	$V_{\rm ref}$	1.737	4.281	10.004	1.430	1.421	2.000	2.000	2.001	2.002
	1	1.737	4.281	10.003	1.428	1.425	2.000	2.000	2.001	2.002
	0.96	1.738	4.284	10.004	1.431	1.423	2.000	2.000	2.001	2.002
	0.91	1.739	4.290	10.006	1.435	1.421	2.001	2.000	2.002	2.002
	0.86	1.741	4.296	10.009	1.439	1.419	2.001	2.001	2.003	2.002
Cu1	$V_{\rm ref}$	0.221	6.157	8.694	2.069	2.019	1.737	1.435	1.857	1.833
	1	0.230	6.172	8.688	2.074	2.023	1.729	1.442	1.858	1.829
	0.96	0.233	6.180	8.682	2.078	2.025	1.733	1.430	1.859	1.830
	0.91	0.239	6.193	8.683	2.084	2.027	1.738	1.422	1.861	1.832
	0.86	0.245	6.209	8.682	2.090	2.030	1.741	1.411	1.862	1.834
O1	$V_{\rm ref}$	1.530	3.427	0.010	1.116	1.195	0.001	0.003	0.003	0.002
	1	1.530	3.439	0.011	1.124	1.192	0.002	0.003	0.003	0.002
	0.96	1.530	3.451	0.012	1.126	1.199	0.002	0.003	0.003	0.002
	0.91	1.530	3.471	0.013	1.132	1.208	0.002	0.004	0.003	0.002
	0.86	1.530	3.493	0.015	1.138	1.218	0.002	0.004	0.004	0.003
O2	$V_{\rm ref}$	1.544	3.363	0.010	1.198	0.967	0.005	0.000	0.000	0.002
	1	1.541	3.372	0.010	1.198	0.976	0.005	0.000	0.000	0.002
	0.96	1.542	3.388	0.011	1.206	0.976	0.005	0.000	0.001	0.003
	0.91	1.543	3.408	0.012	1.217	0.975	0.006	0.000	0.001	0.003
	0.86	1.545	3.430	0.014	1.229	0.973	0.006	0.000	0.001	0.003
Ca1	$V_{\rm ref}$	1.938	5.483	0.169	1.827	1.830	0.015	0.043	0.014	0.058
	1	1.940	5.487	0.189	1.828	1.831	0.017	0.048	0.019	0.053
	0.96	1.941	5.490	0.200	1.830	1.832	0.018	0.051	0.020	0.056
	0.91	1.943	5.494	0.214	1.831	1.833	0.020	0.055	0.021	0.059
	0.86	1.945	5.499	0.231	1.832	1.835	0.021	0.060	0.023	0.063

Table 8.7: The partial charges of Hg-1212 as a function of the unit cell volume. For comparison, the values for the experimental geometry are given indicated by V_{ref}.

in-phase mode of Ba and Cu1. Figure 8.15 shows the real and imaginary part of

V/V_{opt}	ω_{ph} [cm^{-1}]	Ba	Cu1	O1	O2
1	594.8	-0.01	-0.02	0.12	-0.99
0.96	602.7	-0.01	-0.02	0.11	-0.99
0.91	618.6	-0.01	-0.02	0.11	-0.99
0.86	623.2	-0.01	-0.03	0.15	-0.99
1	382.1	-0.15	-0.15	0.97	0.12
0.96	391.2	-0.15	-0.08	0.98	0.12
0.91	409.5	-0.15	-0.08	0.98	0.12
0.86	426.4	-0.18	-0.05	0.97	0.15
1	147.1	0.67	-0.74	-0.02	0.01
0.96	145.0	0.63	-0.77	0.03	0.01
0.91	163.2	0.49	-0.87	0.00	0.02
0.86	166.0	0.59	-0.81	0.07	0.03
1	80.8	0.73	0.65	0.21	0.01
0.96	103.4	0.76	0.63	0.17	0.00
0.91	119.2	0.86	0.49	0.17	0.00
0.86	127.8	0.79	0.59	0.18	0.00

Table 8.8: The eigenvectors and the eigenfrequencies of Hg-1212 as a function of the relative unit cell volume.

the dielectric tensor component $\epsilon^{zz}(\omega)$ for several displacements and two different volumes. The picture should give the reader a feeling about the magnitude of changes during the vibration. By that also the uncertainties in the calculation of the first derivatives of the dielectric function can be estimated. The Raman intensity of the O2 mode, depicted in Figure 8.16, shows that contrary to the Hg-1201 compound, the intensity increases with applied pressure. This fact is also displayed in Figure 8.17 which shows the resonance behavior of the integrated Raman intensity of the O2 peak. The giant integrated Raman intensity at V/V_{opt}=0.91 result from the relatively big changes in the calculated dielectric function for that volume and may need a quite big error bar. Furthermore it should be pointed out again that the increasing or decreasing of the Raman intensity with pressure depends on the laser energy (see Figure 8.17) and that there may be an uncertainty in the displayed resonance curve of 0.2 eV with respect to the laser frequency.

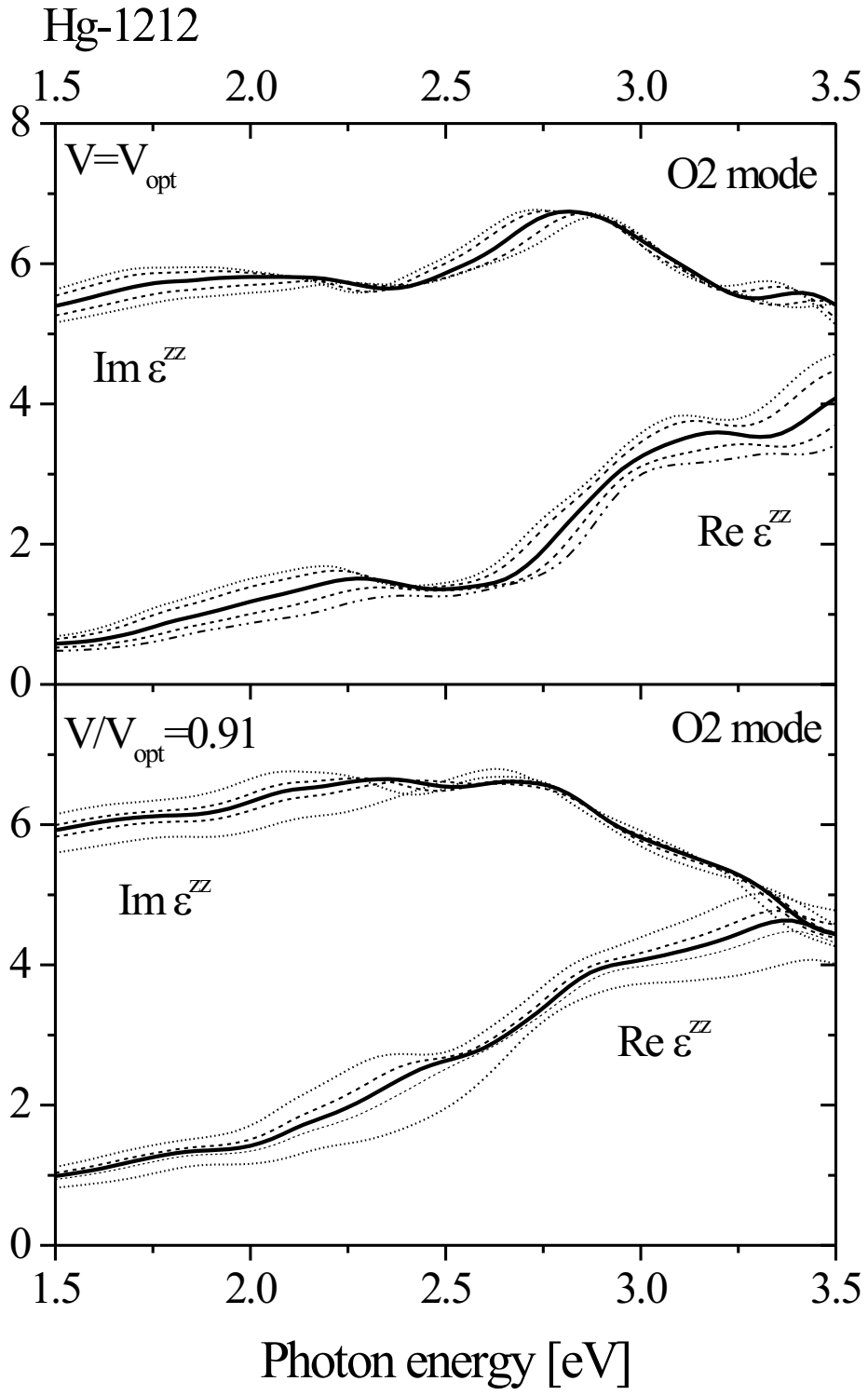

Figure 8.15: Real and imaginary part of the dielectric tensor component ϵ^{zz} of Hg-1212 for several displacements and two different unit cell volumes.

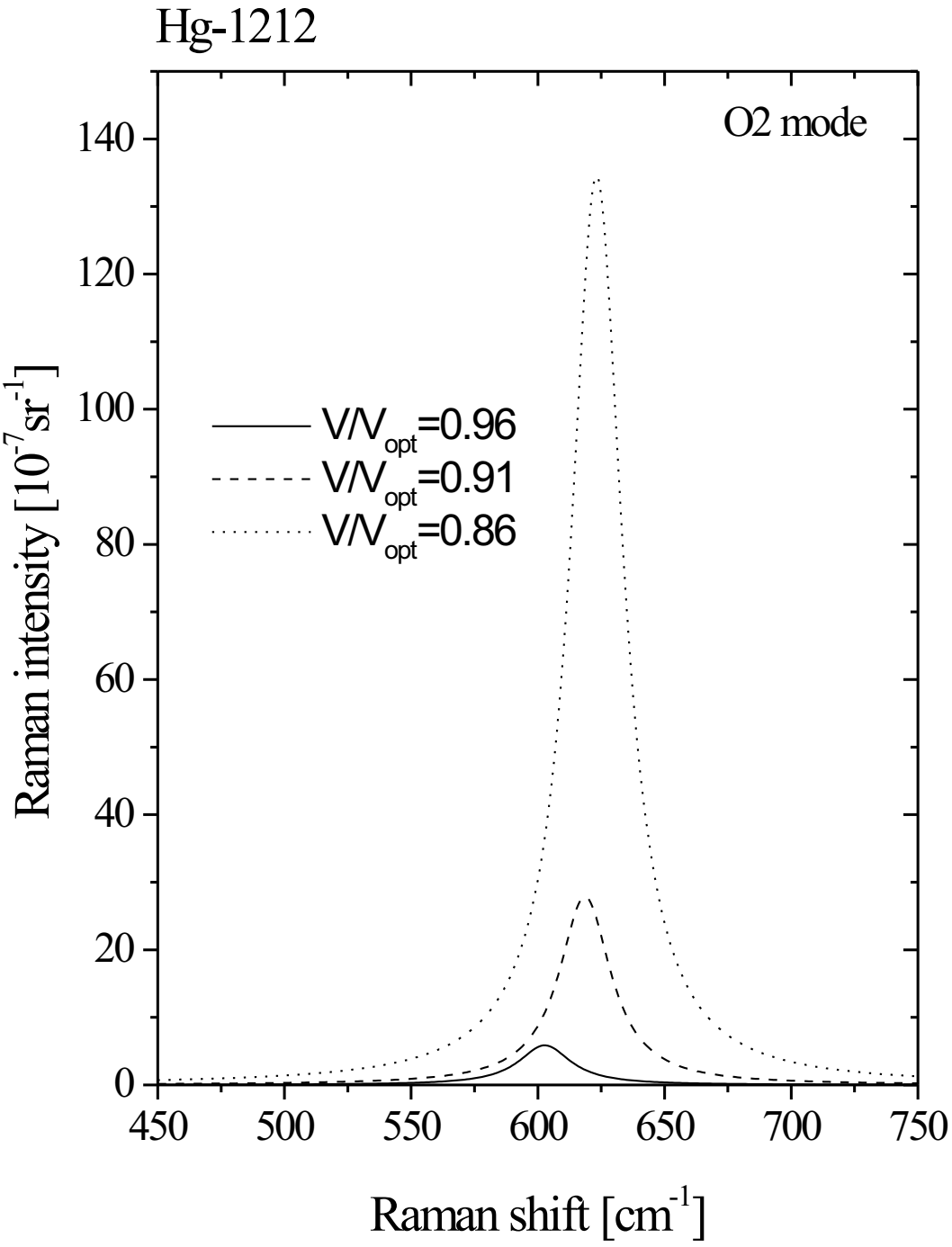

Figure 8.16: The Raman intensity of Hg-1212 with $\Gamma = 25K$ at a laser energy of 2.4 eV.

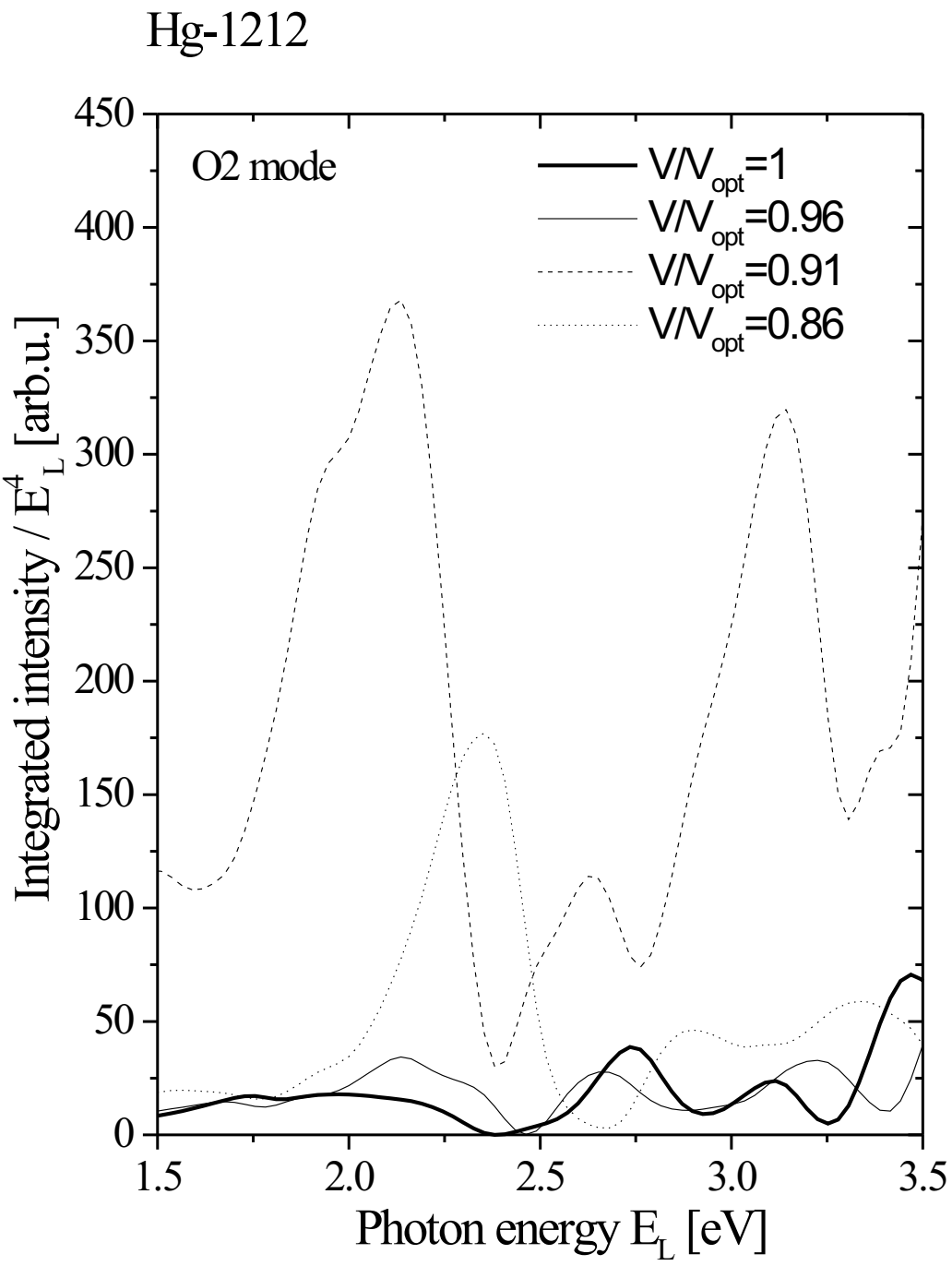

Figure 8.17: The resonance behavior of the integrated Raman intensity of the O2 mode in Hg-1212.

	V_{ref}	V_{opt}	$0.97 * V_{\mathrm{opt}}$	$0.92 * V_{\mathrm{opt}}$	$0.87 * V_{\mathrm{opt}}$
a[a.u.]	7.291	7.194	7.143	7.111	7.001
$\Delta a/a_{\mathrm{opt}}$[%]	1.3	0.0	-0.7	-1.2	-2.7
c[a.u.]	29.933	30.127	29.622	28.319	27.594
$\Delta c/c_{\mathrm{opt}}$[%]	-0.6	0.0	-1.7	-6.0	-8.4
c/a	4.106	4.188	4.147	3.983	3.942
$\Delta(c/a)/(c/a)_{\mathrm{opt}}$[%]	-2.0	0.0	-1.0	-4.9	-5.9
V[a.u.^{3}]	1591.027	1559.201	1511.471	1431.920	1352.369
$\Delta V/V_{\mathrm{opt}}$[%]	2.0	0.0	-3.1	-8.2	-13.3
P[GPa]		0.422	4.361	10.926	17.491
z_{Ba}[a.u.]	5.220	5.521	5.365	4.958	4.718
z_{Cu1}[a.u.]	8.953	9.512	9.332	8.848	8.563
z_{O1}[a.u.]	8.989	9.324	9.142	8.660	8.386
z_{O2}[a.u.]	3.831	3.699	3.691	3.668	3.653
z_{Ca1}[a.u.]	11.898	12.132	11.915	11.343	11.023
$d_{z[\mathrm{Cu1\text{-}Cu2}]}$[a.u.]	6.0135	5.5515	5.479	5.3115	5.234
$d_{z[\mathrm{Cu1\text{-}Ca1}]}$[a.u.]	2.945	2.62	2.583	2.495	2.46
$d_{z[\mathrm{Cu1\text{-}O1}]}$[a.u.]	0.036	0.188	0.19	0.188	0.177
$d_{z[\mathrm{Cu1\text{-}Ba}]}$[a.u.]	3.733	3.991	3.967	3.89	3.845
$d_{z[\mathrm{Cu1\text{-}O2}]}$[a.u.]	5.122	5.813	5.641	5.18	4.91

Table 8.9: The structural data of Hg-1223 as a function of the unit cell volume.

8.4 Hg-1223

8.4.1 The Optimization of the Lattice Parameters

The structural parameters as the starting point for the geometry optimization in Hg-1223 have been taken from Reference [85]. These data have been obtained from X-ray diffraction studies on Hg-1223 crystals with a stoichiometry of $Hg_{0.92}Cu_{0.08}Ba_2Ca_2Cu_3O_{8.11}$, where the Hg sites are partly replaced by cooper and the small amount of interstitial oxygen is situated at (1/2,1/2,0). It turned out that the calculated volume is 2% smaller than the experimental one, whereas the c/a-ratio is 2% larger. Additionally, there are some deviations in the bond lengths (see Table 8.9): The distances between the Cu-layers are obtained shorter than in experiment, while the distances from the Cu-layers to the planes of the other atoms are bigger.

8.4.2 The Pressure Dependence of the Band Structure, Density of States, and Partial Charges

Like for the previously discussed members of the Hg-family the band structure of Hg-1223 also exhibits a two dimensional character (Figure 8.18). The important

characteristics of the band structure remain the same as in Hg-1201 and Hg-1212. The only principle difference is that there are now three CuO_2 bands intersecting the Fermi level. They are hole doped through the existence of the Hg-O2 derived band which shifts E_F down compared to the single-layer compound. The pressure dependence of the band structure is very similar to that of the Hg-1212 system (see Figures 8.18 and 8.19) as well as the DOS (Figures 8.20 and 8.21). As already discussed in the previous sections for Hg-1201 and Hg1212, also in the case of Hg-1223 the partial charges generally increase with applied pressure (Table 8.10).

8.4.3 The Raman Spectra and their Pressure Dependence

The phonon frequencies and Raman spectra of Hg-1223 as a function of pressure are presented in this section. The frozen-phonon atomic-force calculations have yield the eigenmodes and eigenvectors presented in Table 8.11 which show generally the trend of increasing frequencies with applied pressure. The first eigenvibration, the highest one in frequency, can be identified as a nearly decoupled vibration of the apical oxygen O2. The second mode turned out to be mainly dominated by an out-of-phase vibration of O1 and Ca1 (with a larger O1 component) and some admixture of Cu1, Ba, and O2. The third vibration can be attributed to an in-phase vibration of O1 and Ca1, with Ca1 dominating the mode. There is also a pronounced admixture of Ba and a smaller Cu1 contribution. The fourth vibration and the fifth vibration are identified as being mainly dominated by Ba and Cu1 out-of- and in-phase vibrations, respectively, with a little admixture of O1 in the latter one, like it has also been the case in Hg-1212. In Table 8.11 the calculated results are compared to experimental data and assigned to their supposed experimental counterparts. It can be seen that there are quite big differences between theoretical and experimental results and among the experimental data as well. The deviations might have a general explanation by the different amount of excess oxygen. The biggest discrepancy between theory and experiment is observed for the 368.9 cm^{-1} mode. There is a peak at 400 cm^{-1} given in Reference [88], which is, however claimed to originate from a defect-induced mode and can therefore not be clearly assigned to the calculated O1 vibration. On the other hand, the 477 cm^{-1} peak measured in Reference [87] is claimed to be the A_{1g} O1 mode. Summarizing it can be said that the O1 dominated vibration exhibits a significant discrepancy between theory and experiment, which should be investigated more in detail.

8.4.4 The Raman Spectra and their Pressure Dependence

Figure 8.22 shows the real and imaginary part of the dielectric tensor component $\epsilon^{zz}(\omega)$ for several displacements and two different volumes. The picture should again give the reader a feeling about the magnitude of changes during the vibra-

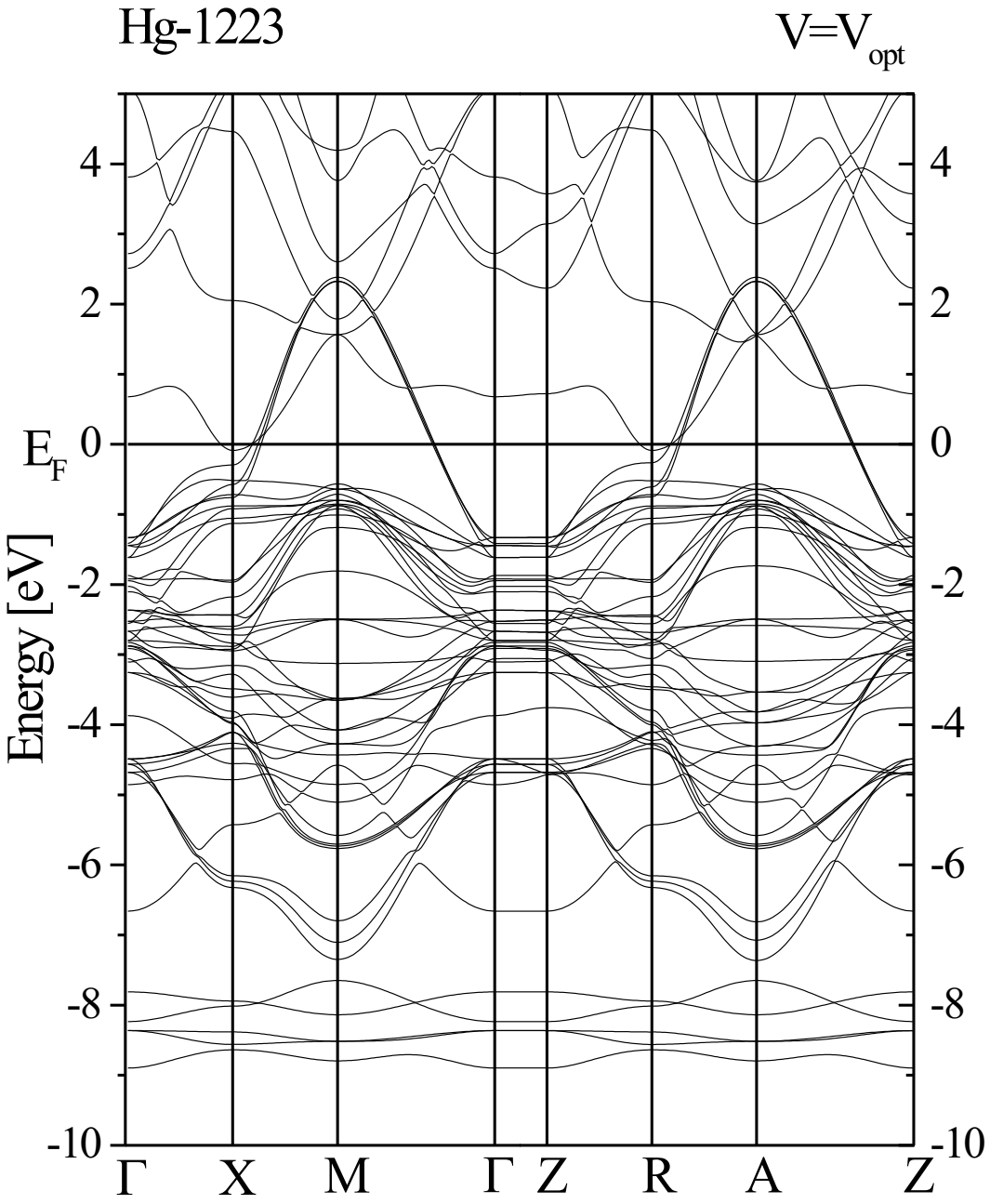

Figure 8.18: The electronic band structure of Hg-1223 at $V = V_{\mathrm{opt}}$.

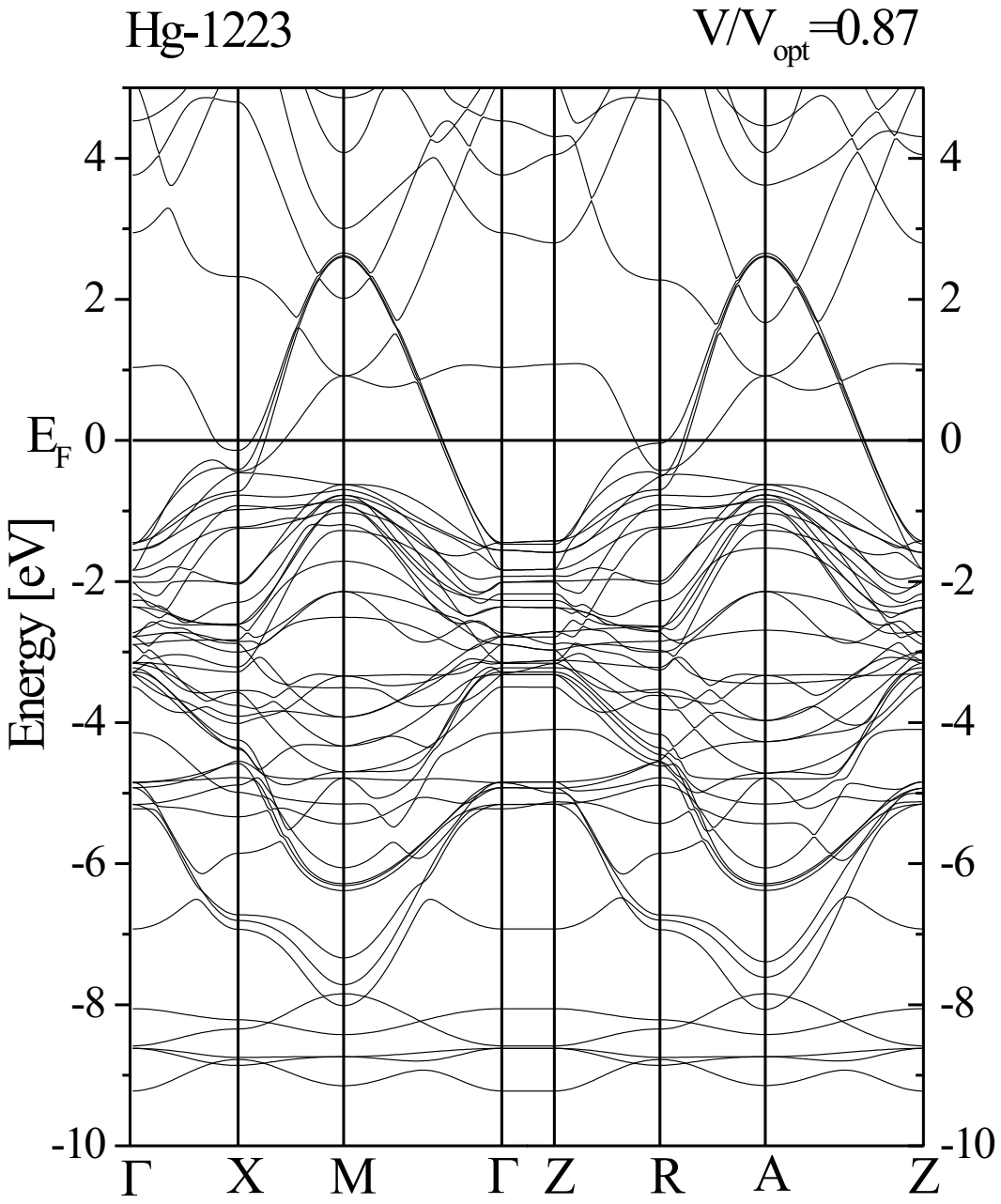

Figure 8.19: The electronic band structure of Hg-1223 at $V/V_{\rm opt}$=0.87.

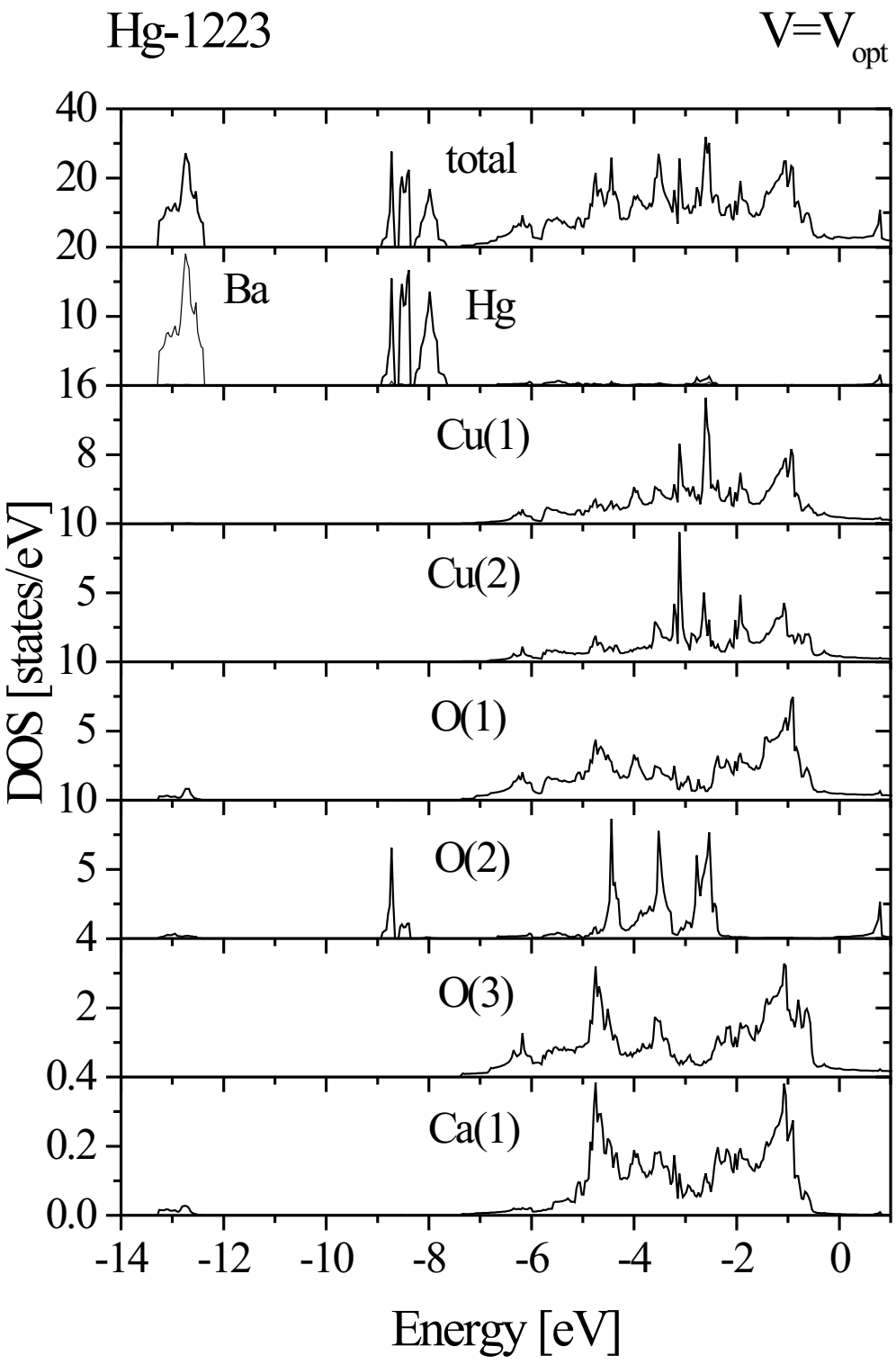

Figure 8.20: The total and partial densities of states of Hg-1223 at $V = V_{\mathrm{opt}}$.

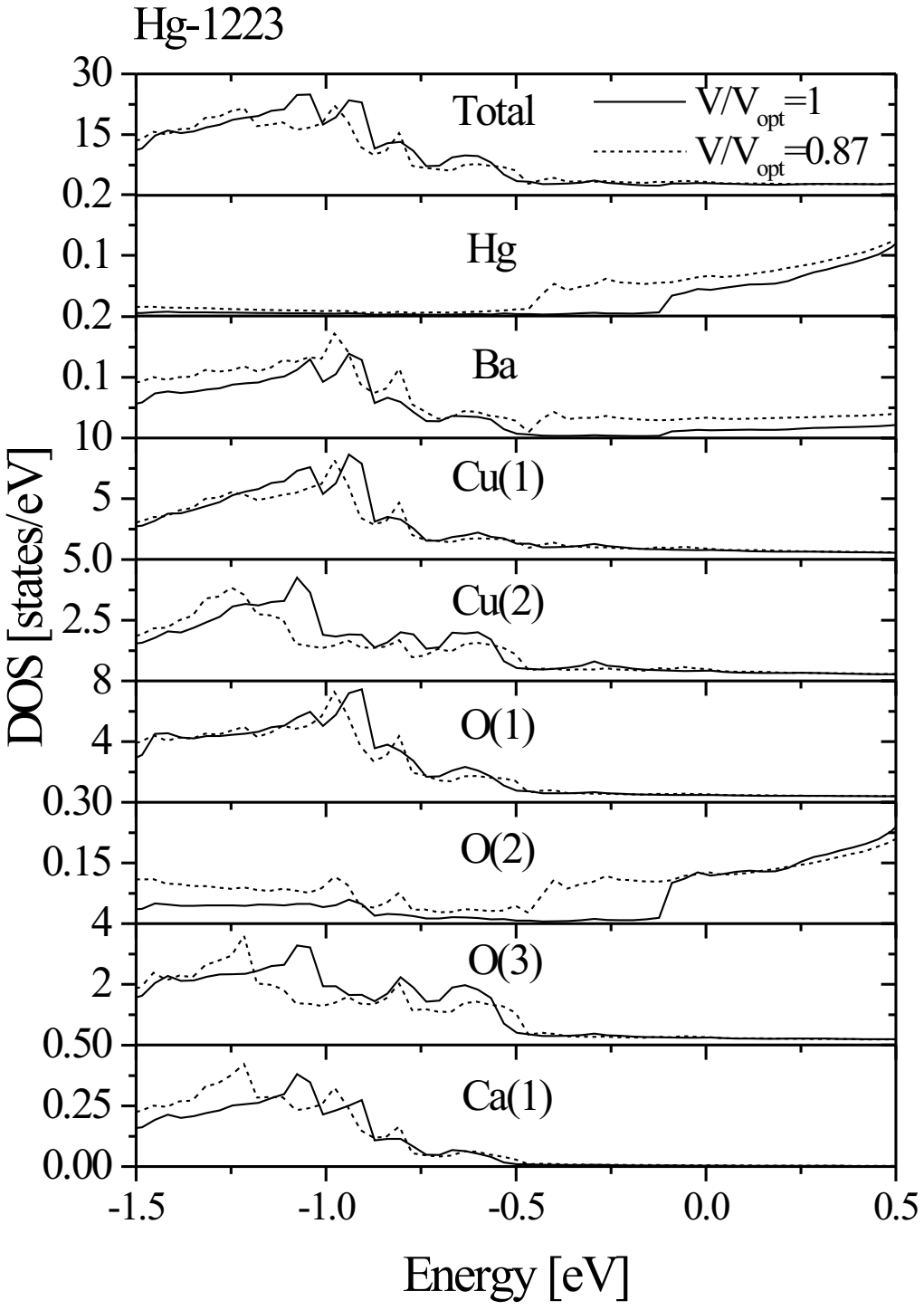

Figure 8.21: The total and partial densities of states of Hg-1223 for two different unit cell volumes.

	$V/V_{\rm opt}$	s	p	d	p_x	p_z	d_{z^2}	$d_{x^2-y^2}$	d_{xy}	d_{xz}
Hg	V_{ref}	0.383	6.030	8.057	1.993	2.044	1.471	1.630	1.627	1.664
	1	0.389	6.043	8.046	1.994	2.056	1.438	1.633	1.629	1.673
	0.97	0.389	6.048	8.042	1.995	2.057	1.438	1.632	1.628	1.672
	0.92	0.394	6.058	8.032	1.999	2.061	1.438	1.629	1.626	1.671
	0.87	0.397	6.070	8.027	2.004	2.064	1.441	1.626	1.624	1.668
Ba	V_{ref}	1.800	4.556	10.009	1.523	1.510	2.001	2.001	2.002	2.003
	1	1.799	4.555	10.008	1.520	1.516	2.001	2.001	2.002	2.003
	0.97	1.800	4.558	10.009	1.522	1.515	2.001	2.001	2.002	2.003
	0.92	1.802	4.563	10.012	1.526	1.511	2.002	2.001	2.003	2.003
	0.87	1.805	4.571	10.015	1.531	1.511	2.002	2.002	2.004	2.004
Cu1	V_{ref}	0.220	6.158	8.689	2.070	2.019	1.736	1.428	1.857	1.834
	1	0.230	6.172	8.695	2.075	2.022	1.732	1.444	1.858	1.831
	0.97	0.234	6.180	8.691	2.079	2.023	1.734	1.437	1.859	1.831
	0.92	0.235	6.187	8.695	2.081	2.025	1.741	1.431	1.859	1.832
	0.87	0.243	6.206	8.683	2.089	2.028	1.741	1.415	1.861	1.834
Cu2	V_{ref}	0.219	6.157	8.683	2.069	2.020	1.731	1.422	1.859	1.836
	1	0.228	6.174	8.687	2.076	2.024	1.723	1.436	1.859	1.835
	0.97	0.232	6.182	8.681	2.078	2.026	1.723	1.429	1.860	1.834
	0.92	0.235	6.189	8.674	2.081	2.028	1.724	1.421	1.860	1.835
	0.87	0.244	6.209	8.668	2.089	2.031	1.723	1.413	1.862	1.835
O1	V_{ref}	1.530	3.426	0.010	1.115	1.195	0.001	0.003	0.003	0.002
	1	1.530	3.446	0.011	1.126	1.195	0.002	0.003	0.003	0.002
	0.97	1.530	3.457	0.012	1.129	1.200	0.002	0.003	0.003	0.002
	0.92	1.530	3.473	0.013	1.130	1.213	0.002	0.004	0.003	0.002
	0.87	1.530	3.496	0.015	1.138	1.221	0.002	0.004	0.004	0.003
O2	V_{ref}	1.547	3.353	0.009	1.207	0.938	0.004	0.000	0.001	0.002
	1	1.540	3.378	0.010	1.201	0.976	0.005	0.000	0.000	0.002
	0.97	1.541	3.391	0.011	1.208	0.976	0.005	0.000	0.001	0.003
	0.92	1.544	3.410	0.012	1.219	0.973	0.006	0.000	0.001	0.003
	0.87	1.546	3.438	0.014	1.233	0.972	0.006	0.000	0.001	0.003
O3	V_{ref}	1.531	3.406	0.010	1.110	1.186	0.001	0.003	0.003	0.001
	1	1.531	3.437	0.011	1.120	1.197	0.002	0.003	0.003	0.002
	0.97	1.531	3.448	0.012	1.124	1.201	0.002	0.004	0.003	0.002
	0.92	1.530	3.461	0.013	1.125	1.212	0.002	0.004	0.003	0.002
	0.87	1.530	3.485	0.015	1.134	1.218	0.002	0.004	0.004	0.003
Ca1	V_{ref}	1.938	5.482	0.167	1.826	1.830	0.016	0.043	0.014	0.047
	1	1.940	5.487	0.189	1.828	1.831	0.018	0.049	0.018	0.053
	0.97	1.941	5.489	0.198	1.829	1.832	0.019	0.051	0.019	0.055
	0.92	1.943	5.493	0.213	1.831	1.832	0.020	0.055	0.020	0.059
	0.87	1.945	5.498	0.231	1.832	1.834	0.021	0.060	0.022	0.064

Table 8.10: The partial charges of Hg-1223 as a function of the unit cell volume.

V/V_{opt}	$\omega[cm^{-1}]$	$\omega[cm^{-1}]$	$\omega[cm^{-1}]$	$\omega[cm^{-1}]$	Ba	Cu1	O1	O2	Ca1
		Ref. [86]	Ref. [87]	Ref. [88]					
1	592.1	526	576	580-589	0.01	0.02	-0.13	0.99	0.02
					-0.01	0.02	-0.02	1.00	0.02
0.97	610.4				0.00	0.03	-0.12	0.99	0.03
0.92	623.4				0.02	0.04	-0.16	0.99	0.04
0.87	622.2								
1	368.9		477	400	-0.13	-0.12	0.91	0.13	-0.35
					-0.03	-0.08	0.52	0.03	-0.85
0.97	344.6				-0.15	-0.09	0.86	0.12	-0.46
0.92	423.6				-0.12	-0.08	0.87	0.16	-0.44
0.87	415.4								
1	273.2	260	300	264	-0.21	-0.11	0.31	0.02	0.92
					-0.29	-0.24	0.77	0.01	0.50
0.97	283.5				-0.29	-0.12	0.40	0.03	0.86
0.92	296.6				-0.17	-0.10	0.41	0.04	0.89
0.87	325.7								
1	146.7	150	151	152 (131)	-0.62	0.79	0.00	-0.01	-0.04
					-0.68	0.73	0.00	-0.02	-0.05
0.97	146.6				-0.66	0.74	-0.08	-0.03	-0.08
0.92	151.9				-0.80	0.59	-0.08	-0.02	-0.05
0.87	155.5								
1	72.9	104	92	106	-0.75	-0.60	-0.24	-0.01	-0.16
					-0.67	-0.63	-0.36	0.00	-0.14
0.97	42.8				-0.68	-0.65	-0.28	-0.01	-0.18
0.92	73.4				-0.56	-0.80	-0.21	0.01	-0.10
0.87	103.3								

Table 8.11: The eigenfrequencies and eigenvectors of the lattice vibrations in Hg-1223.

tion and an estimation about the uncertainties in the calculation of the Raman intensities. The Raman intensity of the O2 mode, depicted in Figure 8.23, shows, similarly as in the Hg-1212 compound, that the intensity increases with applied pressure. However, like it has already been discussed for the latter material and can also be seen in Figure 8.24 this behavior strongly depends on the used laser frequency. The trend that the peak in the Raman spectra is shifted to higher frequencies with applied pressure as shown in Reference [89] is obviously reproduced by the calculations.

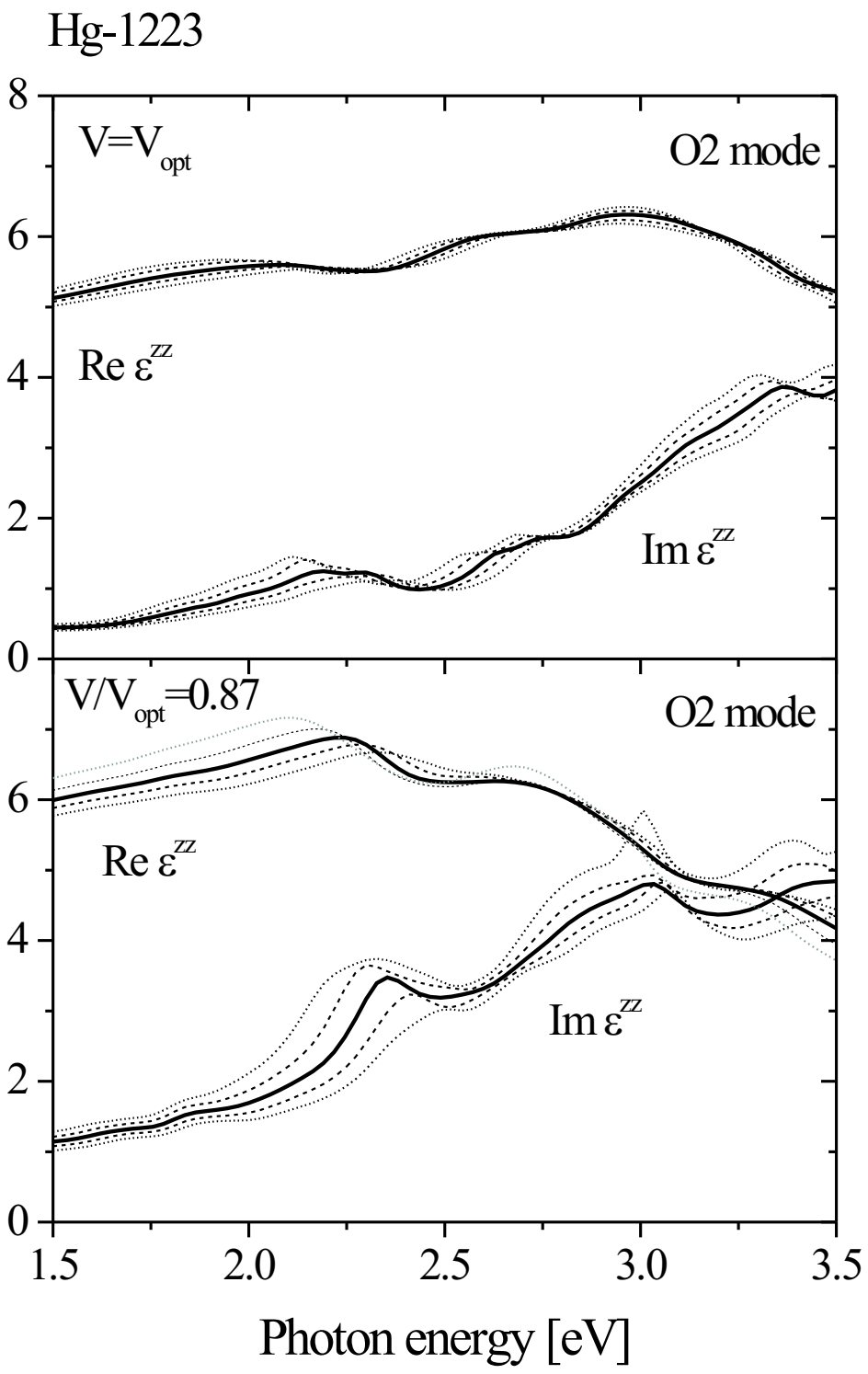

Figure 8.22: The dielectric tensor component ϵ^{zz} of the Hg-1223 for different displacements of the O2 atom at two different unit cell volumes.

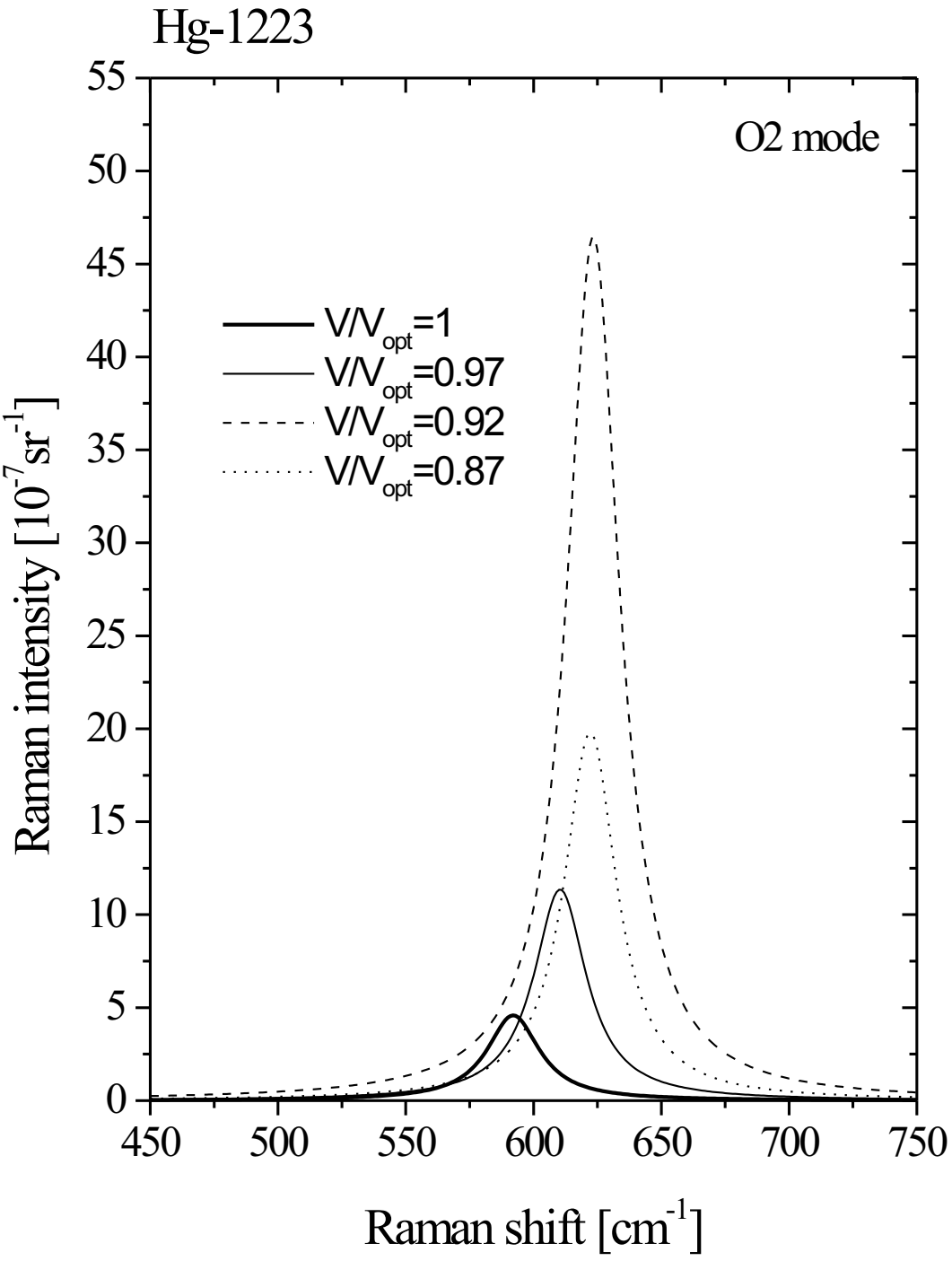

Figure 8.23: The Raman intensity of the O2 peak in Hg-1223 with $\Gamma = 25K$ at E_L=2.4 eV.

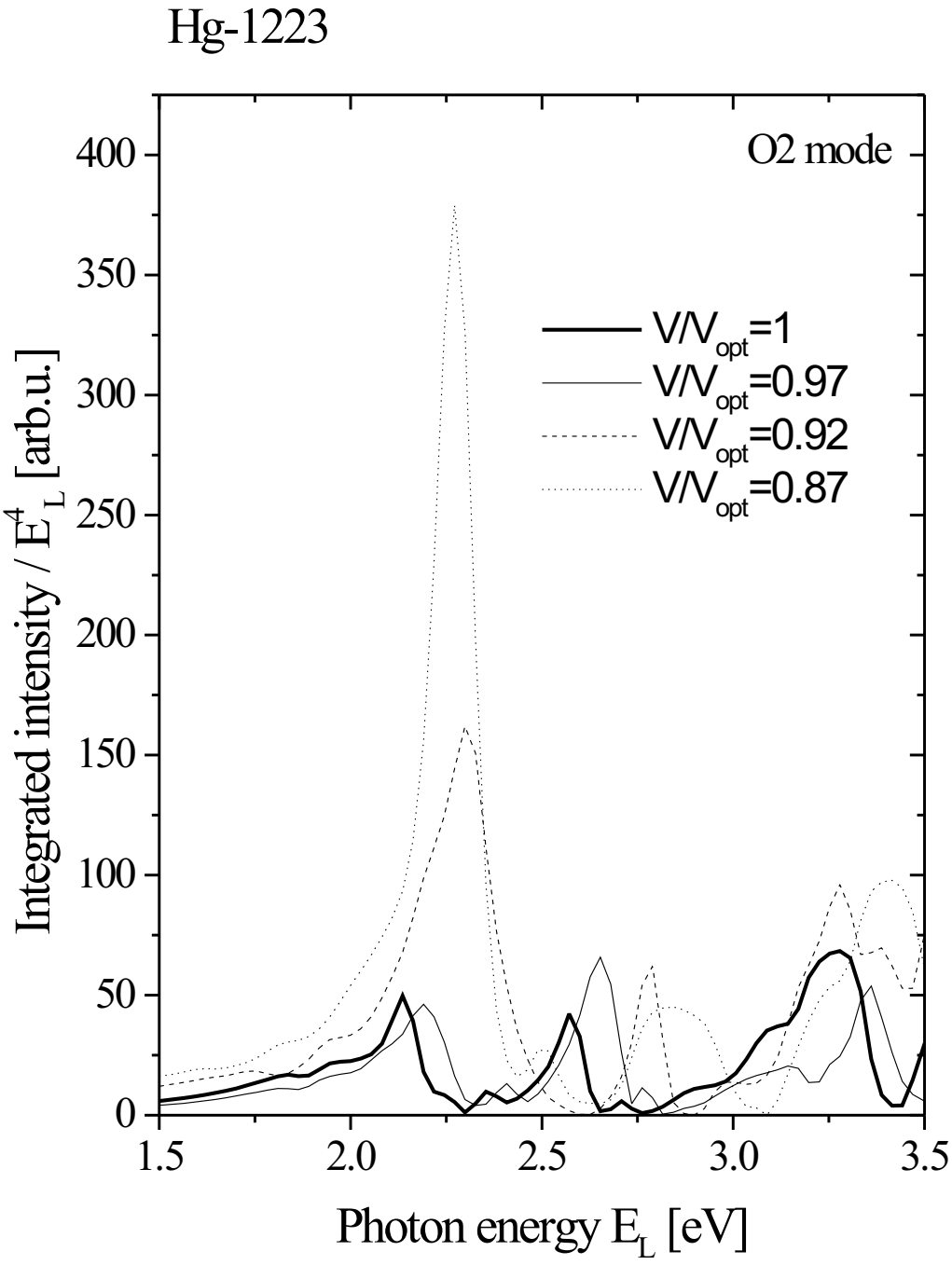

Figure 8.24: The resonance behavior of the integrated Raman intensity of Hg-1223.

8.5 Hg-1234

Also for the four-layer compound Hg-1234 an optimization of the lattice parameters has been carried out. The experimental lattice constants and atomic positions, which served as a starting point for this procedure were taken from Reference [90]. It turned out that compared to these data the calculated optimized structural parameters show a 2% smaller unit cell volume and the same c/a-ratio (see Table 8.12).

	a	$\Delta a/a_{\mathrm{opt}}$	c	$\Delta c/c_{\mathrm{opt}}$	V	$\Delta V/V_{\mathrm{opt}}$
	[a.u.]	[%]	[a.u.]	[%]	[a.u.^{3}]	[%]
V_{opt}	7.277	0	35.888	0.000	1862.863	
V_{ref}	7.205	1	35.885	0.008	1900.603	+2 %

Table 8.12: The structural data of Hg-1234.

The changes in the layer distances are displayed in Table 8.13.

Like the other members of the Hg-family also Hg-1234 exhibits a two dimensional character of its band structure (see Figure 8.25). The important characteristics of the band structure remain the same as in Hg-1201, Hg-1212, and Hg-1223 with the only major difference that Hg-1224 is having a fourth CuO_2 band, which is crossing the Fermi level.

The total and partial densities of states are shown in Figure 8.26 and the corresponding partial charges are displayed in Table 8.15. For the optimized geometry also the phonon frequencies and eigenvectors have been calculated. Looking at Table 8.14 it can be seen, that there is again an uncoupled vibration of the O2 atom, which is the highest one in frequency, accompanied by 6 additional modes which turned out to have a mixed character consisting of Cu1, Cu2, O1, O3, Ca, and Ba components.

	z_{Ba}	z_{Cu1}	z_{Cu2}	z_{O1}	z_{O2}	z_{O3}	z_{Ca1}
	[a.u.]	[a.u.]	[a.u.]	[a.u.]	[a.u.]	[a.u.]	[a.u.]
$V_{\rm opt}$	5.510	9.491	15.007	9.306	3.698	15.051	12.092
$V_{\rm ref}$	5.337	8.899	15.014	8.777	3.912	15.136	11.836

Table 8.13: The atomic positions in Hg-1234.

$\omega[\mathrm{cm}^{-1}]$	Ba	Cu1	Cu(2)	O1	O3	O2	Ca1
598.8	0.00	0.02	0.00	-0.11	-0.01	0.99	0.03
382.4	-0.11	-0.07	0.04	0.73	-0.66	0.08	-0.06
364.2	0.04	0.07	0.06	-0.53	-0.65	-0.08	0.53
238.6	-0.30	-0.16	-0.16	0.32	0.34	0.02	0.80
141.5	0.52	-0.83	-0.22	-0.04	-0.04	0.01	0.02
111.5	0.27	-0.09	0.93	0.11	0.14	0.01	0.17
85.4	-0.75	-0.53	0.24	-0.24	-0.06	-0.01	-0.21

Table 8.14: The eigenfrequencies and eigenvectors of the phonon modes of Hg-1234.

	s	p	d	p_x	p_z	d_{z^2}	d_{x^2-y2}	d_{xy}	d_{xz}
Hg	0.390	6.044	8.046	1.994	2.056	1.439	1.632	1.629	1.673
Ba	1.799	4.555	10.008	1.520	1.516	2.001	2.001	2.002	2.003
Cu1	0.227	6.171	8.693	2.075	2.023	1.727	1.440	1.859	1.834
Cu2	0.229	6.170	8.684	2.075	2.022	1.730	1.437	1.857	1.830
O1	1.531	3.437	0.011	1.120	1.197	0.002	0.003	0.003	0.002
O2	1.541	3.379	0.010	1.201	0.976	0.005	0.000	0.000	0.002
O3	1.530	3.443	0.011	1.125	1.194	0.002	0.003	0.003	0.002
Ca1	1.940	5.487	0.189	1.828	1.831	0.018	0.048	0.018	0.053
Ca2	1.940	5.486	0.184	1.828	1.830	0.018	0.047	0.016	0.052

Table 8.15: The partial charges of Hg-1234.

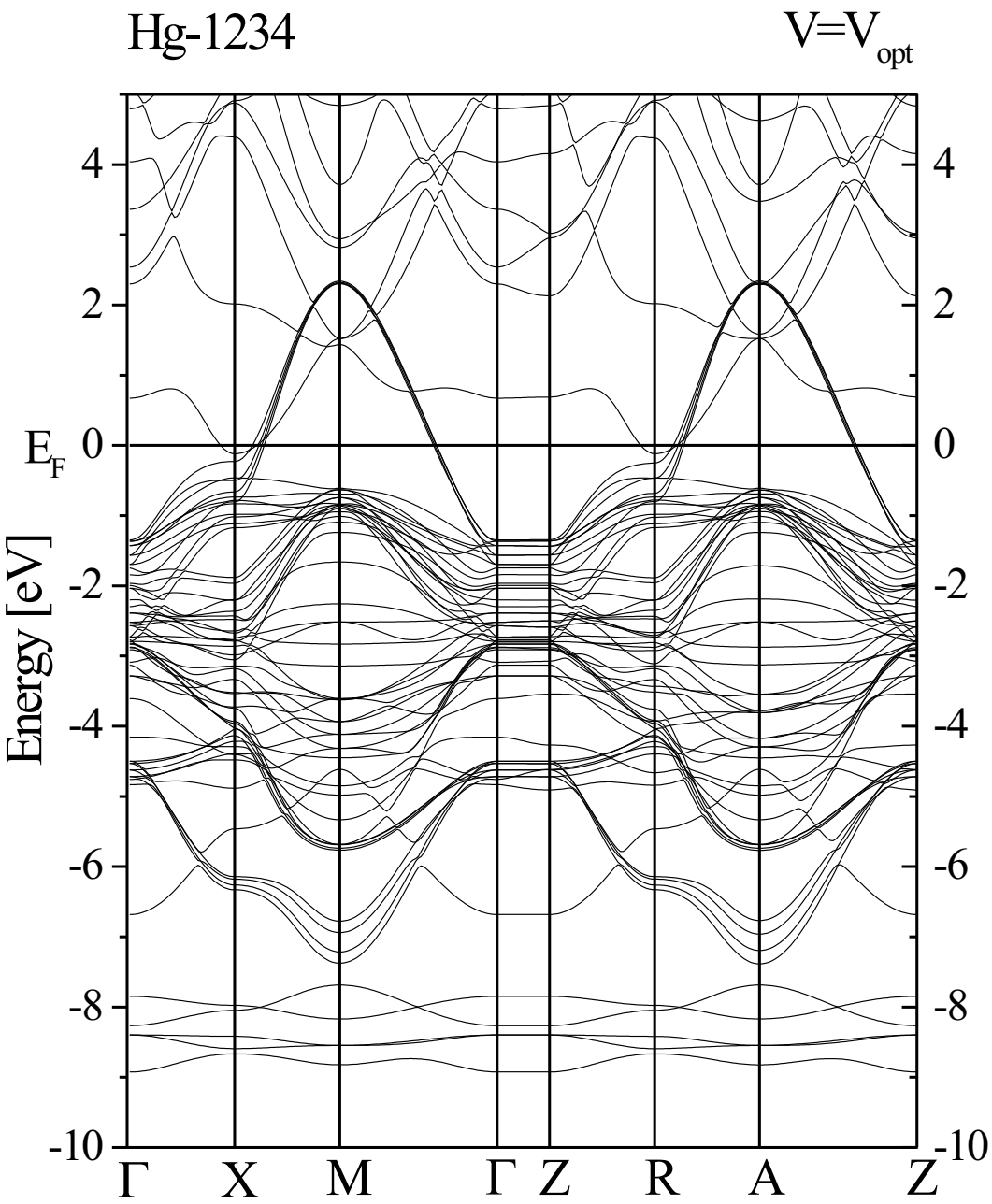

Figure 8.25: The band structure of Hg-1234 at $V = V_{\text{opt}}$.

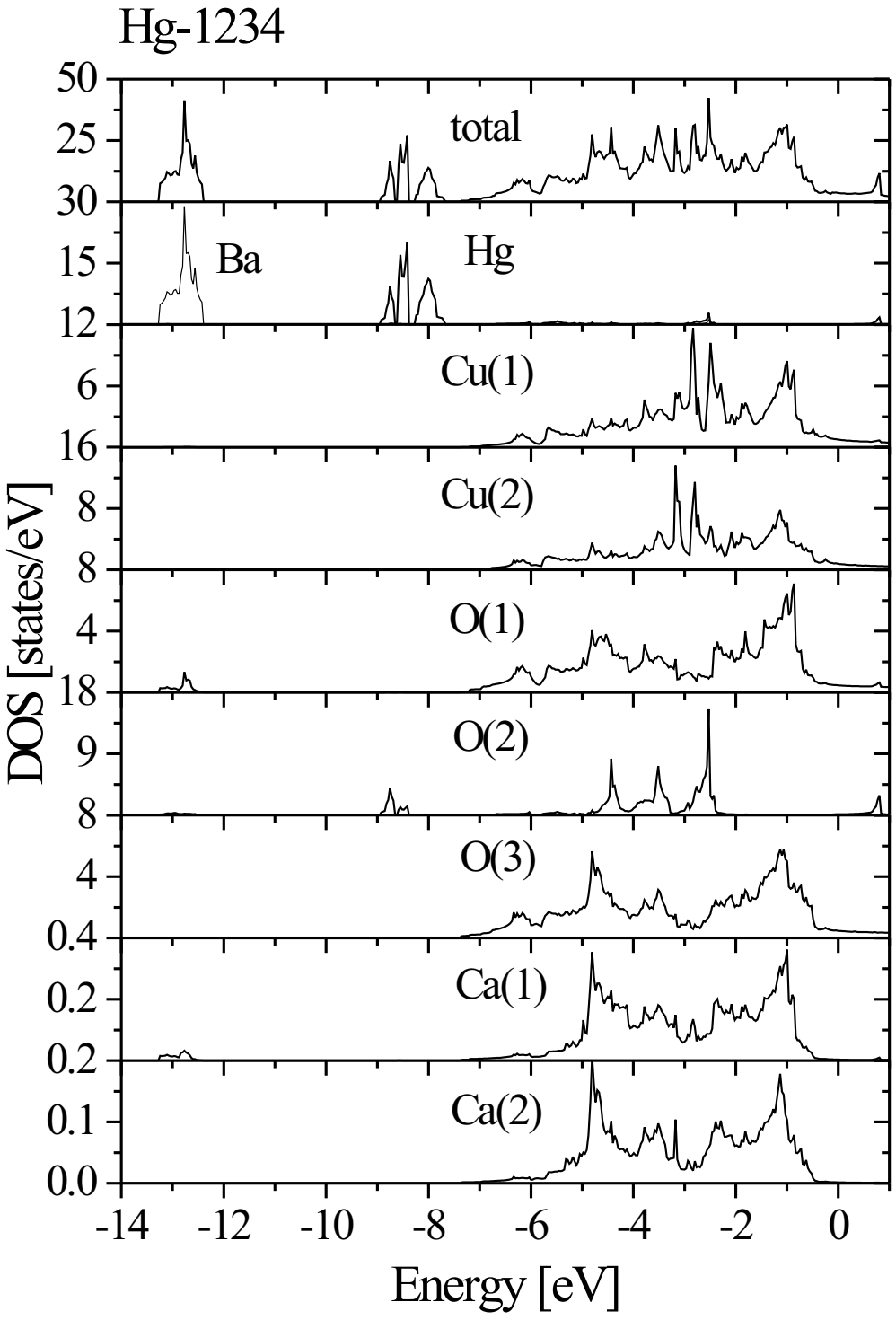

Figure 8.26: The total and site-projected densities of states of Hg-1234.

8.6 Doping of Hg-1201

It is commonly believed that the charge carriers responsible for the superconducting pairing of high T_c cuprates are holes mainly confined to the CuO_2 layers. Similar correlations between T_c and and n_s/m^*, with n_s and m^* being the charge carrier density and the effective mass, respectively, do not only include high T_c materials, but also other families of superconductors [91]. A universal relationship between T_c/T_c^{max} and the hole content p, exhibiting a common feature among the p-type high-T_c superconductors, was presented by Zhang *et al.* [92]. This dependence is characterized by a plateau, where the variation of T_c/T_c^{max} is independent of the compound considered.

In all these materials of interest the actual amount of holes is driven by doping. However, for most of the theoretical models describing the superconducting phase transition the hole content rather than the doping level is the crucial input parameter. Above all, hardly anything is known about the relationship between these two physical quantities. Without a detailed knowledge of how doping influences the number of carriers in the normal state, also the superconducting properties will lack a profound understanding. In view of being able to tune the amount of carriers and thereby the superconducting transition temperature a full clarification of how doping affects the electronic structure is not only highly interesting, but even inevitable. In this context the questions are raised, where the excess charge goes upon doping, how does doping influence the carrier concentration in the copper-oxygen planes, and what limits the amount of holes in these building blocks.

In order to address these topics, electronic structure calculations have been carried out for the simplest representative of the Hg-based high T_c cuprate, $HgBa_2CuO_{4+\delta}$. For this compound an optimum oxygen concentration of $\delta_{opt} \simeq 0.22$ was found [93] with a T_c^{max} of 97 K for ambient pressure which is the the highest T_c of any single-layer cuprate.

Theoretically, doping effects in this class of materials have been studied for a high doping level of $\delta = 1/2$ only [94, 95] revealing strong covalent bonding in the basal plane with large overlap of the Hg and the dopant oxygen orbitals. This oxygen concentration, however, has never been achieved experimentally. Therefore a detailed study of the much more important low doping regime was highly desirable.

In the following investigations special emphasis is put to the doping induced redistribution of the hole concentration in the CuO_2 layer. In addition, the doping effect on the crystal structure and the Raman spectra are studied.

Arbitrary doping levels, are usually hard to achieve since they require calculations for supercells with large unit cell volumes for low doping concentrations. Within this thesis, two approaches have been made in order to treat doping in the Hg-1201 system. First, supercell calculations have been carried out for several doping levels (unit cells up to 9 single cell volumes). In order to make arbitrary

doping levels feasible, virtual crystal (VC) calculations have been performed as well. It will be shown below that such kind of calculations are justified for this special case.

For the systematic study of the doping-dependent electronic structure, the crystalline data as a function of doping have been taken from Ref. [49].

8.6.1 Supercell Calculations

Supercell calculations have been performed for $\delta = 1/8$, $\delta = 1/6$, $\delta = 1/5$, $\delta = 2/9$, $\delta = 1/4$, $\delta = 1/3$, and $\delta = 1/2$. For the latter two, two different geometries have been considered in order to check the sensitivity of the results to the actual site and surrounding of the excess oxygen. The basal planes of the unit cells used during these calculations are depicted in Figure 8.27.

As already described above, in the undoped material the Fermi level intersects a single free-electron-like two-dimensional half-filled $dp\sigma^*$ band, with its states being of Cu($d_{x^2-y^2}$) and O(p_x) character. Upon doping the effect on the electronic structure is twofold. First, the dopant adds states at the Fermi level, where these new charge carriers cause a shift of E_F. Second, the shift of the Fermi level changes the carrier concentration in the CuO_2 plane. This can be seen in Figure 8.28 where the corresponding losses in the partial charges with respect to the undoped system are displayed for a selected number of doping concentrations.

At the optimal doping the occupation number for the copper $d_{x^2-y^2}$ orbital $Q(d_{x^2-y^2})$ is decreased by 0.072 e (from 1.442 e for the undoped case to 1.370 e for δ_{opt}), and similarly the O1(p_x) charge $Q(p_x)$ drops by 0.024 e (from 1.113 to 1.101 for one oxygen). Both orbitals clearly exhibit their minimum occupation number (maximum amount of holes) as a plateau starting close to the experimentally observed optimal doping content. The hole concentration within the copper-oxygen planes with respect to the undoped case is obtained by $[Q(d_{x^2-y^2})(0) + 2 \times Q(p_x)(0)]$ - $[Q(d_{x^2-y^2})(\delta) + 2 \times Q(p_x)(\delta)]$ also displayed in Figure 8.28. Close to the experimental results [93] the optimal value is found to be ≈ 0.13 e. One should recall here that the partial charges depend on the atomic sphere radii and therefore the absolute values are somewhat bigger. An estimate of the corrected value gives 0.16e which exactly reproduces the experimental value.

It should be noticed that for $\delta = 1/5$ the number of doping induced holes does not exactly lie on the straight line indicated by the other doping concentrations. This finding can be easily explained by the stretched geometry of the supercell (see Figure 8.27). Similar effects are found for $\delta = 1/3$ and $\delta = 1/2$.

The total and partial charges of all the other atomic spheres remain nearly unchanged upon doping as can be seen from Table 8.16.

The increase of the hole content can be generally understood in an ionic picture: The excess oxygen attracts electrons from the copper-oxygen plane thereby increasing the hole concentration in this region. In fact, the OI states do not show strong overlap with the neighboring Hg states in the entire doping regime up to

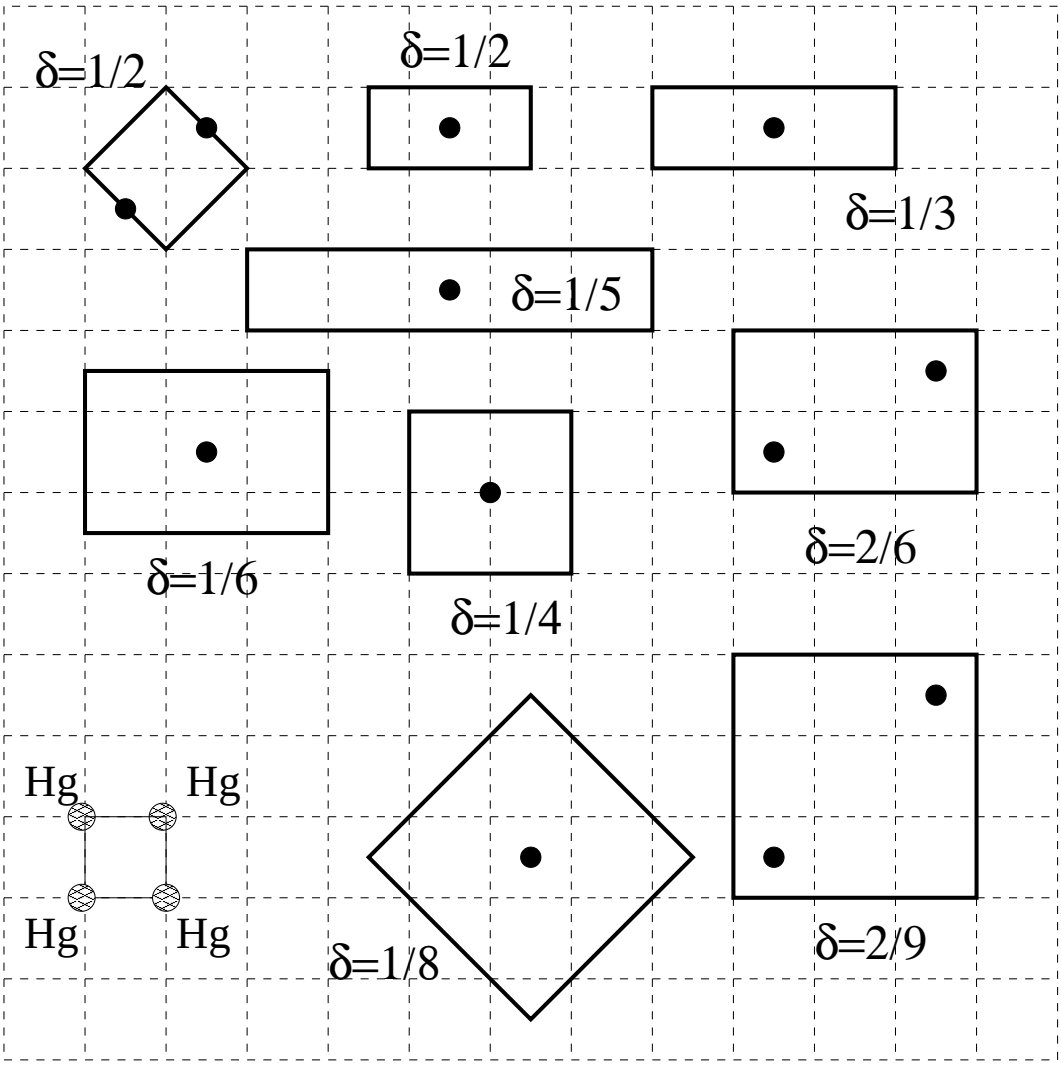

Figure 8.27: The choices of supercells for different concentrations of excess oxygen (black dots). The corners of the mesh represent the Hg positions in the basal plane as indicated for one single unit cell.

	δ	s	p	d	p_x	p_z	d_{z^2}	$d_{x^2-y^2}$	d_{xy}	d_{xz}
Hg	0.125	0.383	6.038	8.058	1.993	2.053	1.452	1.634	1.631	1.671
	0.167	0.379	6.036	8.058	1.992	2.050	1.452	1.634	1.631	1.670
	0.22	0.375	6.034	8.059	1.993	2.049	1.456	1.634	1.630	1.669
	0.25	0.372	6.033	8.064	1.992	2.048	1.461	1.635	1.632	1.668
	0.33	0.366	6.033	8.064	1.993	2.048	1.455	1.635	1.637	1.669
Ba	0.125	1.737	4.285	10.003	1.431	1.425	2.000	2.000	2.001	2.001
	0.167	1.737	4.286	10.003	1.430	1.426	2.000	2.000	2.001	2.001
	0.22	1.737	4.287	10.003	1.430	1.427	2.000	2.000	2.001	2.001
	0.25	1.737	4.287	10.003	1.430	1.427	2.000	2.000	2.001	2.001
	0.33	1.737	4.288	10.003	1.429	1.428	2.000	2.000	2.001	2.001
Cu1	0.125	0.215	6.150	8.688	2.067	2.018	1.770	1.390	1.857	1.837
	0.167	0.214	6.151	8.683	2.067	2.018	1.771	1.379	1.857	1.838
	0.22	0.213	6.152	8.680	2.067	2.018	1.774	1.370	1.858	1.839
	0.25	0.213	6.152	8.676	2.067	2.018	1.776	1.362	1.858	1.840
	0.33	0.212	6.152	8.675	2.067	2.018	1.773	1.365	1.857	1.840
O1	0.125	1.529	3.434	0.010	1.109	1.218	0.001	0.003	0.002	0.002
	0.167	1.530	3.430	0.010	1.105	1.220	0.001	0.003	0.002	0.002
	0.22	1.530	3.424	0.009	1.101	1.222	0.001	0.003	0.002	0.002
	0.25	1.531	3.421	0.009	1.098	1.226	0.001	0.003	0.002	0.002
	0.33	1.531	3.421	0.009	1.098	1.225	0.001	0.003	0.002	0.002
O2	0.125	1.539	3.365	0.010	1.199	0.968	0.005	0.000	0.000	0.002
	0.167	1.540	3.366	0.010	1.200	0.967	0.005	0.000	0.000	0.002
	0.22	1.540	3.367	0.009	1.202	0.962	0.005	0.000	0.000	0.002
	0.25	1.539	3.368	0.009	1.202	0.963	0.005	0.000	0.000	0.002
	0.33	1.540	3.364	0.009	1.202	0.961	0.005	0.000	0.000	0.002
OI	0.125	0.228	0.499	0.001	0.160	0.180	0.000	0.000	0.001	0.000
	0.167	0.304	0.665	0.002	0.211	0.243	0.001	0.000	0.001	0.000
	0.22	0.406	0.885	0.002	0.273	0.338	0.001	0.000	0.001	0.000
	0.25	0.456	0.997	0.002	0.315	0.368	0.001	0.000	0.001	0.000
	0.33	0.609	1.318	0.003	0.406	0.505	0.001	0.000	0.001	0.000

Table 8.16: The partial charges as a function of the doping parameter δ obtained from supercell calculations. Depending on the choice of the supercell there are non-equivalent positions of the various atoms. Therefore the partial charge given in this table are the averaged values.

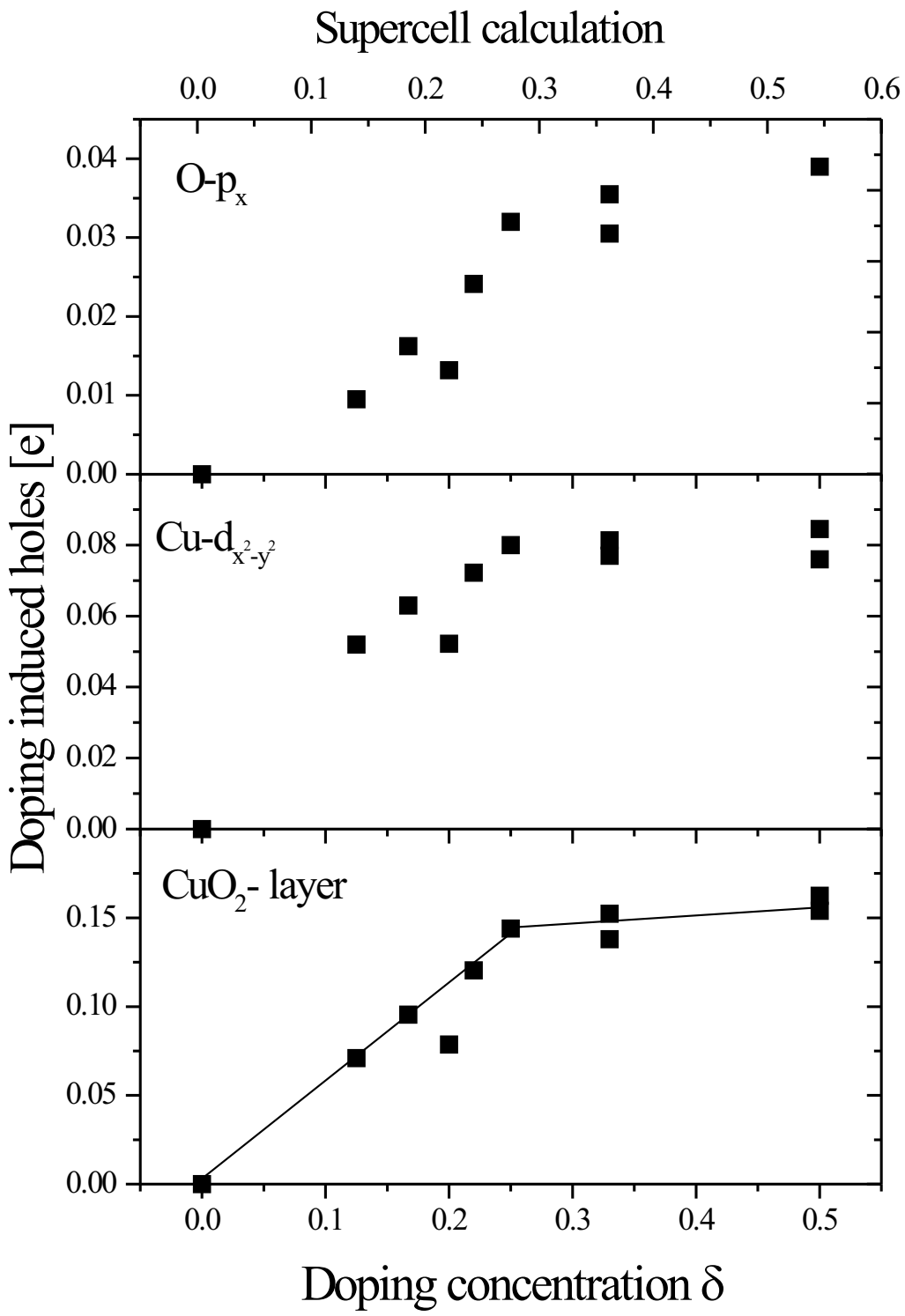

Figure 8.28: The partial charges of the CuO_2 plane as a function of δ obtained from supercell calculations.

optimal doping. This picture is also confirmed by the partial densities of states for doping concentrations of $\delta = 1/6$ (Figures 8.29, 8.30) and $\delta = 1/4$ (Figures 8.31, 8.32). They show nearly constant oxygen and cooper contributions at E_F with vanishing Hg–*d* admixture, whereas the Hg–*d* states are found somewhat below. Furthermore covalent bonding of Cu1 and O1 with peaks at -0.35 eV and a small feature right below E_F is exhibited. Covalent bonds are also formed by Hg and the apical oxygen O2, whereas the dopant atom OI has the highest contribution to the DOS at the Fermi level with hardly any common feature with mercury. This fact is supported by the partial charges in the Hg sphere which are not affected by doping (see Table 8.16). In the overdoped region, investigated for $\delta = 1/3$, and for $\delta = 1/2$, stronger bonds between oxygen and mercury atoms are formed as was also found in the three-layer compound for the heavily oxygenated material [95].

Now the question arises, what the limiting fact for the creation of holes in the CuO_2 plane is. The results of the supercell calculations fully support the conclusion drawn from VC calculations [96]: The hole concentration in the cuprate planes reaches its maximum when the dopant band is completely occupied, i.e. for a *closed OI shell*. Since the excess oxygen attracts electrons from the CuO_2 plane, its orbitals will be systematically filled up not only by the electrons provided by the oxygen atom itself, but also by those coming from the CuO_2 unit. Only in the overdoped region covalent bonds between oxygen and mercury atoms are formed. By this change the pure ionic character of the dopant oxygen gets lost and therefore no more carriers are attracted from the CuO_2 plane. These findings also show up in the density of states which in the optimal doping regime exhibits an almost filled band right below E_F.

8.6.2 Virtual Crystal Calculations

In these calculations an arbitrary doping concentration δ has been treated by adding the appropriate amount of valence electrons, which is $6 \times \delta$ (6 electrons for the fully doped cell), to the crystal in a single-cell calculation. To guarantee charge neutrality the corresponding positive charge was placed in a sphere at the doping oxygen site, i.e. in the middle of the Hg squares in the basal plane. This quite crude approximation, the VC approach, should usually not be used for simulating fractional oxygen occupations. However, the special situation, i.e. due to the ionic character of the dopant oxygen OI far from the overdoped region, this procedure seems to be justified. A comparison of the increase of the hole concentration between the results of the supercell calculations (Figure 8.33) and the VC calculations (8.28), respectively, indeed exhibits the same behavior of the partial charges in the CuO_2 plane as a function of doping. Therefore it can be concluded that the VC calculations lead to reliable results in the underdoped region, where the picture of the ionic behavior of OI is valid.

In a next step, also the effect of doping on the lattice parameters and atomic

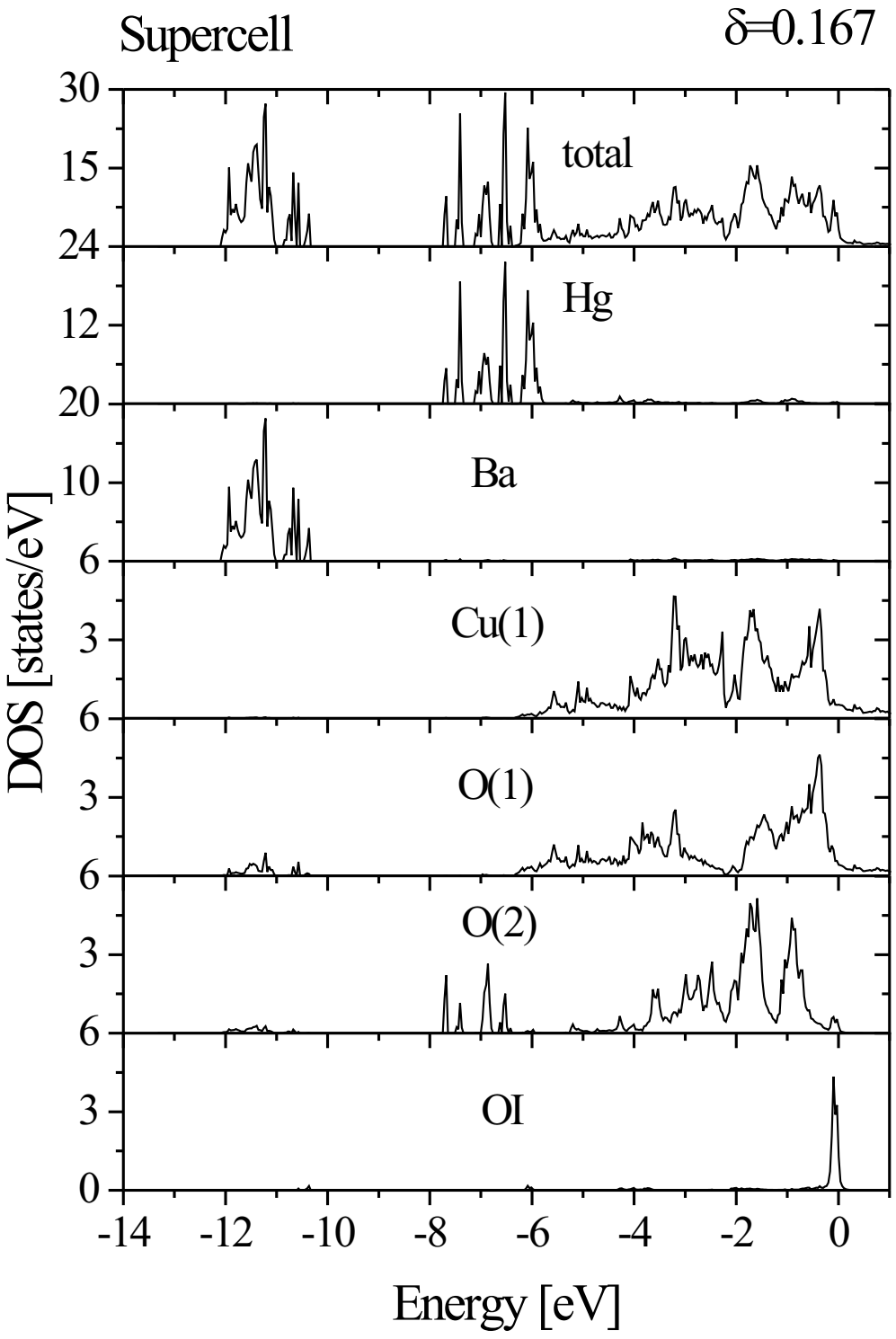

Figure 8.29: The total and partial densities of states for $HgBa_2CuO_{4+\delta}$ with $\delta = 1/6$ obtained from supercell calculations.

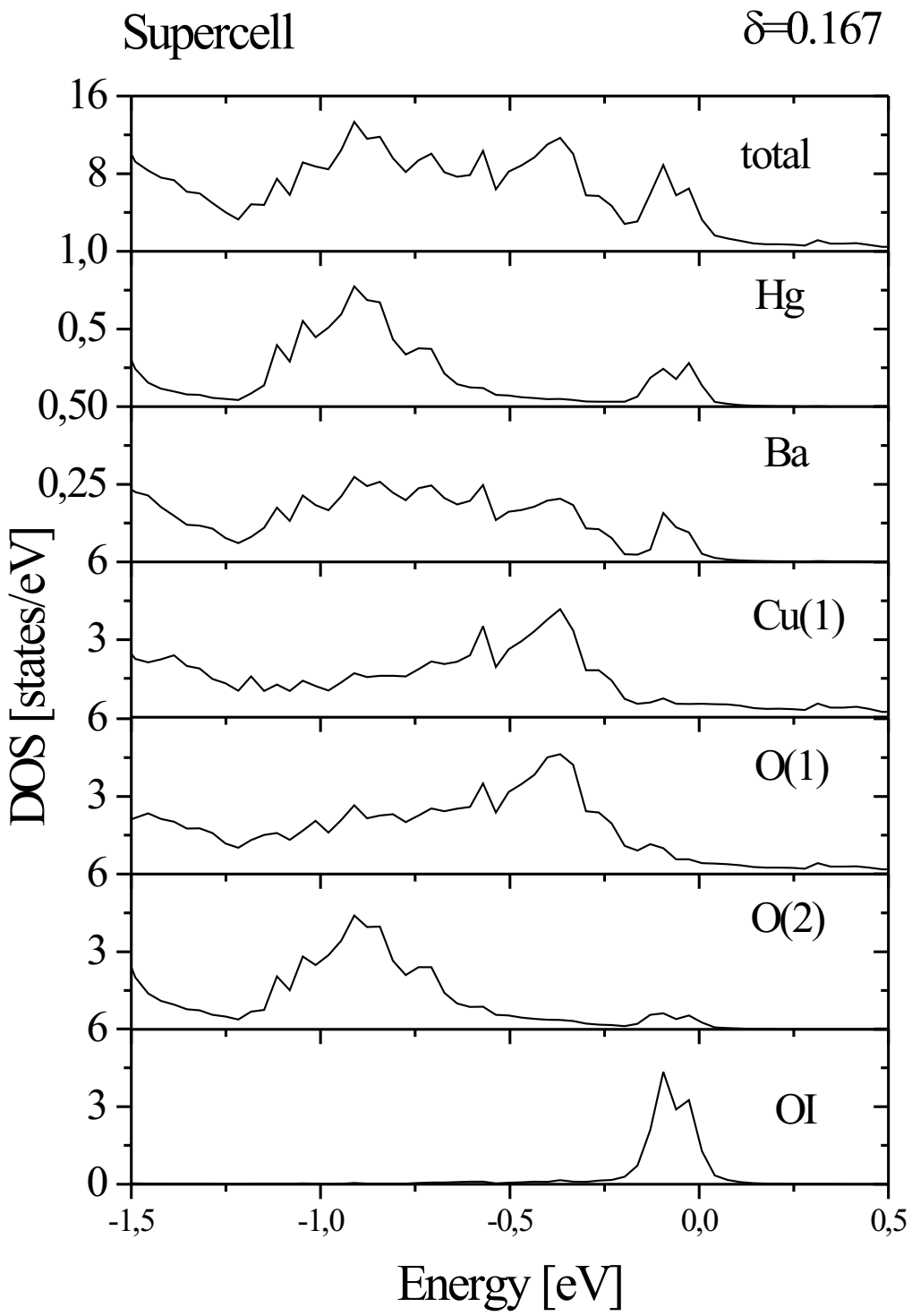

Figure 8.30: The total and partial densities of states around the Fermi level for $HgBa_2CuO_{4+\delta}$ with $\delta = 1/6$ obtained from supercell calculations.

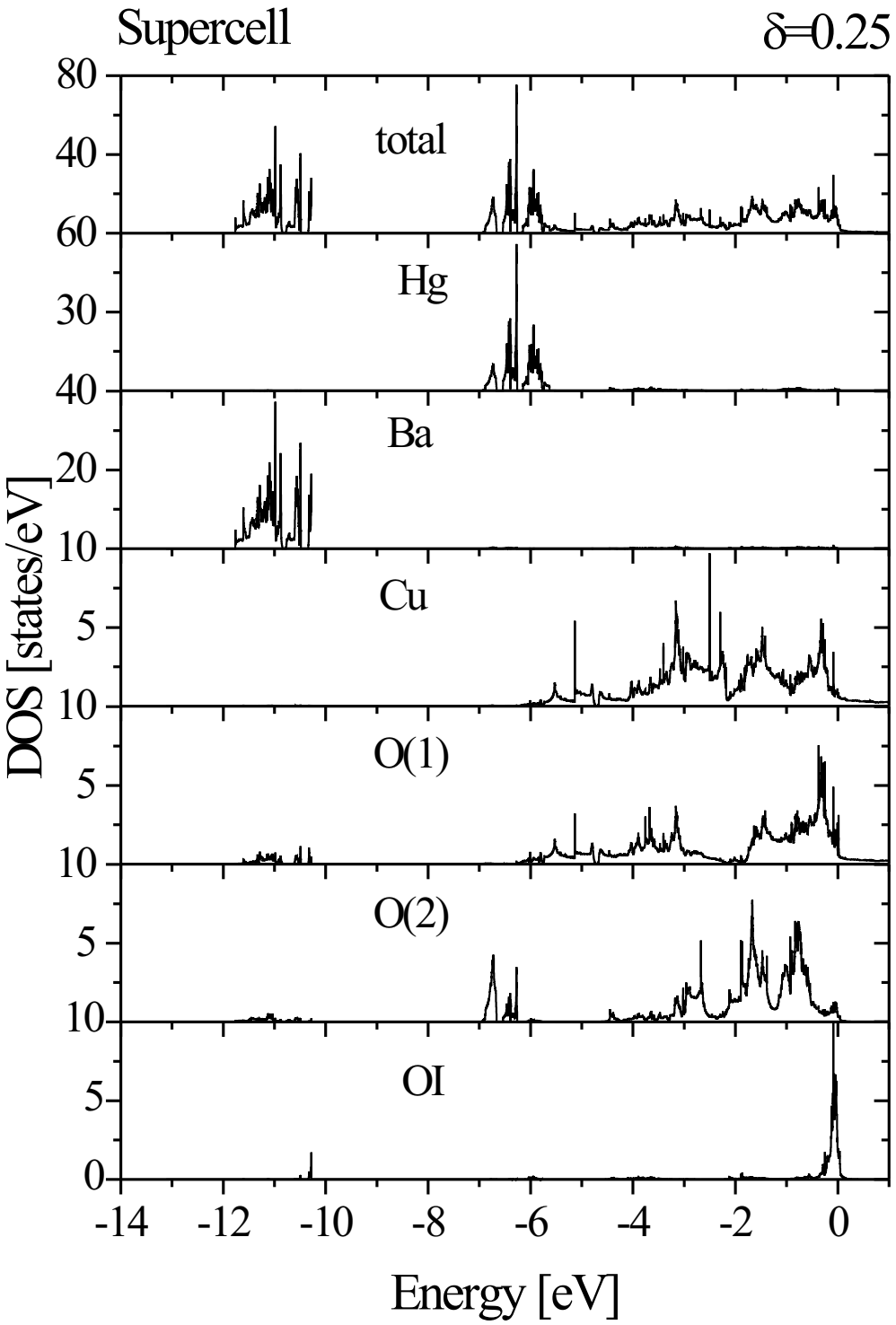

Figure 8.31: The total and partial densities of states for $HgBa_2CuO_{4+\delta}$ with $\delta = 1/4$ obtained from supercell calculations.

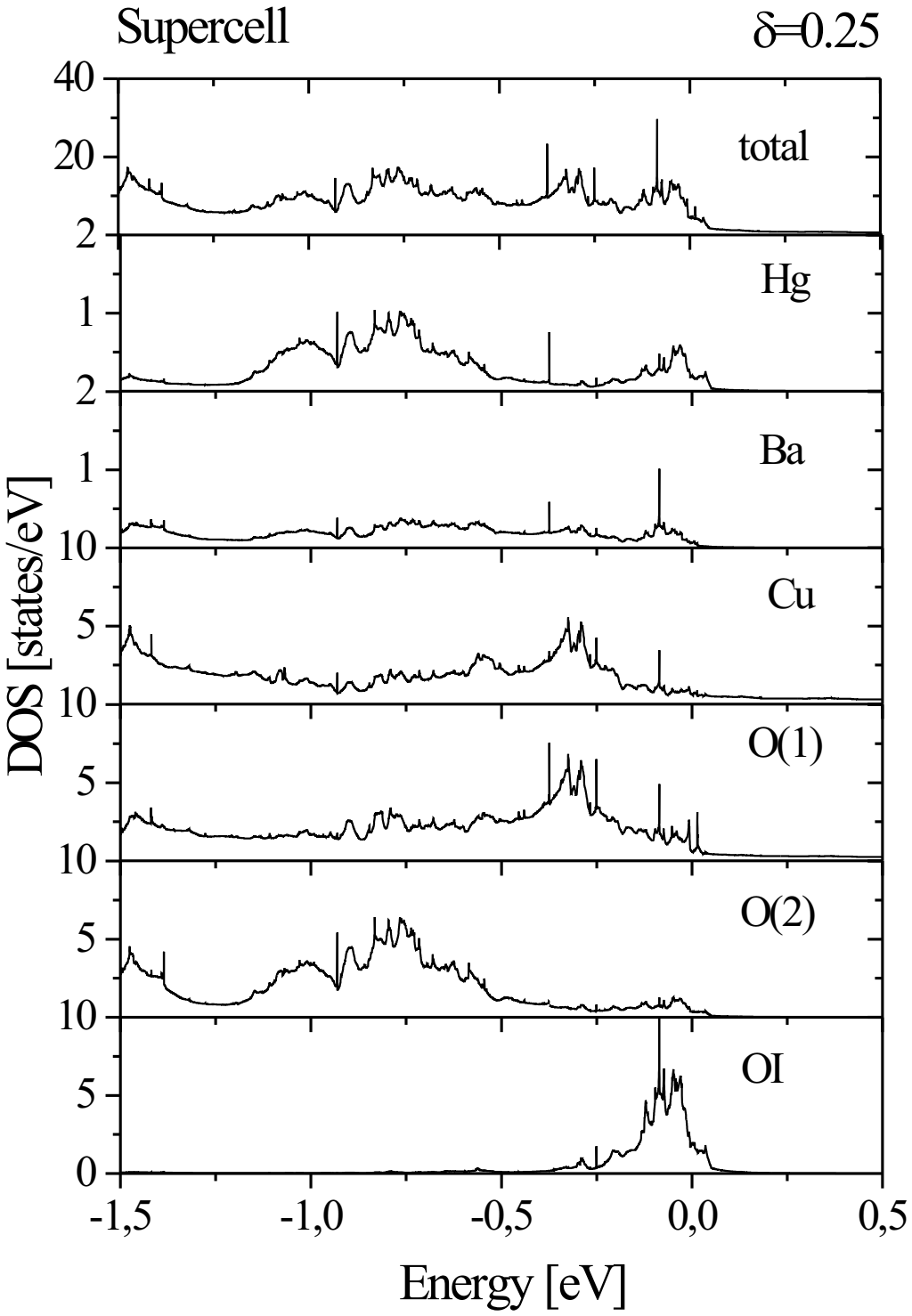

Figure 8.32: The total and partial densities of states around the Fermi level for $HgBa_2CuO_{4+\delta}$ with $\delta = 1/4$ obtained from supercell calculations.

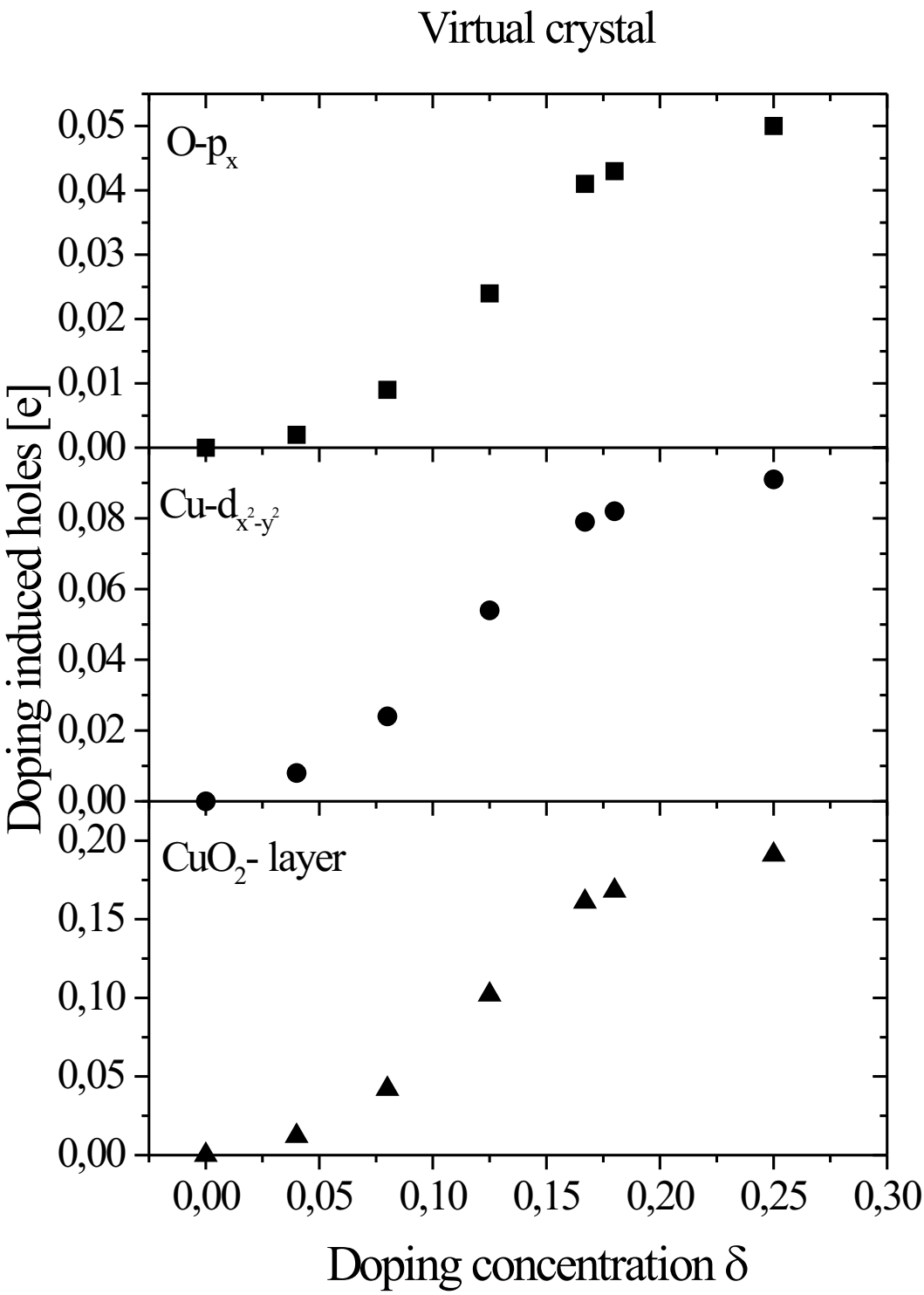

Figure 8.33: The partial charges of the CuO_2 plane as a function of δ obtained from virtual crystal calculations.

positions by total-energy and atomic-force calculations has been investigated. Not only the electronic properties, but also the crystal structure is influenced by doping. The redistribution of bond lengths can again be explained within the ionic picture. Since doping does not change the symmetry of the crystal, it only leads to displacements of Ba and the apical oxygen in z-direction. With increasing oxygen content at the doping site, the positive Ba ions are expected to be attracted by the oxygen, whereas the negatively charged O2 ions should be repelled. Indeed a shift of the Ba position towards the basal plane is observed together with a displacement of the O2 ions away from this plane. In Fig. 8.34 the corresponding z-coordinates of both atoms are shown which were calculated by fully optimizing the crystalline data for selected doping concentrations in the virtual crystal approach: For δ=0, 0.08, 0.17, and 0.23 the unit cell volumes, c/a ratios, and atomic positions were obtained by total-energy and atomic-force calculations using the procedure like for the undoped materials. The results are displayed in Table 8.6.2.

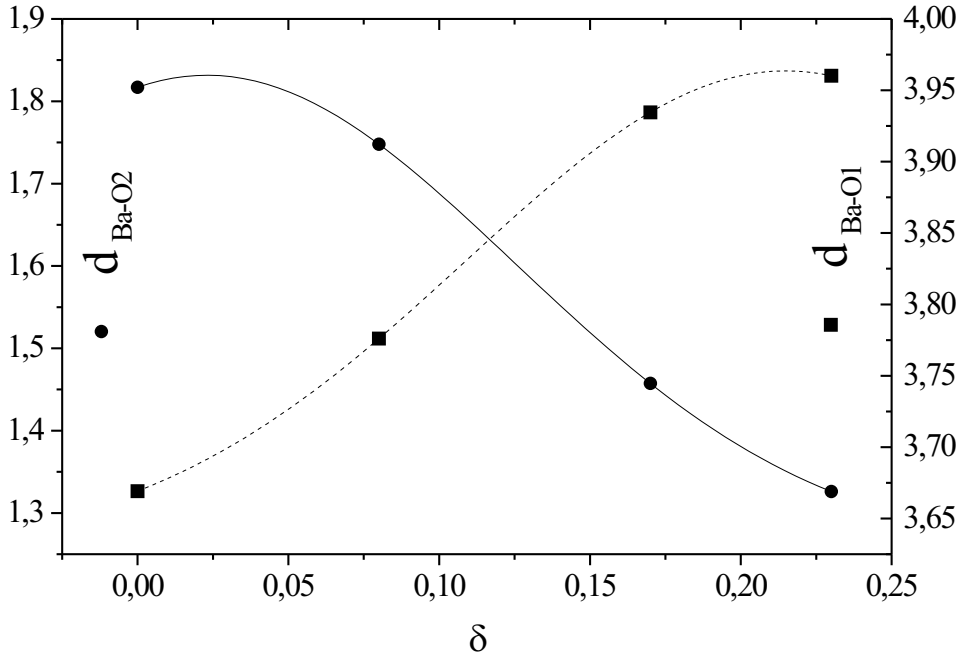

Figure 8.34: Hg-1201: Atomic positions and distances as a function of the doping level δ obtained within the virtual crystal approach.

All trends are in agreement with experimental observations [49]: These are a shrinkage of the unit cell upon doping, a shortening of the lattice parameter a, an increase of c for small doping levels followed by a nearly linear decrease, an increasing distance between the basal plane and the Ba layer, as well as a reduction of the distance between the layers of Ba and O2. In agreement with

δ	a [Å]	c [Å]	Ω [Å^3]	z_{Ba} [c]	z_{O2}[c]
0.00	3.8574	9.7228	144.6676	0.3003	0.2014
0.08	3.8192	9.8191	143.2211	0.2965	0.2023
0.17	3.8058	9.6887	140.3283	0.2851	0.2055
0.23	3.8312	9.5604	140.3280	0.2808	0.2074

Table 8.17: Crystalline data as a function of doping obtained from total-energy and atomic-force calculations.

measured data, the latter two quantities show a less pronounced dependence up to $\delta = 0.08$ and a stronger one for higher oxygen contents.

With the optimized lattice parameters the Raman intensities of the O2 dominated lattice vibration have been calculated. Although the trends should be reproduced quite reasonably, one cannot expect to describe *reality* in detail within the VC approach. E.g in the real crystal the doping with oxygen leads to local effects like the presence of two different Ba sites as described by Huang *et al.* [49] or the deformation for the crystal by the excess oxygen as it is was argued by Zhang *et al.* [50].[3] All these effects are averaged by the virtual crystal approximation. Nevertheless, the following results will give a guideline of how the Raman spectra could evolve as a function of doping. The frequencies for the Ba and O2 vibrations are listed in Table 8.18. It can be seen that the phonon-frequency of

δ	ω_{O2}	ω_{Ba}
	$[cm^{-1}]$	$[cm^{-1}]$
0.00	590	144
0.08	545	139
0.17	542	134
0.23	583	145

Table 8.18: Phonon frequencies as a function of the doping parameter δ.

the O2 dominated vibration shows the tendency to be lowered with increasing oxygen content. Looking at Figure 8.35 also a decrease of the Raman intensity with increased doping concentration is found. In the experimental spectra as mentioned in the previous sections there are two peaks with less intensity than the A_{1g} vibrations, which can be attributed to either originate from or being influenced by oxygen doping, i.e. one at 538 cm^{-1} and one at 571 cm^{-1}. The calculated frequencies may be attributed to the 571 cm^{-1} peak. Since, however, for small doping levels the frequency is lowered the experimentally observed 538 cm^{-1} mode could be explained by the same kind of vibration in the neighborhood

[3]The O2 atoms move away from the OI site, while the Hg and the Ba atoms come closer.

of higher oxygen concentration.

The optimized lattice geometry for different doping values has also been used to calculate the band structure as a function of δ. As predicted by Novikov *et al.* [77] doping with oxygen should have similar effects on the band structure like applying pressure: The van Hove singularity should move closer to the Fermi level, and it should intersect E_F close to or at optimal doping. This prediction is proven by the present calculations and can be seen in Figure 8.36. These findings support the picture that the van Hove singularity could be directly related to T_c.

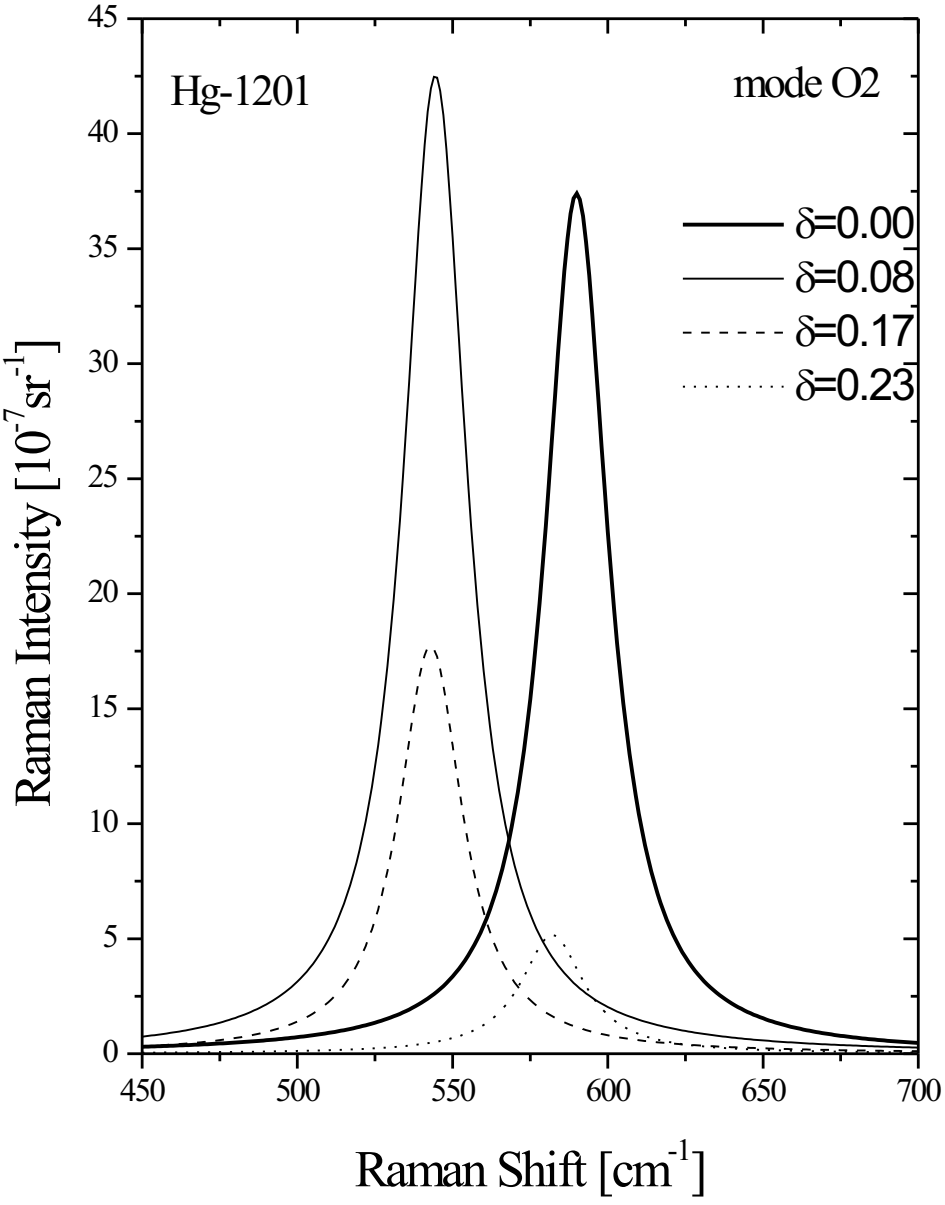

Figure 8.35: Raman spectra of Hg-1201 as a function of the doping concentration δ.

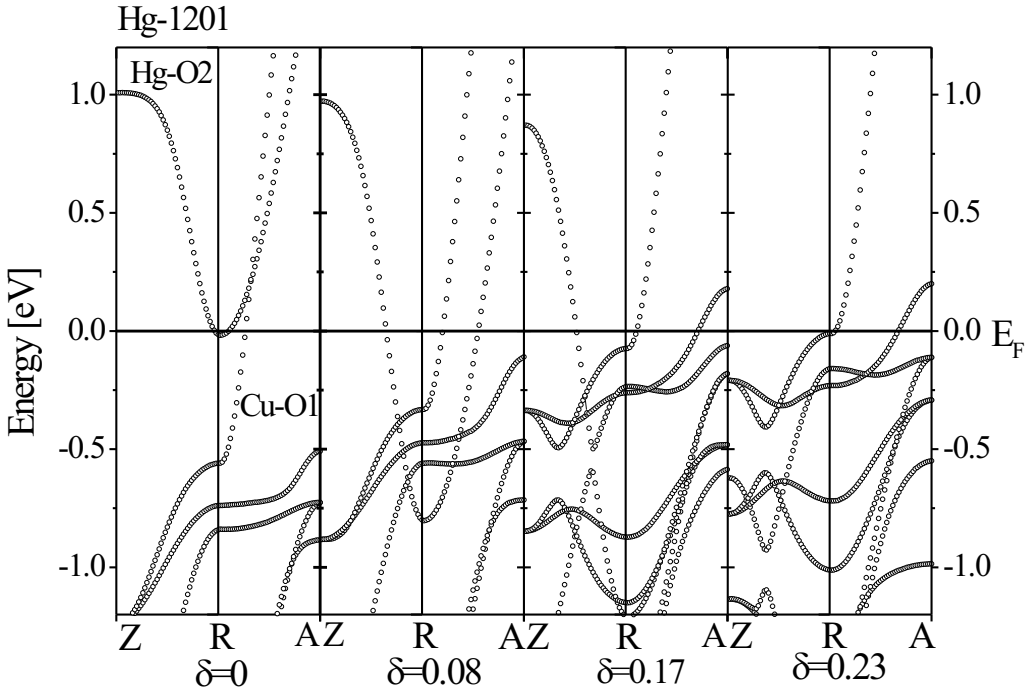

Figure 8.36: Band structure as a function of the doping level δ

List of Figures

List of Tables

Bibliography

[1] J.G. Bednorz und K.A. Müller, Z. Phys. B **64**,189 (1986).

[2] H.K. Onnes: Comm. Leiden **120b** (1911).

[3] H.K. Onnes: Comm. Leiden **108**, Proc. Roy. Acad. Amsterdam **11**, 168 (1908).

[4] W. Meissner and R. Ochsenfeld: Naturwissenschaften **21**, 787 (1933).

[5] E. Maxwell: Phys. Rev. **86**, 235 (1952).

[6] J.M. Lock, A.B. Pippard u. D. Shoenberg: Proc. Cambridge Phil. Soc. **47**, 811 (1951).

[7] A.Schilling, M. Cantoni, J.D. Guo and H.R. Ott, Nature (London) 362 (1993) 226.

[8] E.V. Antipov, S.M. Loureiro, C. Chaillout, J.J. Capponi, P. Bordet, J.L. Tholence, S.N. Putilin and M. Marezio, Physica C215 (1993) 1.

[9] C.E. Gough, M.S. Colclough, E.M. Forgan, R.G. Jordan, M. Keene, C.M. Muirhead, A.I.M. Rae, N. Thomas, J.S. Abell und S. Sutton, Nature (London) **326**, 855 (1987).

[10] A. Bussmann-Holder, L. Genzel, A. Simon u. A. R. Bishop: Z. Physik **C 91**, 271 (1993).

[11] W. Pint and E. Schachinger (1991). Phys. Rev. B **43**, 7664.

[12] M.D. Whitmore, J.P. Carbotte, and E. Schachinger (1984). Phys. Rev. B **29**, 2510.

[13] Z.-X. Shen, A.Lanzara, and N. Nagaosa, cond-mat 0102244 v2

[14] A. Lanzara, P.V. Bogdanov, X.J. Zhou, S.A. Kellar, D.L. Feng, E.D. Lu, T. Yoshida, H. Eisaki, A. Fujimori, K. Kishio, J.-I Shimoyama, T. Noda, S. Uchida, Z. Hussain, Z.-X. Shen, *Evidence for Ubiquitous Strong Electron-Phonon Coupling in High Temperature Superconductors*, Preprint

[15] W. Buckel, ***Supraleitung***, *Grundlagen und Anwendungen*, 5. Auflage.

[16] B. Renker *et al.*, Physica C153-155, 1067 (1988).

[17] M. Cardona *et al.*, Solid State Commun. 75 (3), 219 (1990).

[18] N. Pyka *et al.*, Phys. Rev. Lett. 70, 1457 (1993).

[19] R. Zeyher: Physica C185-189, 1437 (1991).

[20] R. Kouba, C. Ambrosch-Draxl and B. Zangger, Phys. Rev. B **60**, 9321 (1999).

[21] Xingjiang Zhou, M. Cardona, C.W. Chu, Q.M. Lin, S.M. Loureiro, M. Marezio, Physica C 270 (1996) 193-206.

[22] K. Kitazawa, H. Takagi, K. Kishio, T. Hasegawa, S. Uchida, S. Tajima, S. Tanaka u. K. Fueki: Physica **C 153-155**, 9 (1988).

[23] M. Born and R. Oppenheimer, Ann. Physik **84**,457 (1927).

[24] M. Born und K. Huang, *Dynamical Theory of Crystal Lattices*, (Oxford University Press, 1954).

[25] H. Sormann, *Theoretische Festkoerperphysik 1*, Skriptum TU-Graz.

[26] E.P. Wigner, Ann. Math. 40, 149 (1939)

[27] H. Kuzmany, *Festkörperspektroskopie*, Eine Einführung, Springer 1989

[28] Ran Liu, *Ramanstreuung an Hoch-T_c-Supraleitern*, PhD thesis, Max-Planck-Institut für Festkörperforschung Stuttgart

[29] Daniel C. Harris, *Symmetry and Spectroscopy*, Dover Publications, Inc., New York (1978)

[30] P.M.A. Sherwood, *Vibrational spectroscopy of solids*, Cambridge University Press (1972)

[31] D.L. Rousseau, R.P. Baumann und S.P.S. Porto, J. of Raman Spectroscopy, **10**,253 (1981)

[32] W. Hayes and R. Loudon *Scattering of Light by Crystals*, Wiley, New York, (1978)

[33] C. Ambrosch-Draxl, H. Auer, R. Kouba, E. Ya. Sherman, P. Knoll, M. Mayer, Phys. Rev. B (in print)

[34] P. Knoll and C. Ambrosch-Draxl, in Proceedings of the International Workshop on *Anharmonic Properties of High-T_c Cuprates*, ed. D. Mihailovich, G. Ruani, E. Kaldis und K.A. Müller, World Scientific, 220 (1995).

[35] H. Hohenberg and W. Kohn (1964). Phys. Rev.**136**, B864

[36] D.C. Langreth and M.J. Mehl (1983). Phys. Rev. B **28**, 1809.

[37] A.D. Becke (1988). Phys. Rev. A **38**, 3098.

[38] J.P. Perdew, J.A. Chevary, S.H. Vosko , K.A. Jackson, M.R. Pederson, D.J. Singh and C. Fiolhais (1992). Phys. Rev. B **46**, 6671.

[39] O. Gunnarsson, M. Jonson and B.I. Lundqvist (1977). Solid State Commun. **24**, 765.

[40] O. Gunnarsson, M. Jonson and B.I. Lundqvist (1979). Phys. Rev. B. 20, 3136.

[41] O. Gunnarsson, R.O. Jones (1980). Phys. Scr. **21**, 394.

[42] W. Kohn and L.J. Sham (1965). Phys. Rev. **140**, A1133

[43] D. Singh. 1991, Phys. Rev. B43, 6388

[44] P. Blaha, K. Schwarz, and J. Luitz, *WIEN97, A Full Potential Linearized Augmented Plane Wave Package for Calculating Crystal Properties*, Karlheinz Schwarz, Techn. Universität Wien, 1999, ISBN 3-9501031-0-4.

[45] F. Wooten, *Optical Properties of Solids*, Academic Press, New York and London, 1972

[46] R. Abt, *Berechnung Optischer Eigenschaften von Hochtemperatursupraleitern in der LAPW-Methode*, PhD thesis, Institut für theoretische Physik der Universität Graz, Mai 1997

[47] B.A. Scott, E.Y. Suard, C.C. Tsuei, D.B. Mitzi, T.R. McGuire, B.H. Chen and D. Walker, Physica C 230 (1994) 239.

[48] E.M. Kopnin, E.V. Antipov, J.J. Capponi, P. Bordet, C. Chaillout, S. de Brion, M. Marezio, A.P. Bobylev and G. van Tendeloo, Physica C 243 (1994) 239.

[49] Q. Huang, J.W. Lynn, Q. Xiong and C.W. Chu, Phys. Rev. B 52 I, 462 (1995)

[50] X.Zhang *et al.*, /Journal of physics and Chemistry od Solids 60 (1999) 1675-1682

[51] M. Cardona, R. Liu, C. Thomsen, W. Kress, E. Schönherr, M. Bauer, L. Genzel, and W. König, Solid State Commun. **67**, 789 (1988).

[52] D. Zech, H. Keller, K. Conder, E. Kaldis, E. Liarokapis, N. Poulakis, and K.A. Müller, Nature **371**, 681 (1994).

[53] J. H. Nickel, D. E. Morris, and J. W. Ager, Phys. Rev. Lett. **70**, 81 (1993).

[54] V. B. Vykhodets, T. E. Kurennykh, V. A. Pavlov, and A. A. Fotiev, JETP Lett. **58**, 431 (1993).

[55] S. I. Bredikhin, A. A. Maksimov, B. C. H. Steele, and I. I. Tartakovskii, Physica C **196**, 112 (1992).

[56] O.K. Andersen, Phys. Rev. B **12**,3060 (1975).

[57] T. Strach, T. Ruf, E. Schoenherr, and M. Cardona, Phys. Rev. B **51**, 16460 (1995).

[58] G. Burns, F. H. Dacol, F. Holtzberg, and D. L. Kaiser, Solid State Commun. **66**, 217 (1988).

[59] B. Friedl, C. Thompson, E. Schönherr and M. Cardona, Solid State Commun. **76**, 1107 (1990) .

[60] R. Liu, C. Thomsen, W. Kress, M. Cardona, B. Gegenheimer, F.W. de Wette, J. Prade, A.D. Kulkarni, and U. Schröder, Phys. Rev. B **37**, 7971 (1988).

[61] V. G. Hadjiev, M. N. Iliev, C. Raptis, L. Kalev, and B. M. Wanklyn, Physica C **166**, 225 (1990).

[62] K. F. McCarty, J. Z. Liu, R. N. Shelton, and H. B. Radousky, Phys. Rev. B **41**, 8792 (1990).

[63] R. Kouba, C. Ambrosch-Draxl, and B. Zangger, Phys. Rev. B **60**, 9321 (1999).

[64] R. Kouba, C. Ambrosch-Draxl, P. Korzhavyi, and B. Johansson, *First-principles investigations of structural properties, phonons, and vacancy ordering in* $YBa_2Cu_30_{7-x}$, Proceedings of the First Regional Conference on Matgnetic and Superconducting Materials (MSM99), Eds. M. Akhavan, J. Jensen, and K. Kitazawa, World Scientific (2000), p. 259.

[65] R. Kouba and C. Ambrosch-Draxl, Phys. Rev. B **56**, 14766 (1997).

[66] R. E. Cohen, W. E. Pickett, and H. Krakauer, Phys. Rev. Lett. **64**, 2575 (1990).

[67] C. O. Rodriguez, A. I. Liechtenstein, I. I. Mazin, O. Jepsen, O. K. Andersen, and M. Methfessel, Phys. Rev. B **42**, 2692 (1990).

[68] O. V. Misochko, E. I. Rashba, E. Ya. Sherman, and V. B. Timofeev, Phys. Rep. **194**, 387 (1990).

[69] E. T. Heyen, S. N. Rashkeev, I. I. Mazin, O. K. Andersen ,R. Liu, M. Cardona, and O. Jepsen, Phys. Rev. Lett. **65**, 3048 (1990).

[70] E. I. Rashba and E. Ya. Sherman, JETP Lett. **47**, 482 (1988).

[71] The importance of investigating the site-selective isotope substitution by Raman spectroscopy was mentioned in E. Altendorf, J. Chrzanowski, J. C. Irwin, and J. P. Frank, Phys. Rev. B **43**, 2771 (1991).

[72] R. Henn, T. Strach, E. Schönherr, and M. Cardona, Phys. Rev. B **55**, 3285 (1997).

[73] C. Ambrosch-Draxl, R. Kouba, and P. Knoll, Z. f. Physik B **104**, 687 (1997).

[74] O.K. Anderson, A.I. Liechtenstein *et al.*, Physica C 185-189 (1991) 147-155

[75] W. Reichardt and N. Pyka *et al.*, Physica C 162-164 (1989) 464-465

[76] P. Blaha, K. Schwarz, and J. Luitz, *WIEN97, A Full Potential Linearized Augmented Plane Wave Packkage for Calculating Crystal Properties*, Karlheinz Schwarz, Techn. Universität Wien, Austria, 1999, ISBN 3-9501031-0-4.

[77] D.L. Novikov, M.I. Katsnelson, Jaejun Yu, A. V. Postnikov, A.J. Freeman, Phys. Rev. B 54 II, 1313 (1996)

[78] B.A. Hunter *et al.*, Physica C 221, 1 (1994)

[79] D.L. Novikov, O.N. Mryasov, A.J. Freeman, Physica C 222 (1994) 38.

[80] A.L. Cornelius, J.S. Shiling, Physica C 218 (1993) 369.

[81] V.L Aksenov, A.M. Balagurov, B.N. Wsavenko, D.V. Sheptyakov, V.P. Glazkov, V.A. Somenkov, S.Sh. Shilshtein, E.V.Antipov, S.N. Putilin, Physica C 275 (1997) 87.

[82] J.H. Eggert, J.Z. Hu, H.K. Mao, L. Beauvais, R.L. Meng, C.W. Chu, Phys. Rev. B 49 (1994) 15299.

[83] Q. Huang *et al.*, IEEE Transactions Magn. Mat. 27,833 (1991).

[84] P.G. Radaelli, J.L. Wagner, B.A. Hunter, M.A. Beno *et al.*, Physica C 216 (1993) 29-35

[85] R. Gatt, E. Olsen, A. Morawski *et al.*, Physica C 276 (1997) 270-276

[86] K.F. McCarty, B. Morosin, D.S. Ginley and D.R. Boehme, Physica C 157 (1989) 135.

[87] A. Sacuto, A. Lebon, D. Colson *et al.*, Physica C 259 (1996) 209-217.

[88] Xingjiang Zhou, M. Cardona, D. Colson, and V. Viallet Phys. Rev. B **55**, 12770 (1997).

[89] In-Sang Yang, Hye-Soo Shin, Hye-Gyong Lee *et al.*, Phys. Rev. B **51**, 644 (1995).

[90] A.R. Armstrong W.I.F. David *et al.*, Phys. Rev. B **52**, 15551 (1995).

[91] Y. J. Uemura, L. P. Le, G. M. Luke, B. J. Sternlieb, W. D. Wu, J. H. Brewer, T. M. Riseman, C. L. Seaman, M. B. Maple, M. Ishikawa, D. G. Hinks, J. D. Jorgensen, G. Saito, and H. Yamochi, Phys. Rev. Lett. **66**, 2665 (1991).

[92] H. Zhang and H. Sato, Phys. Rev. Lett. **70**, 1697 (1993).

[93] Q. Xiong, Y. Y. Xue, Y. Cao, F. Chen, Y. Y. Sun, J. Gibson, and C. W. Chu, Phys. Rev. B **50**, 10346 (1994).

[94] D. J. Singh, Physica **C212**, 228 (1993).

[95] D. J. Singh, W. E. Pickett, Phys. Rev. Lett., **73**, 476 (1994).

[96] P. Suele, C. Amrosch-Draxl, H. Auer, to be published.